

# The Aortic Wrap: an experimental and computational investigation of a device-based method for reduction of arterial pressure

Francesca Maria Giudici (*MSc, BSc*)

A thesis of The Australian School of Advanced Medicine, Faculty of Human Sciences, Macquarie University, submitted in fulfilment of the requirements for the degree of Doctor of Philosophy.

Supervisor:

Prof. Alberto Avolio

Adjunct Supervisor:

Prof. Michael O'Rourke

April 2014



THE AUSTRALIAN SCHOOL  
OF ADVANCED MEDICINE



## **Declaration of originality**

I hereby declare that the work presented in this thesis has not been submitted for a higher degree to any other university or institution. To the best of my knowledge this submission contains no material previously published or written by another person, except where due reference is stated otherwise. Any contribution made to the research by others is explicitly acknowledged.

Francesca Maria Giudici

Australian School of Advanced Medicine  
Faculty of Human Science  
Macquarie University

April 2014

## **Declaration of contributions**

### **Chapter 3**

The original multibranched model was created in Fortran language by Prof. Alberto Avolio. The model implementation on the Matlab platform was performed by Dr. Koen Matthys (Brunel University).

### **Chapter 4**

The fabric aortic model was built in collaboration with Prof. Michael O'Rourke.

### **Chapter 5**

The distributed silicon model of the arterial circulation was built by the BioMMeda research group at IBiTech, Ghent University, in Ghent, Belgium, under the direction of Prof. Patrick Segers. The experiments were performed under the supervision of Prof. Segers.

### **Chapter 6**

Dr. Azadeh Farnoush and Prof. Yi Qian (Macquarie University, Sydney, Australia) provided advice and feedback for the CFD simulations.

### **All Chapters**

The work presented in this thesis was supervised by Prof. Alberto Avolio and Prof. Michael O'Rourke.

## Acknowledgements

The Ph.D. experience is at times a quite lonely one, made of hours spent staring at the laptop screen, thinking out loud in the shower, and waking up at your desk, alone, with no idea of the time. Yet, it is also a collective effort: it takes a village to produce a Ph.D. thesis. This is my village, and I would like to thank every one of its inhabitants.

Thanks to Albert, who guided me through this Ph.D. journey: despite a false start and several hurdles, his constant support and resourcefulness made it possible for me to get here today. I will never forget his all-encompassing wisdom and his home-made gnocchi.

Thanks to Michael, whose brilliant ideas and tireless love of knowledge are beyond anyone's reach: it is only because of him that the Aortic Wrap exists. I am honoured I had the opportunity to work with one of my scientific "idols", whose papers I avidly read years before life took me to Australia.

Thanks to everyone in the Vascular Research group at ASAM (in no specific order): Audrey Adj, Nyan Khin, Miok Kim, George Lindesay, Xu Ke, Isabella Tan, Parisa Kouchaki, Dr. Wendy Liu, Dr. Mojtaba Golzan, Dr. Martin Turner, and Dr. Mark Butlin. But, most of all, thanks to Kayla Viegas, who shared this experience with me from the beginning till the end, through tough times and amazing times, tears and laughs.

Thanks to Dr. Azadeh Farnoush and Prof. Yi Qian at Macquarie University, who helped me with the CFD component of this thesis and provided the software to perform the simulations.

Thanks to Prof. Patrick Segers, who made it possible for me to come to Australia in the first place and, years later, offered me IBiTech's facilities to perform some of the experimental studies presented in this thesis: he made me feel part of the team from day one. Thanks to

Jurgen Deviche and everyone else in the bioMMeda group at IBiTech, Ghent University: Ghent feels like a second home to me, and bioMMeda is one of the reasons why.

Thanks to all my friends, in Australia, in Italy, and all over the world: they are my “home” and they know it. Thanks especially to Chiara, Ashley, Helena, and most of all Josh, who kept my mental sanity within physiological levels during the last months of this Ph.D. – I will be forever grateful.

Thanks to my father Roberto, who doesn’t complain too much about me living on the opposite side of the world, and to my family, for their constant support.

Thanks, most of all, to my grandmother Luisa: she was an example of moral strength, intellectual curiosity, and savoir-faire. She supported my education from my first day in kindergarten and I would definitely not be here right now, writing this page, if it wasn’t for the role she played in my life. This thesis is dedicated to her.

## **Publications**

### **Refereed conference proceedings**

**Giudici F**, Qian Y, O'Rourke M, Avolio A. "Simulation of Reduction of Proximal Aortic Stiffness by an Elastic Wrap and Effects on Pulse Pressure". *Engineering in Medicine and Biology Society (EMBC), 2012 Annual International Conference of the IEEE*, 2012:657–660.

### **Conference abstracts published in journals**

**Giudici F**, Qian Y, O'Rourke M, Avolio A. "Reduction of arterial pulse pressure by and elastic aortic wrap: a modelling study". *Meeting of the International Society of Hypertension*, Sydney, Australia (2012). *Journal of Hypertension* 2012(30):9, eSupplement 1, a139.

**Giudici F**, O'Rourke M, Qian Y, Avolio A. "Reduction of aortic stiffness by an external passive elastic aortic wrap: an *in vitro* study". *23rd European Meeting on Hypertension and Cardiovascular Protection*, Milan, Italy (2013). *Journal of Hypertension* 2013(31):6, e-Supplement A, e100 7B.07.

**Giudici F**, Segers P, O'Rourke M, Qian Y, Avolio A. "Reduction of aortic pressure by a passive elastic aortic wrap: an *in vitro* study". *Meeting of High Blood Pressure Research Council of Australia*, Melbourne, Australia (2013). *Hypertension* 2014, in press.

**Giudici F**, O'Rourke M, Qian Y, Farnoush A, Avolio A. "Effect of diameter reduction on aortic wall shear stresses: a pilot computational fluid dynamic study of a model of aortic wrap". *Meeting of Pulse of Asia*, Seoul, Korea (2013). *Pulse* 2013;1:35-76 (M77).

**Giudici F**, Qian Y, O'Rourke M, Avolio A. "Reduction of arterial pulse pressure by and elastic aortic wrap: a modelling study". *Meeting of Pulse of Asia*, Sydney, Australia (2012).

### **Abstracts published in conference proceedings**

**Giudici F**, Segers P, O'Rourke M, Qian Y, Avolio A. "Reduction of aortic pressure by a passive elastic aortic wrap: an *in vitro* study". *Australian Biomedical Engineering Conference*, Sydney, Australia (2013).

## Abstract

**Background:** Age-related aortic stiffening is a major determinant of isolated systolic hypertension (ISH) and is mainly due to mechanical fatigue-induced deterioration of elastin in the aortic wall. The Aortic Wrap (AW), a proposed method to restore aortic distensibility, is a highly distensible implantable device secured around the ascending aorta (AA): by decreasing the AA diameter (D), the pulsatile load is transferred from the collapsed AA wall to the AW, thus enabling aortic pulse pressure (PP) reduction. This thesis aims to evaluate the efficacy of the AW in increasing distensibility and decreasing PP and systolic pressure.

**Multibranched model:** A multibranched mathematical model of the arterial system was used to simulate the effects of the AW on PP and input impedance ( $Z_{in}$ ): the AW was simulated by varying AA radius and stiffness. The study showed that the AW was able to achieve an 8% decrease in PP with an 80% reduction in functional stiffness, compensating for the increase in PP and  $Z_{in}$  associated with a 20% D reduction.

**In vitro distensibility study:** Tubular models of the ascending aorta were used to determine the effects of distensible synthetic AWs with variable D reduction on aortic distensibility. Pressure changes were measured at incremental volumes of 5ml and pressure–volume (P-V) curves were obtained. Distensibility was calculated, and was initially higher for all wrapped compared to unwrapped configurations, until a critical pressure ( $P_{cr}$ ) value was reached, at which distensibility dropped to unwrapped values. The wrap determined a 5 fold increase in distensibility when applied to a rigid aortic model with a 20% D reduction in the 50-200 mmHg pressure range.

**In vitro pulsatile study:** A silicone model of the arterial tree was connected to a pulsatile hydraulic circuit with variable heart rates (HR) and stroke volumes (SV). The AA and thoracic aortic segment were wrapped. Pressure waves were recorded via a Millar catheter at 10 locations along the model. PP,  $Z_{in}$ , and systemic characteristic impedance were consistently decreased after wrapping at every location. However, the efficacy of the AW was markedly influenced by HR and SV. For intermediate HR (60 bpm) and SV (60 ml), PP was reduced by 8% in the AA after wrapping applying a 20% D reduction.

**Computational fluid-dynamic study:** 3D models of the unwrapped and wrapped aorta and aortic arch were created with variable wrap geometries. CFD investigations were performed applying steady inflow velocity. The narrowing due to the AW diameter reduction increased maximum wall shear stress (WSS) values, maximum velocity values, and pressure drops along the model. For curved models of the aortic arch with wrapped diameter reduction > 30%, the AW created areas of flow recirculation and separation.

**Conclusions:** The studies demonstrated that the AW is an effective method to increase AA distensibility and decrease aortic PP, therefore proposing it as a potential treatment for ISH and congestive heart failure. The diameter reduction associated with the AW leads to potentially unfavorable hemodynamic effects: a compromise between unloading efficacy and lumen reduction should thus be pursued.



# Table of Contents

Declaration of originality	i
Declaration of contributions	ii
Acknowledgements	iii
Publications	v
Abstract	vi
Table of Contents	vii
List of Figures	xi
List of Tables	xviii
List of Abbreviations	xix
List of Symbols	xx
<b>Chapter 1 Preface</b>	<b>1</b>
<b>Chapter 2 Background</b>	<b>3</b>
2.1 Pulsatile hemodynamics	3
2.1.1 Arterial structure and function	3
2.1.2 Mechanical properties of the arteries	5
2.1.3 Pulse Wave Velocity	9
2.1.4 Arterial hemodynamics	11
2.1.5 Arterial impedance and cardiac power	14
2.2 Age-related arterial stiffening	16
2.2.1 Arterial aging and arteriosclerosis	16
2.2.2 Age-related arterial stiffening mechanisms	21
2.2.3 Functional effects of arterial stiffening	24
2.3 Isolated Systolic Hypertension	28
2.3.1 ISH and arterial stiffness	28
2.3.2 Current treatments of ISH	30
2.4 The Aortic Wrap	33
2.4.1 What is the aortic wrap	33
2.4.2 Comparison with commercial device-based treatments of heart failure	35

2.4.3	Experimental evidence of “stiffening” aortic wraps	37
2.4.4	Initial study on the Aortic Wrap	39
2.4.5	Aim of the thesis	40

### **Chapter 3 Simulation of reduction of proximal aortic stiffness by an elastic wrap and effects on**

#### **pulse pressure**

3.1	Background	42
3.2	Methods	44
3.3	Results	45
3.4	Discussion	48

### **Chapter 4 In vitro investigation of the effects of the Aortic Wrap on distensibility of a rigid**

#### **cylindrical model of the aorta**

4.1	Introduction	51
4.2	Methods	53
4.2.1	Aortic models	53
4.2.2	Elastic wraps	55
4.2.3	Execution of the experiments	57
4.2.4	Data analysis	60
4.3	Results	61
4.3.1	Reproducibility	61
4.3.2	Experiment A	62
4.3.3	Experiment B	63
4.3.4	Experiment C	66
4.4	Discussion	67
4.4.1	Limitations of the wrap models	67
4.4.2	Silicon aortic model	69
4.4.3	Fabric aortic model	70
4.5	Conclusions	71

**Chapter 5 In vitro investigation of the effects of the Aortic Wrap on pressure and impedance in a silicon model of the arterial circulation \_\_\_\_\_73**

5.1	Introduction	73
5.2	Methods	74
5.2.1	Arterial tree model	74
5.2.2	Wrap models	75
5.2.3	Hydraulic set-up	78
5.2.4	Measurements	79
5.2.5	Execution of the experiments	81
5.2.6	Data analysis	82
5.3	Results	83
5.3.1	Reproducibility of the experiments	83
5.3.2	Pressure wave shape	84
5.3.3	PP and SP changes	86
5.3.4	Zc and Zin changes	91
5.4	Discussion	95
5.4.1	Efficacy in PP and Z reduction	95
5.4.2	Unloading mechanism	96
5.4.3	Comparison with “stiffening” wrapping studies	97
5.4.4	Limitations of the study	97

**Chapter 6 Computational fluid dynamic study of the effects on velocity patterns and wall shear stress of the ascending aortic diameter reduction induced by wrapping \_\_\_\_\_99**

6.1	Introduction	99
6.2	Methods	100
6.2.1	Geometrical models	100
6.2.2	Discretization	103
6.2.3	Fluid dynamic simulations	105
6.3	Results	106
6.3.1	Straight model	106

6.3.2	Realistic arch model	110
6.4	Discussion	116
<b>Chapter 7</b>	<b>Conclusions</b>	<b>119</b>
<b>Appendix</b>		<b>123</b>
<b>References</b>		<b>125</b>

## List of Figures

<b>Figure 2.1:</b> Different layers of the arterial wall: 1) tunica intima, 2) internal elastic lamina, 3) tunica media, 4) thin medial elastic membrane, 5) tunica adventitia. Reproduced from Kahle <i>et al.</i> (Kahle, Leonhardt, and Platzer 1992).....	5
<b>Figure 2.2:</b> Elastic modulus and PWV measured in the aorta and iliac artery of a young healthy subject; both PWV and elastic modulus increase as the distance from the hearth increases. Reproduced from Nichols <i>et al.</i> (Nichols et al. 1987) .....	6
<b>Figure 2.3:</b> Linear (left) and non-linear (right) relationships between stress (S) and strain (or length, L). $E_{inc} = (S_2 - S_1) \cdot (L_m) / (L_2 - L_1)$ . Reproduced from Milnor <i>et al.</i> (Milnor 1989).....	7
<b>Figure 2.4:</b> Pressure diameter curve of the abdominal aorta based on 28 individual recordings taken both at rest and during isometric exercise. Note the inflection at 90-110 mmHg with a stiffer vessel wall above than below. Reproduced from Länne <i>et al.</i> (Länne et al. 1992) .....	8
<b>Figure 2.5:</b> Carotid-to-femoral PWV (cfPWV) assessed with tonometry in a young subject, calculated with the time delay method ( $\Delta t$ = time delay between the feet of the pressure waves, D = distance between the measurement locations). Reproduced from Redheuil <i>et al.</i> (Redheuil et al. 2010).....	10
<b>Figure 2.6:</b> Progressive increase of PWV with increasing distance from the heart in the dog (solid line) and measured in young adult humans (broken line). Reproduced from Nichols <i>et al.</i> (Nichols et al. 2011) .....	11
<b>Figure 2.7:</b> Average aortic input impedance calculated for five normal adult subjects (vertical and horizontal bars represent standard errors of the means of modulus, phase, and frequency). $Z_o$ is the estimated characteristic impedance ( $53 \pm 4 \text{ dyn sec/cm}^5$ ) obtained by averaging the moduli above 2 Hz. Reproduced from Nichols <i>et al.</i> (Nichols et al. 1977) .....	15
<b>Figure 2.8:</b> Age and aortic and brachial pulse wave velocity (PWV) in healthy subjects. Data from the Anglo-Cardiff Collaborative Trial (ACCT) study population. Note the relatively linear relationship for brachial PWV (broken line) compared with the curved relationship for aortic PWV (solid line). Reproduced from McEniery <i>et al.</i> (McEniery, Wilkinson, and Avolio 2007) .....	18
<b>Figure 2.9:</b> fig.2 Effect of age on measures of proximal aortic function. A) AA strain (dot) and distensibility (squares) by decades of age. B) AA distensibility (age <50 in red dots and >50 years in blue dots). C) Aortic arch PWV (dark squares) and carotid-to-femoral PWV (open squares) by decades of age. D) Aortic arch PWV (red dots, <50 years of age; blue dots, >50 years of age). Reproduced from Redheuil <i>et al.</i> (Redheuil et al. 2010). .....	18
<b>Figure 2.10:</b> Aortic PWV measured between base of the neck and groin for all subjects (both male and female subjects) between ages 3 and 89 years. Individual values were determined as the average of 10 pairs of pulses simultaneously recorded with identical transcutaneous Doppler transducers. Reproduced from Avolio <i>et al.</i> (Avolio et al. 1983). .....	19
<b>Figure 2.11:</b> Two faces of the cameo: the Cardiovascular Continuum (left) and the Aging Continuum (right), and their interaction. Reproduced from O'Rourke <i>et al.</i> (O'Rourke, Safar, and Dzau 2010). .....	20
<b>Figure 2.12:</b> Comparison of the arterial wall elastin composition in a child (left) with that in an elderly adult (right). Stain: Orcein and Giesen, magnification $\times 450$ . Prepared by P Lauren, reproduced from O'Rourke <i>et al.</i> (O'Rourke et al. 1987). The wall of the older human is	

disorganized as a consequence of fraying and fracture of the elastic lamellae and loss of muscle attachments, together with increase in collagen fibres and mucoid material. ....21

**Figure 2.13:** Stress–strain relationship of the human aorta. Non-linear relationship between arterial stress (pressure) and strain (change in relative diameter). At lower strains, the stress is taken up predominantly by the elastin fibres. At higher strains, the stress is taken up by the stiffer collagen fibres. The effects of age or loss of arterial elasticity are generally to engage the collagen fibres at lower strain, hence effectively increasing pulse pressure for the same strain (as indicated by the arrows). Reproduced from McEniery *et al.* (McEniery, Wilkinson, and Avolio 2007). ....22

**Figure 2.14:** Pressure waveforms synthesized for the ascending aorta from the measured brachial artery waveforms in 3 women of the same family—an 18-year-old at left, a 48-year-old at centre, and a 97-year-old at right. Pulse pressure is increased almost 4-fold in the ascending aorta. Reproduced from O’Rourke and Hashimoto (O’Rourke and Hashimoto 2007). ....25

**Figure 2.15:** Ascending aortic impedance shown schematically in a young 20-year-old and in an 80-year-old human subject showing the effect of doubling of characteristic impedance (older curve set higher) and early return of wave reflection (first minimum at double the frequency). In consequence of both, impedance modulus at heart rate frequency is increased 4-fold. Reproduced from Nichols *et al.* (Nichols et al. 2011) .....26

**Figure 2.16:** Simple tubular models of the arterial system, connecting the heart (left) to the peripheral circulation (right) in a young (top) and old (bottom) subject. In the young subject, the tube is distensible, whereas in the old subject it is stiff. The distal end of the tube constitutes a reflection site where the pressure wave travelling down the tube is reflected back to the heart. The wave travels slowly in the young distensible tube so that the reflected wave boosts pressure in diastole when it returns to the proximal end. The wave travels faster in the old stiffer tube, returns earlier, and boosts pressure in late systole. Flow input from the heart is intermittent in both young and old subjects. In the young subject, pulsations are absorbed in the distensible tube so that outflow is steady or almost so. In the old subject with stiff tube, pulsations cannot be absorbed, and so output from tube into peripheral microvessels is pulsatile. Reproduced from O’Rourke and Hashimoto (O’Rourke and Hashimoto 2007). ....27

**Figure 2.17:** Frequency distribution of untreated hypertensive individuals by age and hypertension subtype. The numbers at the tops of the bars represent the overall percentage distribution of all subtypes of untreated hypertension in the age group (the Third Report of the National Health and Nutrition Examination Survey, 1988–1994). Isolated diastolic hypertension (systolic blood pressure [SBP] <140 mm Hg and diastolic blood pressure [DBP] >90 mm Hg) shown in yellow, systolic-diastolic hypertension (SBP >140 mm Hg and DBP>90 mm Hg) shown in red, and isolated systolic hypertension (SBP>140 mm Hg and DBP <90 mm Hg) shown in aqua. Reproduced from Franklin *et al.* (Franklin 2012). ....29

**Figure 2.18:** Arterial pressure components by age: group averaged data for all subjects and with deaths, myocardial infarction, and chronic heart failure excluded. Averaged blood pressure levels from all available data from each subject within 5-year age intervals (30 to 34 through 80 to 84) by SBP groupings 1 through 4. Thick line represents entire study cohort (2036 subjects); thin line represents study cohort with deaths and nonfatal myocardial infarction and chronic heart failure excluded (1353 subjects). Reproduced from Franklin *et al.* (Franklin et al. 1997). ....31

<b>Figure 2.19:</b> Pressure (P)-diameter (D) or stress-strain relations for elastic arteries. Elastance can be estimated as the slope ( $\Delta P/\Delta D$ ) of the pressure-diameter curve. With advancing age the curve for elastic arteries shifts to the left, indicating increased elastance for all diameters. Drugs have little direct effect on elastic arteries; however, they do have a passive effect. Vasoconstrictor drugs cause an increase in pressure, diameter and elastance while vasodilator drugs cause a decrease in pressure, diameter and elastance. The pressure-diameter curve does not shift. Reproduced from Nichols <i>et al.</i> (Nichols and Edwards 2001).....	32
<b>Figure 2.20:</b> Scheme of the Aortic Wrap design concept: a young thoracic aorta (left), an old dilated and stiffened thoracic aorta (centre), and an old aorta (right) in which the ascending aortic lumen is restored to young values by means of the Aortic Wrap (in black). .....	34
<b>Figure 2.21:</b> Schematic diagram of the intra-aortic balloon pump inserted in the thoracic aorta, operating during diastole (left) and systole (right). .....	36
<b>Figure 2.22:</b> Schematic diagram of the extra-aortic balloon counterpulsation device. A) Deflation during diastole and B) inflation during systole. Reproduced from Legget <i>et al.</i> (Legget et al. 2005).....	36
<b>Figure 2.23:</b> Diagram of the dog arterial system reproduced from (O'Rourke 1965), showing how arterial distensibility was reduced by applying ferrules to the brachio-cephalic artery and descending thoracic aorta. similar wrapping pattern could be used for destiffening of the aorta. ....	38
<b>Figure 2.24:</b> Picture of an implanted AW in an experimental sheep model. Reproduced from Iliopoulos. (Iliopoulos 2006) .....	40
<b>Figure 3.1:</b> PP (as % of PP100) calculated by the model for the aortic root vs. variations in R (as % of R100) and E (as % of E100) of the ascending aortic segment. ....	46
<b>Figure 3.2:</b> $Z_c$ (as % of $Z_c100$ ) calculated by the model for the aortic root vs. variations in R (as % of R100) and E (as % of E100) of the ascending aortic segment. ....	47
<b>Figure 3.3:</b> Modulus of $Z_{in}$ calculated by the model at the aortic root, when no variations are imposed ( $R = 100\% R100$ , $E = 100\% E100$ , solid line) and for variations that simulate what is expected to occur after wrapping ( $R = 80\% R100$ , $E = 20\% E100$ , dotted line).....	48
<b>Figure 3.4:</b> Solid lines represent PP calculated by the model (as % of PP100) at the aortic root, vs. E variations (as % of E100) of the ascending aortic segment, for four different R variations (100%, 90%, 80%, and 70% of R100). Six data points measured in the <i>in vitro</i> pilot study are plotted over the model lines with the following markers: star (material B, $R = 91\% R100$ ), triangle (material A, $R = 91\% R100$ ), plus sign (material B, $R = 82\% R100$ ), circle (material A, $R = 82\% R100$ ), x sign (material B, $R = 70\% R100$ ), square (material A, $R = 70\% R100$ ). ....	50
<b>Figure 4.1:</b> Typical experimental set up: the silicon aorta is closed at one end by the “plug” connector and is connected to a pressure transducer and a syringe via the “inlet” connector and 3-way valve. ....	54
<b>Figure 4.2:</b> “Plug” connector composed of a rigid cylindrical core and several external layers of Tygon sealed with silicon glue and hot glue. ....	54
<b>Figure 4.3:</b> A) “Inlet” connector, composed by Tygon layers around a barbed connector. B) Barbed reducing connector used as core for the “inlet” connector.....	55
<b>Figure 4.4:</b> A) Wrap obtained from a rubber inflatable balloon. B) Wrap obtained from a physiotherapy elastic band.....	57

<b>Figure 4.5:</b> A) Pressure transducer. B) Quad Bridge Amp and PowerLab acquisition system. C) Sphygmomanometer. ....	57
<b>Figure 4.6:</b> A) fabric aortic model at 0 mmHg (beginning of the experiment); B) fabric aortic model at 300 mmHg (end point of the experiment); C) wrapped fabric aortic model at 0 mmHg (beginning of the experiment); D) wrapped fabric aortic model at 300 mmHg (end point of the experiment). ....	59
<b>Figure 4.7:</b> Beginning of experiment with a single rectangular wrap derived from a physiotherapy elastic band. A) Wrapped silicon aortic model at zero pressure; B) detail of the wrap. ....	59
<b>Figure 4.8:</b> End of experiment with a single wrap derived from a physiotherapy elastic band. A) Wrapped silicon aortic model under pressure; B) detail of the wrap. ....	59
<b>Figure 4.9:</b> Experiment with multiple cylindrical wraps derived from rubber balloons. A) Beginning of the experiment – wrapped aortic model at zero pressure. B) End of the experiment – model under pressure. ....	60
<b>Figure 4.10:</b> Typical “ramp” of pressure values recorded during an experiment and displayed on the computer monitor via LabChart. Each pressure increment occurs after every volume injection via the syringe. The longer plateaux correspond to the pauses in which the syringe had to be disconnected to be refilled with water. In this particular experiment, a value of about 200 mmHg was reached after 31 volume steps (i.e. after injecting 155 ml). ....	60
<b>Figure 4.11:</b> Reproducibility experiment: average P-V curve for the unwrapped (blue line) and wrapped (red line) configurations; standard deviation is represented by vertical error bars. ....	62
<b>Figure 4.12:</b> Experiment A: Dist (mmHg <sup>-1</sup> ) plotted against pressure (mmHg), calculated for the unwrapped (blue line) and tubular wrapped (red line) configurations and for the wrap material (green line) in its tubular initial shape (before the wraps were created). Dist of the wrapped model “follows” Dist of the wrap material for pressures below P <sub>c</sub> (here approximately 50 mmHg), indicating that the wrap material is determining the global behaviour of the whole wrapped segment. When P <sub>c</sub> is reached, the silicon model “unfolds” from its collapsed lumen shape to its round “loaded” shape: this brisk change creates a tension release that causes the spike in Dist observable in the picture. After the shape change occurs, for pressures above P <sub>c</sub> the silicon model is completely distended inside the wrap, and is therefore bearing the pulsatile load; as a consequence, Dist of the wrapped segment drops to values comparable to those of the unwrapped model configuration. ....	63
<b>Figure 4.13:</b> Experiment B: normalized P-V curves obtained for the unwrapped configuration (blue line), and wrapped configurations characterized by a combination of 2 different diameters - 70% (solid lines) or 80% (broken lines) of the unwrapped diameter - and 3 different wrapping lengths – 1 wrap (red lines), 2 wraps (green lines), or 3 wraps (yellow lines). ....	64
<b>Figure 4.14:</b> Experiment B: Distensibility curves obtained for the unwrapped configuration (blue line), and wrapped configurations characterized by a combination of 2 different diameters - 70% (solid lines) or 80% (broken lines) of the unwrapped diameter - and 3 different wrapping lengths – 1 wrap (red lines), 2 wraps (green lines), or 3 wraps (yellow lines). ....	65



<b>Figure 4.15:</b> Experiment C, on fabric aortic model: Average normalized P-V curve measured for the wrapped (blue line) and unwrapped (red line) experiments. Standard deviation is represented by vertical error bars.....	67
<b>Figure 4.16:</b> Experiment C, on fabric aortic model: Distensibility measured for the wrapped (blue line) and unwrapped (red line) experiments. ....	67
<b>Figure 4.17:</b> Detail of the folded shape that the silicon aortic model assumed after wrapping. ....	69
<b>Figure 5.1:</b> Picture of the whole silicon distributed model of the arterial circulation, connected to the pumping system (top). The flow probe is placed around the ascending aorta and the Millar catheter is inserted via a dedicated inlet at the left common iliac artery. ....	76
<b>Figure 5.2:</b> Detail of the model aorta (inlet at the bottom of the picture, iliac bifurcation at the top); the black spots are the measurement locations at which the Millar catheter tip was placed. ....	77
<b>Figure 5.3:</b> Detail of the single AA wrap clamped around the aorta inducing a diameter reduction, placed at location 2 distal to the coronary branches. ....	77
<b>Figure 5.4:</b> Detail of both AA and TA wraps clamped on the arterial model.....	78
<b>Figure 5.5:</b> Detail of outflow reservoirs, seen from the model side (left) and from the outflow volumetric surveys side (right). ....	79
<b>Figure 5.6:</b> Execution of the double wrap experiment; both wraps are in place around the AA and TA, secured with metal clamps in order to induce a 70% diameter reduction at the respective aortic locations.....	81
<b>Figure 5.7:</b> Calculation of $Z_c$ as the slope of the curve (thick line) obtained by linearization of the P-Q curve (thin line loop), considering only the time frame from 10% to 25% of the time between the $P_{min}$ and $P_{max}$ . ....	83
<b>Figure 5.8:</b> Graph of the synchronized pressure profiles (in mmHg) recorded at the AA location, for the unwrapped (blue line), single AA wrapped (red line), and double AA+TA wrapped (green line) configurations, for the 50 bpm - 70 ml HR-SV combination; a reference flow profile (in ml/s) is represented by the purple line.....	85
<b>Figure 5.9:</b> Graph of the synchronized pressure profiles (in mmHg) recorded at the renal artery location, for the unwrapped (blue line), single AA wrapped (red line), and double AA+TA wrapped (green line) configurations, for the 50 bpm - 70 ml HR-SV combination; a reference flow profile (in ml/s) is represented by the purple line.....	85
<b>Figure 5.10:</b> PP amplification measured at 10 different locations along the model, for the 50 bpm – 70 ml HR-SV combination, for the unwrapped (black line), single wrap (red line), and double wrap (green line) configurations. On the left panel, absolute values of PP at every location are represented in mmHg; on the right panel, PP at each location is represented as normalized to the PP value at the inlet for each wrapping configuration. ....	86
<b>Figure 5.11:</b> PP drop (calculated as difference in PP after wrapping) measured at 10 different locations along the model, for the single wrap (left panels) and double wrap (right panels) configurations, for 50 bpm (black line), 65 bpm (red line) and 80 bpm (green line) HR values, for 50 ml (upper row), 60 ml (middle row), and 70 ml (bottom row) SV values.....	87
<b>Figure 5.12:</b> Systolic pressure drop (calculated as difference in SP after wrapping) measured at 10 different locations along the model, for the single wrap (left panels) and double wrap (right panels) configurations, for 50 bpm (black line), 65 bpm (red line) and 80 bpm (green	

line) HR values, for 50 ml (upper row), 60 ml (middle row), and 70 ml (bottom row) SV values. ....	88
<b>Figure 5.13:</b> 3D plot of PP drop (as the difference in PP between wrapped and unwrapped configurations) for the single AA wrapped configuration measured at the AA location, for every HR-SV combination, expressed in % PP of the unwrapped configuration. ....	89
<b>Figure 5.14:</b> 3D plot of PP drop (as the difference in PP between wrapped and unwrapped configurations) for the double AA+TA wrapped configuration measured at the AA location, for every HR-SV combination, expressed in % PP of the unwrapped configuration. ....	89
<b>Figure 5.15:</b> 3D plot of PP drop (as the difference in PP between wrapped and unwrapped configurations) for the single AA wrapped configuration measured at the renal artery location, for every HR-SV combination, expressed in % PP of the unwrapped configuration. ....	90
<b>Figure 5.16:</b> 3D plot of PP drop (as the difference in PP between wrapped and unwrapped configurations) for the double AA+TA wrapped configuration measured at the renal artery location, for every HR-SV combination, expressed in % PP of the unwrapped configuration. ....	90
<b>Figure 5.17:</b> Input impedance modulus (left panel) and phase (right panel) of the arterial model, calculated for the 50 bpm – 70 ml HR-SV combination, for the unwrapped (black line), single wrap (red line), and double wrap (green line) configurations. ....	91
<b>Figure 5.18:</b> Input impedance modulus (left panel) and phase (right panel) of the arterial model, for the unwrapped (black line), single wrap (red line), and double wrap (green line) configurations, calculated for a fixed 50 ml SV and three different HRs: 50 bpm (top row), 65 bpm (middle row), and 80 bpm (bottom row). ....	92
<b>Figure 5.19:</b> Input impedance modulus (left panel) and phase (right panel) of the arterial model, for the unwrapped (black line), single wrap (red line), and double wrap (green line) configurations, calculated for a fixed 60 ml SV and three different HRs: 50 bpm (top row), 65 bpm (middle row), and 80 bpm (bottom row). ....	93
<b>Figure 5.20:</b> Input impedance modulus (left panel) and phase (right panel) of the arterial model, for the unwrapped (black line), single wrap (red line), and double wrap (green line) configurations, calculated for a fixed 70 ml SV and three different HRs: 50 bpm (top row), 65 bpm (middle row), and 80 bpm (bottom row). ....	94
<b>Figure 6.1:</b> Sagittal oblique view of the thoracic aorta using MRI acquisition, illustrating thoracic aortic geometry. AC = average arch curvature; Ant = anterior arch width; H = arch height; L1 = length of the aortic arch; L2 = length of the descending aorta; Post = posterior arch width; and W = arch width. Reproduced from Redheuil <i>et al.</i> (Redheuil et al. 2011) ...	102
<b>Figure 6.2:</b> 3D geometrical realistic model of the aortic arch: unwrapped configuration. The red arrow indicates the inlet. ....	102
<b>Figure 6.3:</b> 3D geometrical realistic model of the aortic arch: panel 1) model type B, shorter wrapping length, 70% D; panel 2) model type A, longer wrapping length, 70% D. Red arrows indicate the inlet. ....	103
<b>Figure 6.4:</b> Example of hexahedral mesh created for the straight models of the aorta. Panel A: whole mesh of the wrapped model characterized by wrapping L of 10 cm and wrapping diameter of 70% D; panel B: detail of the inlet mesh of the model displayed in panel A. ....	104
<b>Figure 6.5:</b> Example of tetrahedral mesh created for the realistic curved models of the aortic arch. Panel A: whole mesh of the wrapped model type B (characterized by a shorter wrapping	

length) and wrapping diameter of 70% D; panel B: detail of the inlet mesh of the model displayed in panel A. ....	105
<b>Figure 6.6:</b> Maximum WSS values (normalized for the UW maximum WSS) calculated for every wrapped configuration: four different wrapping D (90%, 80%, 70%, and 60% of the UW D, displayed on the horizontal axis) and four different wrapping lengths (5 cm in blue, 10 cm in red, 15 cm in green, and 20 cm in purple). ....	107
<b>Figure 6.7:</b> WSS plots (mmHg) on the surface of two wrapped models; top: model characterized by 5 cm wrapping length and 90% D (lower maximum WSS value), presenting maximum values of WSS located at the inlet wall; bottom: model characterized by 20 cm wrapping length and 60% D (higher maximum WSS value), presenting maximum values of WSS located at the proximal edge of the wrapped section. Red arrows indicate the inlet.....	108
<b>Figure 6.8:</b> Velocity profiles (m/s) in two wrapped models. Inlets are on the left of the figure. Top: model characterized by 10 cm wrapping length and 60% D; bottom: model characterized by 10 cm wrapping length and 70% D. A small decrease in diameter from 70% to 60% of the UW diameter induced a marked peak velocity increase (almost 1.5 times). ....	109
<b>Figure 6.9:</b> Velocity profiles (m/s) in the unwrapped model of the aortic arch. The red arrow indicates the inlet. ....	111
<b>Figure 6.10:</b> Velocity profiles (m/s) in the wrapped models of the aortic arch. Red arrows indicate the inlet. Left column: type A models, characterized by longer wrapping length and shorter distance from the inlet; right column: type B models, characterized by shorter wrapping length and larger distance from the inlet. Top row: wrapping diameter 60% of the UW one; middle row: wrapping diameter 70% of the UW one; bottom row: wrapping diameter 80% of the UW one. The combination of different wrapping lengths and diameters produced diverse flow patterns among the models. In every wrapped model the velocity in the AA tract was increased compared to the UW model. A 60% wrapping diameter combined with a short distance of the wrap from the inlet (top left panel) induced the creation of a wide area of flow recirculation immediately distal to the wrapped section of the arch. ....	112
<b>Figure 6.11:</b> Velocity streamlines (m/s) in a wrapped model of the aortic arch: type A model with 60% D. This configuration shows the most irregular streamlines, with areas stagnating flow and flow separation distal to the wrap on the lower side of the arch. The red arrow indicates the inlet. ....	113
<b>Figure 6.12:</b> Velocity streamlines (m/s) in a wrapped model of the aortic arch: type A model with 80% D. This configuration shows the most regular streamlines with no areas of flow recirculation. The red arrow indicates the inlet. ....	113

## List of Tables

<b>Table 3.1:</b> Changes in pressure (PP and SP) and impedance ( $Z_c$ ) values in the ascending aorta, induced by six variations of E and two variations of R. All values calculated as % of the respective reference values (PP100, SP100, $Z_c$ 100, E100, R100). ....	49
<b>Table 4.1:</b> Experiment B: Critical pressure (mmHg) calculated for the 6 different wrapping configurations (1, 2, or 3 wraps, and diameters 70% or 80% of the unwrapped diameter). ....	65
<b>Table 4.2:</b> Experiment B: Average distensibility ( $\text{mmHg}^{-1}$ ) for the 0-50 mmHg pressure range (“folded state” of the aortic model inside the wraps), calculated for the 6 different wrapping configurations (1, 2, or 3 wraps, and diameters 70% or 80% of the unwrapped diameter). ....	66
<b>Table 4.3:</b> Typical values of ascending aortic distensibility measured in human subjects, averaged for six age groups, derived for literature (Redheuil et al. 2010). ....	71
<b>Table 5.1:</b> List of 10 pressure measurement locations along the arterial model. ....	80
<b>Table 5.2:</b> Reproducibility test on PP measurements for unwrapped and wrapped experiment configurations. ....	84
<b>Table 5.3:</b> Difference of $Z_c$ values between the single AA wrapped configuration and the unwrapped one, expressed in mmHg/(ml/s) (absolute difference) and % of unwrapped $Z_c$ (relative difference). ....	95
<b>Table 5.4:</b> Difference of $Z_c$ values between the double AA+TA wrapped configuration and the unwrapped one, expressed in mmHg/(ml/s) (absolute difference) and % of unwrapped $Z_c$ (relative difference). ....	95
<b>Table 6.1:</b> Number of mesh elements obtained for the UW and wrapped configurations. ...	104
<b>Table 6.2:</b> Maximum WSS values calculated for every geometrical configuration of the straight AA model; values are normalized to the max WSS value of the unwrapped straight model. ....	106
<b>Table 6.3:</b> Maximum velocity values calculated for every geometrical configuration of the straight AA model; values are normalized to the max velocity value of the unwrapped straight model. ....	109
<b>Table 6.4:</b> Pressure drops calculated for every geometrical configuration of the straight AA model; values are normalized to the pressure drop value of the unwrapped straight model. .	110
<b>Table 6.5:</b> Maximum velocity values calculated for every geometrical configuration of the aortic arch model: absolute values in m/s (left) and relative values normalized to the max velocity value of the unwrapped model (right).....	114
<b>Table 6.6:</b> Pressure drops calculated for every geometrical configuration of the aortic arch model: absolute values in Pa (left) and relative values normalized to the pressure drop value of the unwrapped model (right). ....	115
<b>Table 6.7:</b> Maximum WSS values calculated for every geometrical configuration of the realistic arch model: absolute values in Pa (left) and relative values normalized to the maximum WSS value of the unwrapped model (right). ....	115

## List of Abbreviations

AA	Ascending aorta
ACE	Angiotensin converting enzyme
AGE	Advanced glycation end-product
AW	Aortic Wrap
C	Compliance
CHD	Chronic heart disease
CFD	Computational fluid dynamic
cfPWV	Carotid-to-femoral PWV
CVD	Cardiovascular disease
D	Diameter
Dist	Distensibility
DP	Diastolic pressure
EAB	Extra-aortic balloon
HR	Heart rate
HY-VET	Hypertension in the Very Elderly Trial
ISH	Isolated systolic hypertension
L	Length of vessel
LV	Left ventricular
MAP	Mean arterial pressure
MRI	Magnetic resonance imaging
NHANES III	The National Health and Nutrition Examination Survey
NO	Nitric oxide
P	Pressure
$P_c$	Critical pressure
PP	Pulse Pressure
PWV	Pulse wave velocity
R	Radius
Re	Reynolds number
SHEP	Systolic Hypertension in the Elderly Program
SP	Systolic pressure
SV	Stroke volume
TA	Thoracic aorta
UW	Unwrapped
v	Velocity
V	Volume
VAD	Ventricular assist device

## List of Symbols

$\alpha$	Womersley number
$\varepsilon$	Tensile strain
$\vartheta$	Phase angle
$\mu$	Blood viscosity
$\pi$	pi constant
$\rho$	Blood density
$\sigma$	Tensile stress
$\varphi$	Angle representing the phase lead of pressure in relation to wall displacement
$\omega$	Angular frequency
$A^*$	Modulus of sinusoidal pressure drop in Womersley equation
$E$	Elastic modulus
$E_{\text{inc}}$	Incremental elastic modulus
$h$	Arterial thickness
$j$	Imaginary unit
$J_0$	Bessel function of order zero
$Q$	Volumetric flow rate
$W$	$\dot{W}$ Total hydraulic work
$\dot{W}_0$	Pulsatile hydraulic work
$y$	Ratio of distance from the axis to the radius of a vessel in the Womersley equation
$Z$	Impedance
$Z_c$	Characteristic impedance
$Z_{\text{in}}$	Input impedance
$Z_0$	Characteristic impedance of every segment of the arterial tree

# Chapter 1

## *Preface*

Stiffening of central elastic arteries caused by ageing plays a major role in the marked increase in central pulsatile pressure observed in the elderly, and ultimately leads to isolated systolic hypertension and congestive heart failure (Nichols et al. 2011). Current anti-hypertensive drug treatments are only partially succeeding in treating hypertension in elderly patients, with 82% of > 50 year-old failing to achieve their systolic pressure target goals (Franklin et al. 2001). This is mainly due to the focus of anti-hypertensive agents on lowering peripheral resistance and wave reflections, while not addressing the origin of raised pulse pressure: the increased arterial stiffness.

To address this clinical challenge, the Aortic Wrap (AW) is a proposed implantable device conceived as a mechanical method to reduce increased stiffness in the aorta. It is hypothesized that by wrapping the stiffened and dilated thoracic aorta, typical of elderly isolated systolic hypertension (ISH) patients, with a highly distensible synthetic band, it is possible to unload the aortic walls by reducing the aortic diameter. Through wall unloading, the pulsatile load will be borne by the wrap and therefore increase distensibility and buffering function of the whole wrapped aortic segment. The AW working concept needs to be investigated via

experimental and computational simulations, in order to assess its efficacy in achieving the desired results, in terms of increased aortic distensibility and aortic pulse pressure reduction.

This thesis will explore four different methodologies used to investigate and provide proof of efficacy of the AW involving *in vitro* and *in silico* experimentation and modelling. In Chapter 2 a comprehensive literature review on the topics of arterial stiffness and ISH is presented; Chapter 3 presents an investigation on the effects of aortic distensibility and diameter changes on pulse pressure and impedance using a multibranched computational 1D model of the arterial circulation; an *in vitro* study on distensibility changes after elastic wrapping performed on synthetic models of the aorta is detailed in Chapter 4; in Chapter 5 an *in vitro* investigation of the AW effects on pulse pressure reduction in a bench-top distributed model of the arterial circulation is presented; Chapter 6 describes two computational fluid dynamic studies performed on 3D models of the aortic arch to evaluate the hemodynamic effects of the AW-associated diameter reduction.



# Chapter 2

## *Background*

### **2.1 Pulsatile hemodynamics**

#### **2.1.1 Arterial structure and function**

Arteries are the vessels that allow to feed tissues of large animals with blood, rich in nutrients and oxygen necessary for survival, and to transport waste products and carbon dioxide, that would otherwise poison the system, away from the tissues. They link the heart, which pumps oxygenated blood from the pulmonary circulation, to the peripheral capillary network where the gas and nutrient exchange with the tissues takes place. (Hall and Guyton 2011; Nichols et al. 2011; Noordergraaf 1978)

The arterial tree has then the fundamental function of converting highly pulsatile blood flow generated by the heart intermittent contractions to the continuous blood flow necessary for optimal diffusion at the organ tissue level. The central arteries, i.e. the thoracic aorta and the proximal branches of the carotid and brachiocephalic arteries, serve the main function of buffering pulsations of the heart's left ventricle: they distend and act as blood reservoir during systole (the myocardial contraction phase) and they retract expelling the blood to the rest of the circulation during diastole (the myocardial distension phase). The abdominal aorta and the

peripheral arteries, instead, act mainly as a conduit to deliver blood to the tissues and can vary their smooth muscle tone in order to modify pulse wave propagation. Finally, the arterioles are the link between arteries and capillaries and vary their calibre to regulate peripheral resistance in order to maintain mean arterial pressure (MAP) and regulate blood flow distribution. (Hall and Guyton 2011; Nichols et al. 2011; Noordergraaf 1978)

This difference in function is reflected by an equally marked difference in structure of the arterial tree. Arterial walls are constituted by three concentric layers: intima, media and adventitia (**Figure 2.1**). The intima is similar at all levels of the arterial tree and it normally consists of one layer of endothelial cells, which line the vascular lumen and are a major factor in arterial function regulation, and a thin layer of collagen and elastin, which separates the intima from the media – the main structural part of the arterial wall and the focus of this thesis. On the outside of the media is the adventitia, which merges with connective tissue surrounding other organs and tissues. The media occupies most of the vascular volume and is structurally different in central and peripheral arteries, thus determining the different mechanical properties of these two sections of the arterial tree; this layer is constituted by organized elastin lamellar structures oriented circumferentially, smooth muscle cells placed parallel to them, and collagen fibres dispersed in the gaps between elastin lamellae. Whereas in central arteries elastin makes up 60% of the total fibrous volume, in peripheral arteries collagen becomes the dominating fibrous element, forming 70%. (Nichols et al. 2011)

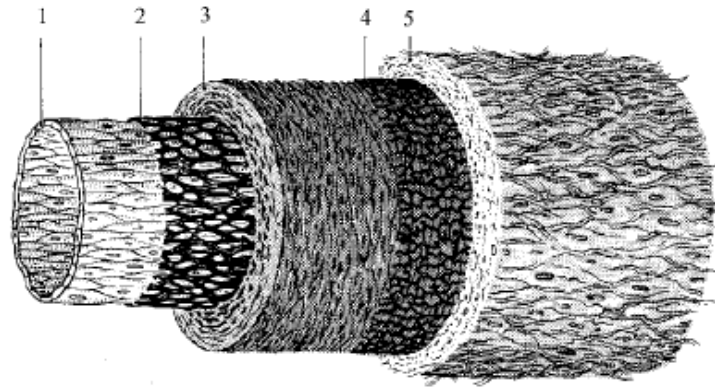


**Figure 2.1:** Different layers of the arterial wall: 1) tunica intima, 2) internal elastic lamina, 3) tunica media, 4) thin medial elastic membrane, 5) tunica adventitia. Reproduced from Kahle *et al.* (Kahle, Leonhardt, and Platzer 1992)

### 2.1.2 Mechanical properties of the arteries

A parameter used to characterise the mechanical properties of a material is the elastic modulus ( $E$ ), or Young's modulus, defined as the ratio of tensile stress ( $\sigma$ ) to tensile strain ( $\epsilon$ ). The elastic modulus of an artery is therefore an index of its structural stiffness; vascular stiffness, though, is also determined by the vessel thickness and diameter. (Noordergraaf 1978; Nichols et al. 2011)

The elastic modulus of elastin ( $3 \times 10^6$  dyne/cm<sup>2</sup>) is three orders of magnitude smaller than that of collagen ( $1000 \times 10^6$  dyne/cm<sup>2</sup>). This factor, combined with the different composition of the medial layer along the vasculature, as introduced in the previous section, explains the markedly distinct mechanical properties of central and peripheral arteries: the arterial elastic modulus increases with increasing distance from the heart (**Figure 2.2**). (Nichols et al. 2011; Nichols et al. 1987)

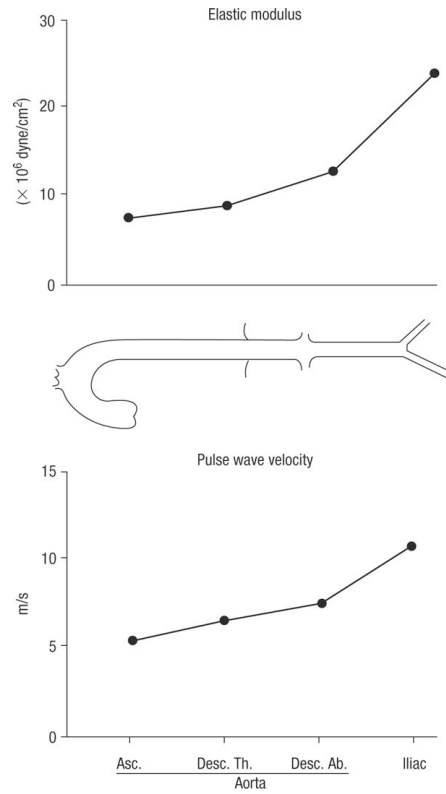


**Figure 2.2:** Elastic modulus and pulse wave velocity measured in the aorta and iliac artery of a young healthy subject; both pulse wave velocity and elastic modulus increase as the distance from the hearth increases. Reproduced from Nichols *et al.* (Nichols et al. 1987)

Moreover, hemodynamic factors have a role in determining central arterial stiffness. Collagen fibres in the media are recruited at higher distending pressures compared to elastin lamellae: at low values of  $\sigma$  (corresponding to low distending pressure), elastin fibres are the only load-bearing structures in the arterial wall, but with increasing pressure more and more collagen fibres are under tension, determining a sharp increase of  $E$  (Armentano et al. 1991; Vlachopoulos, Aznaouridis, and Stefanadis 2006; Okamoto et al. 2002). This pressure-dependant elastic behaviour can be expressed by the concept of incremental elastic modulus ( $E_{inc}$ ), defined as the tangent of the stress-strain curve at a particular value of wall strain (corresponding to a specific value of distending pressure) (**Figure 2.3**) (Milnor 1989). The work of Learoyd and Taylor (Learoyd and Taylor 1966) demonstrated that  $E_{inc}$  increases with

pressure, over the pressure range 50 – 150 mmHg, in both central and peripheral human arteries.

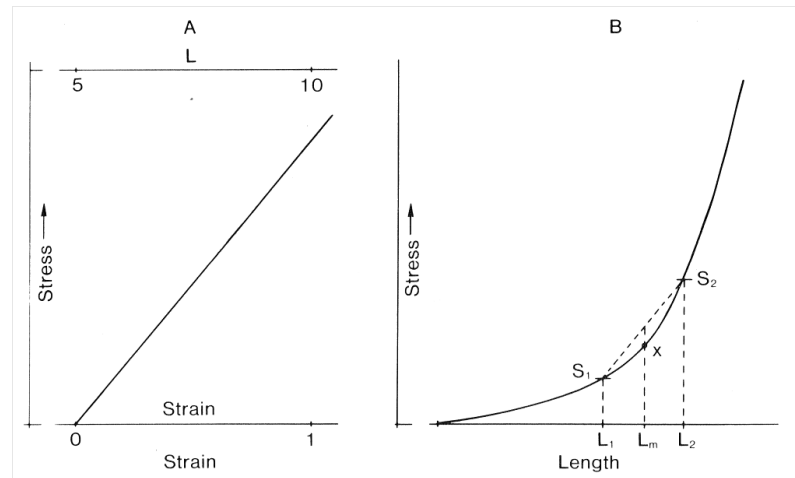


**Figure 2.3:** Linear (left) and non-linear (right) relationships between stress (S) and strain (or length, L).  $E_{inc} = (S_2 - S_1) \cdot (L_m) / (L_2 - L_1)$ . Reproduced from Milnor *et al.* (Milnor 1989)

The composition of the arterial wall and the spatial organization of its fibrous elements thus determine a curvilinear pressure-diameter relationship: as shown by Länne *et al.* (Länne *et al.* 1992), the aortic diameter-pressure curve has an inflection point at pressures around 90 - 110 mmHg, above which it shows marked reduction in steepness (**Figure 2.4**); this biphasic behaviour represents the transition between purely elastin-driven elastic properties to a more stiff behaviour dominated by collagen properties (though capable of being modified by vascular muscle tone).

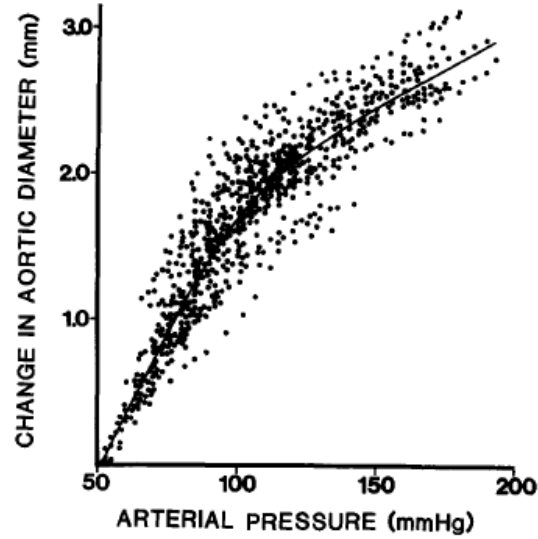


**Figure 2.4:** Pressure diameter curve of the abdominal aorta based on 28 individual recordings taken both at rest and during isometric exercise. Note the inflection at 90-110 mmHg with a stiffer vessel wall above than below. Reproduced from Länne *et al.* (Länne et al. 1992)

The steepness of the pressure-diameter curve represents the compliance (C) of the vessel at any site, i.e. the inverse of stiffness. Arterial compliance is defined as the variation in volume (or diameter,  $\Delta D$ ) occurring for a given variation in pressure ( $\Delta P$ ) at a fixed vessel length; it can be therefore expressed by the following equation:

$$C = \frac{\Delta D}{\Delta P} \quad (1)$$

Distensibility (Dist) is the relative compliance for a given initial volume (or initial diameter,  $D_o$ ), it is the inverse of E, and can be described by:

$$Dist = \frac{1}{D_o} \times \frac{\Delta D}{\Delta P} \quad (2)$$

(Cavalcante et al. 2011; Nichols et al. 2011).

Typical values of Dist for the human ascending aorta (AA) are  $74$  and  $10 \text{ kPa}^{-1} \times 10^{-3}$  for subjects 20-29 years old and  $>70$  years respectively, while carotid Dist is approximately 6 times smaller than AA Dist for younger subjects, but only half for elderly subjects (Redheuil et al. 2010). Age-related changes of central arterial distensibility will be addressed in detail in one of the following sections.

### 2.1.3 Pulse Wave Velocity

Pulse wave velocity (PWV) is defined as the speed of the pulse wave generated by the heart stroke, travelling through the arterial tree and reaching the peripheral arteriolar beds. It is influenced by the properties of blood, i.e. its density, and by those of the arteries, i.e. the arterial wall incremental elastic modulus, and the arterial lumen and thickness. PWV can therefore be expressed by the following equation, also known as the Moens-Korteweg equation (Nichols et al. 2011):

$$PWV = \sqrt{\frac{Eh}{2\rho R_i}} \quad (3)$$

where  $E$  is the arterial wall incremental elastic modulus,  $h$  is the thickness of the artery,  $R_i$  is the internal radius of the lumen, and  $\rho$  is the blood density.

As explained extensively in section 2 of this chapter, PWV is a powerful marker of cardiovascular risk, since it is a measure of arterial stiffness and, therefore, it is an indicator of myocardial afterload, i.e. the load that the heart has to overcome in order to deliver the stroke volume of blood to the tissues of the body (Nichols et al. 2011; Cavalcante et al. 2011).

PWV can be calculated by measuring the time delay between the foot of the pressure wave measured at two distinct arterial locations placed at a known distance apart (**Figure 2.5**). It

can be measured non-invasively by ultrasound technology, applanation tonometry, or brachial pressure cuff systems, making it a very accessible cardiovascular parameter (Pannier et al. 2002).

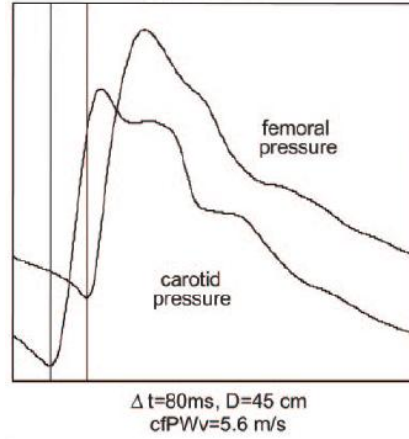


**Figure 2.5:** Carotid-to-femoral PWV (cfPWV) assessed with tonometry in a young subject, calculated with the time delay method ( $\Delta t$  = time delay between the feet of the pressure waves,  $D$  = distance between the measurement locations). Reproduced from Redheuil *et al.* (Redheuil et al. 2010).

An alternative method for measuring local PWV is given by the application of the Bramwell-Hill formula (Bramwell and Hill 1922a; Bramwell and Hill 1922b):

$$PWV = \sqrt{\frac{\Delta P \cdot V}{\Delta V \cdot \rho}} \quad (4)$$

where  $\Delta P$  and  $\Delta V$  are the relative change in pressure and volume, respectively, and  $\rho$  is blood density. Pressure can be measured non-invasively via applanation tonometry, while flow and arterial dimensions can be measured via ultrasound or Doppler techniques (Pannier et al. 2002).

Typical values of PWV for a young individual are around 5 m/s in the ascending aorta, increasing constantly towards the peripheral vasculature, reaching values around 15 m/s in



arteries below the knee (**Figure 2.6**) (Nichols et al. 2011). The variations of PWV with age will be discussed in detail in the following section on age-related arterial stiffening.

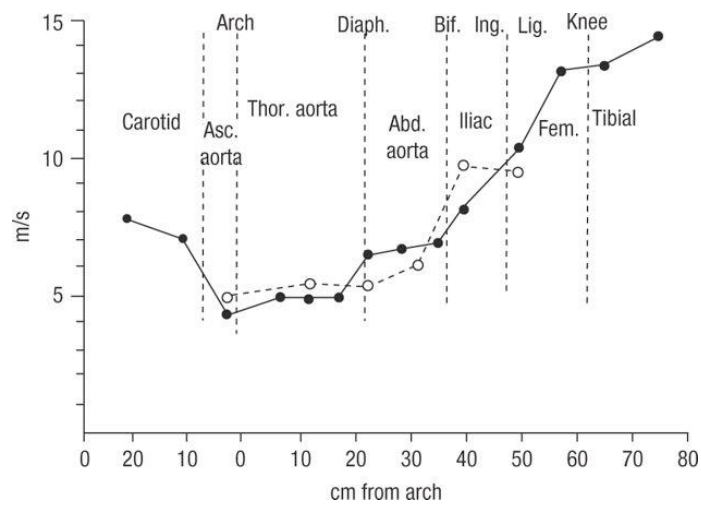


**Figure 2.6:** Progressive increase of PWV with increasing distance from the heart in the dog (solid line) and measured in young adult humans (broken line). Reproduced from Nichols *et al.* (Nichols et al. 2011)

Being an indicator of stiffness, PWV shows a pressure-dependent trend, similarly to compliance and distensibility (Avolio et al. 1983).

Moreover, central PWV increases with age, in accordance with the age-related decrease of distensibility (Avolio et al. 1983; McEniery et al. 2005). The details of this behaviour will be discussed in detail in the following sections of this manuscript.

## 2.1.4 Arterial hemodynamics

Fluid dynamics of the arterial circulation can be efficiently modelled by a set of equations which describe the relationship between blood pressure and flow through the arterial tree. The assumptions necessary to simplify the mathematical problem determine the accuracy of the model in describing real hemodynamics.

Blood can be modelled as a Newtonian fluid, i.e. characterised by constant viscosity; this assumption can reasonably be made for vessels with a diameter > 1mm (as in all major arteries considered in this manuscript) and for normal hematocrit values (up to 45%). Blood viscosity ( $\mu$ ) in such conditions is assumed to be 0.0035 Pa · s at 37 °C. (Nichols et al. 2011; Schmid-Schönbein and Wells Jr. 1971)

The heart acts as a pulsatile pump, pumping blood in spurts through the arterial tree, which can be modelled as a network of viscoelastic thin-walled cylindrical conduits with non-uniform elastic properties. Pressure pulsations are amplified towards the periphery of the network, due to the decreasing distensibility of the arterial walls with distance from the heart, and are then almost completely smoothed at the arteriolar level, so that a continuous flow is reached in the capillary of all but highly vascular beds (i.e. brain and kidneys). (Taylor 1964)

When fluid flows orderly in adjacent layers, which are sliding over each other with different velocity, it is defined as *laminar* flow. When the flow rate increases, the fluid particles start to move in a chaotic way across the cross section of the vessel, transitioning from laminar to *turbulent* flow. The Reynolds number (Re) is a dimensionless indicator of this transition and it is defined as:

$$Re = \frac{vD\rho}{\mu} \quad (5)$$

where v is the average fluid cross-sectional velocity (m/s) in steady flow conditions, D is the lumen diameter (m),  $\mu$  is the dynamic viscosity of the fluid (Pa × s), and  $\rho$  is the fluid density (kg/m<sup>3</sup>). (Nichols et al. 2011)

In order to model the pulsatile pressure-flow relationship in distending elastic conduits, such as the arteries, it had been easier to approach a steady-state rigid-walled configuration first. In steady-state modelling, blood flow is considered to have a constant flow rate. The pressure-flow relationship in a thin-walled cylindrical rigid tube under laminar steady conditions can be described by Poiseuille's equation, as follows:

$$\Delta P = \frac{8\mu L}{\pi R^4} Q \quad (6)$$

where  $\Delta P$  is the pressure drop at the extremities of the tube,  $Q$  is the volumetric flow rate ( $\text{m}^3/\text{s}$ ),  $L$  and  $R$  are the length and the radius of the tube respectively (m), and  $\mu$  is the fluid dynamic viscosity ( $\text{Pa} \times \text{s}$ ).

More realistically, pulsatile conditions have to be taken into account for a more accurate model of the arterial circulation. Womersley, in his seminal work (Womersley 1955; Womersley 1957), solved the Navier-Stokes equations for pulsatile blood flow in cylindrical thin-walled viscoelastic conduits. The longitudinal velocity  $v$  (m/s) of blood is then defined by:

$$v = \frac{A^*}{j\omega\rho} \left( 1 - \frac{J_0(\alpha y j^{3/2})}{J_0(\alpha j^{3/2})} \right) e^{j\omega t} \quad (7)$$

where  $A^*$  is the modulus of the sinusoidal pressure drop over the length of the vessel,  $\rho$  is blood viscosity,  $y$  is defined as  $r/R$  (with  $R$  being the radius of the vessel and  $r$  being the distance from the axis),  $J_0$  is the Bessel function of order zero,  $j$  is the imaginary unit, and  $\omega$  is the frequency. Finally,  $\alpha$  is the Womersley number, defined as follows:

$$\alpha = \sqrt{\frac{R^2 \omega \rho}{\mu}} \quad (8)$$

where all parameters are as defined above.

### 2.1.5 Arterial impedance and cardiac power

The parameter used in hemodynamics to describe the arterial hydraulic load, or the opposition of the arterial network to blood flow, is *impedance* ( $Z$ ), defined as the ratio between pressure and flow in the frequency domain. Impedance is a complex parameter, whose modulus represents the relationship between each pressure and flow harmonic component and whose phase is determined by the delay of said corresponding pressure and flow components. (Nichols et al. 2011; O'Rourke and Taylor 1967; O'Rourke 1976)

Input impedance ( $Z_{in}$ ), defined as  $P/Q$ , is the impedance at the inlet cross section of a particular vascular bed and it represent the impedance of the whole downstream arterial tree; it is determined by local conditions as well as the vascular properties of the distal arterial bed. Characteristic impedance ( $Z_c$ ), instead, is defined as the input impedance of an arterial bed where no wave reflections are present. (Milnor 1989)

Input impedance modulus of the human arterial tree has a typical pattern, characterized by a maximum reached at zero frequency (i.e. the steady-flow component, or resistance), a sharp drop for the first five harmonics, with two minima around 3 and 6 Hz, and then a slow increase and oscillation around the  $Z_c$  value. The impedance phase starts negative, crosses the zero at the frequency corresponding to the first minimum, and then oscillates around a positive value or the zero (**Figure 2.7**). (Taylor 1973; O'Rourke and Taylor 1967; Nichols et al. 2011; Nichols et al. 1977)

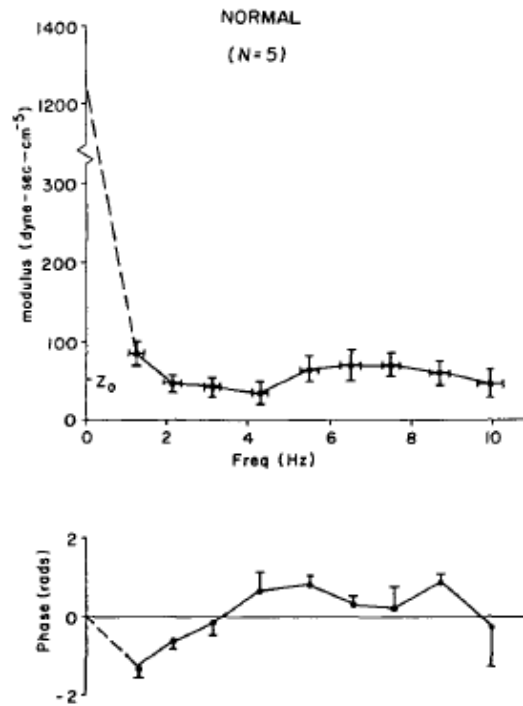


**Figure 2.7:** Average aortic input impedance calculated for five normal adult subjects (vertical and horizontal bars represent standard errors of the means of modulus, phase, and frequency).  $Z_0$  is the estimated characteristic impedance ( $53 \pm 4$  dyn sec/cm<sup>5</sup>) obtained by averaging the moduli above 2 Hz. Reproduced from Nichols *et al.* (Nichols et al. 1977)

The steep fall of impedance modulus after zero frequency and its oscillation around low values at high frequencies can be explained by the elastic non-uniformity of the arterial tree and by wave reflections from scattered arterial terminations (Taylor 1973; Taylor 1966a; Taylor 1966b; Taylor 1967; Taylor 1969). The minima in the modulus result from wave reflections from the peripheral upper and lower body vascular beds (O'Rourke and Taylor 1967).

This specific pattern is optimal for minimizing pulsatile cardiac work, as the impedance modulus is minimal at those frequencies which contain most of the energy of the left ventricular flow wave (Taylor 1965; Taylor 1966b; Taylor 1966a; O'Rourke and Taylor 1967). External cardiac work (or power) can be divided into two components: steady and pulsatile. The steady component is defined as the energy spent by the heart to drive the mean

blood flow to and through the capillaries and is determined by peripheral resistance. Pulsatile work, instead, is the energy dissipated by the oscillatory component of the arterial flow wave and is mainly determined by viscoelasticity of arterial walls, viscosity of blood, and reflections of waves from the periphery (Taylor 1967; Nichols et al. 2011). Pulsatile power ( $\dot{W}_o$ ) can then be described by the following equation:

$$\dot{W}_o = \frac{1}{2} \sum_{n=1}^N (Q_n)^2 Z_n \cos \vartheta_n \quad (9)$$

where the suffix  $n$  indicates the harmonic component considered, varying from 1 to  $N$ , of both the flow wave ( $Q$ ) and the impedance modulus ( $Z$ ) and phase ( $\vartheta$ ). The total cardiac work ( $\dot{W}$ ) can then be defined as:

$$\dot{W} = P_o \times Q_o + \dot{W}_o \quad (10)$$

where  $P_o$  and  $Q_o$  are the mean values of pressure and flow respectively, and their product represents the steady power component. The ratio between pulsatile and total power is an indication of the inverse of the system efficiency and it normally is around 0.2 in human subjects. (Nichols et al. 2011)

## 2.2 Age-related arterial stiffening

### 2.2.1 Arterial aging and arteriosclerosis

Age-related changes in the structure and function of blood vessels are the main risk factors of cardio-vascular disease (Lakatta and Levy 2003a; Lakatta and Levy 2003b). With advancing age, central elastic arteries show increased and diffused stiffness, increased intimal-medial thickness, and dilatation (Virmani et al. 1991). This phenomenon, also referred to as

*arteriosclerosis*, is mainly caused by the degeneration of the medial layer of the arterial wall (Nichols et al. 2011; Cecelja and Chowienczyk 2012; O'Rourke and Hashimoto 2007).

Since the study by Bramwell and Hill in 1922 (Bramwell and Hill 1922b), which demonstrated the increase in arterial PWV with age, numerous studies on arterial function have followed and produced further evidence on age-related central arterial stiffening. (Nichols et al. 2011; Avolio et al. 1983; Dart et al. 1991; Lanne et al. 1994; Sonesson et al. 1993; Smulyan et al. 2001; Hickson et al. 2010; Redheuil et al. 2010)

Although initial studies indicated a linear relationship between age and stiffening of the aorta (Avolio et al. 1983; Smulyan et al. 2001), most recent findings in larger cohorts suggest a non-linear relationship (McEniery et al. 2005; McEniery, Wilkinson, and Avolio 2007; Redheuil et al. 2010; Hickson et al. 2010), with a more marked increase of aortic stiffness after the 5<sup>th</sup> decade of life. In a study by McEniery *et al.* (McEniery et al. 2005) aortic stiffness rose following a second order polynomial curve; aortic PWV (but not brachial PWV) went from a 0.4 m/s increase between the age of 20 and 30 years to a 1.8 m/s increase for 70 to 80-year-old subjects (**Figure 2.8**).

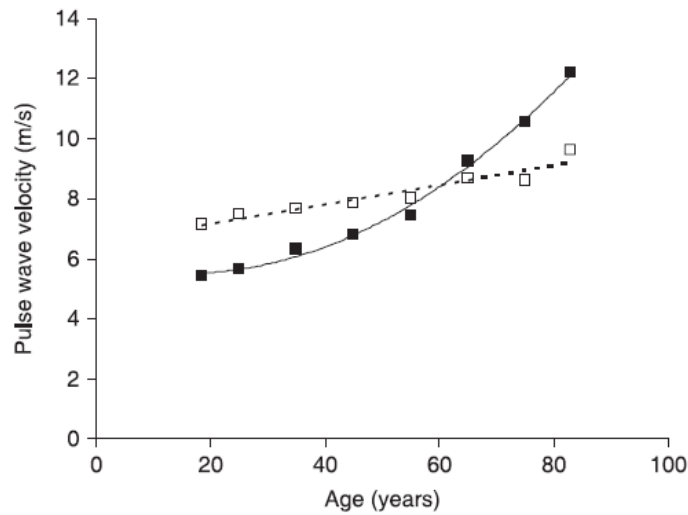


**Figure 2.8:** Age and aortic and brachial pulse wave velocity (PWV) in healthy subjects. Data from the Anglo-Cardiff Collaborative Trial (ACCT) study population. Note the relatively linear relationship for brachial PWV (broken line) compared with the curved relationship for aortic PWV (solid line). Reproduced from McEniery *et al.* (McEniery, Wilkinson, and Avolio 2007)

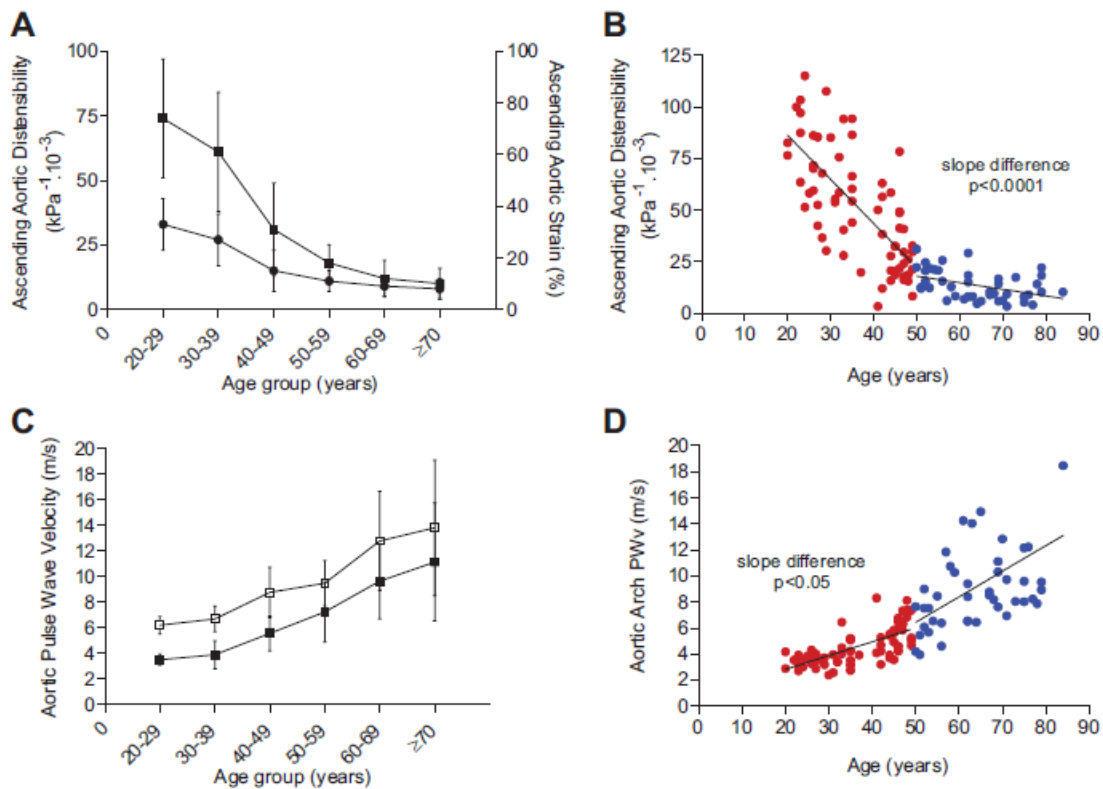


**Figure 2.9:** fig.2 Effect of age on measures of proximal aortic function. A) AA strain (dot) and distensibility (squares) by decades of age. B) AA distensibility (age <50 in red dots and >50 years in blue dots). C) Aortic arch PWV (dark squares) and carotid-to-femoral PWV (open squares) by decades of age. D) Aortic arch PWV (red dots, <50 years of age; blue dots, >50 years of age). Reproduced from Redheuil *et al.* (Redheuil et al. 2010).



The most recent comprehensive investigation on the topic was performed by Redheuil *et al.* (Redheuil *et al.* 2010). Using magnetic resonance imaging (MRI) in healthy subjects, Redheuil's findings indicated a dramatic decrease of AA distensibility between the ages of 20 to 84, with the most prominent drop around 50 years of age; the study showed a >700% reduction in AA distensibility and over a threefold increase in aortic arch PWV (**Figure 2.9**).

Arteriosclerosis, being situated in the media and characterized by dilatation of the central arteries, can thus be sharply differentiated from the other major vascular disease occurring with age, *atherosclerosis*, which is instead a disease of the intima and consists in the formation of plaques in localized areas of the arterial endothelium, with subsequent narrowing of the lumen. As shown by Avolio *et al.* (Avolio *et al.* 1983), age-related arterial stiffening is independent from the prevalence of atherosclerosis and is therefore attributable to the structural changes in the medial layer. (**Figure 2.10**)

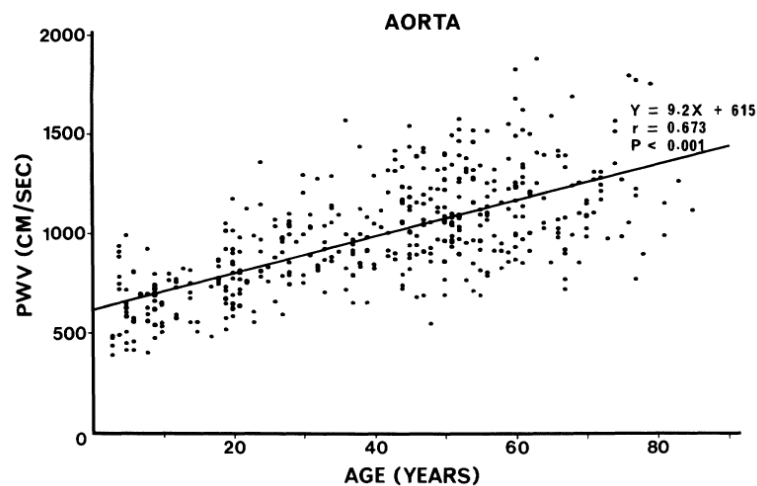


**Figure 2.10:** Aortic PWV measured between base of the neck and groin for all subjects (both male and female subjects) between ages 3 and 89 years. Individual values were determined as the average of 10 pairs of pulses simultaneously recorded with identical transcutaneous Doppler transducers. Reproduced from Avolio *et al.* (Avolio *et al.* 1983).

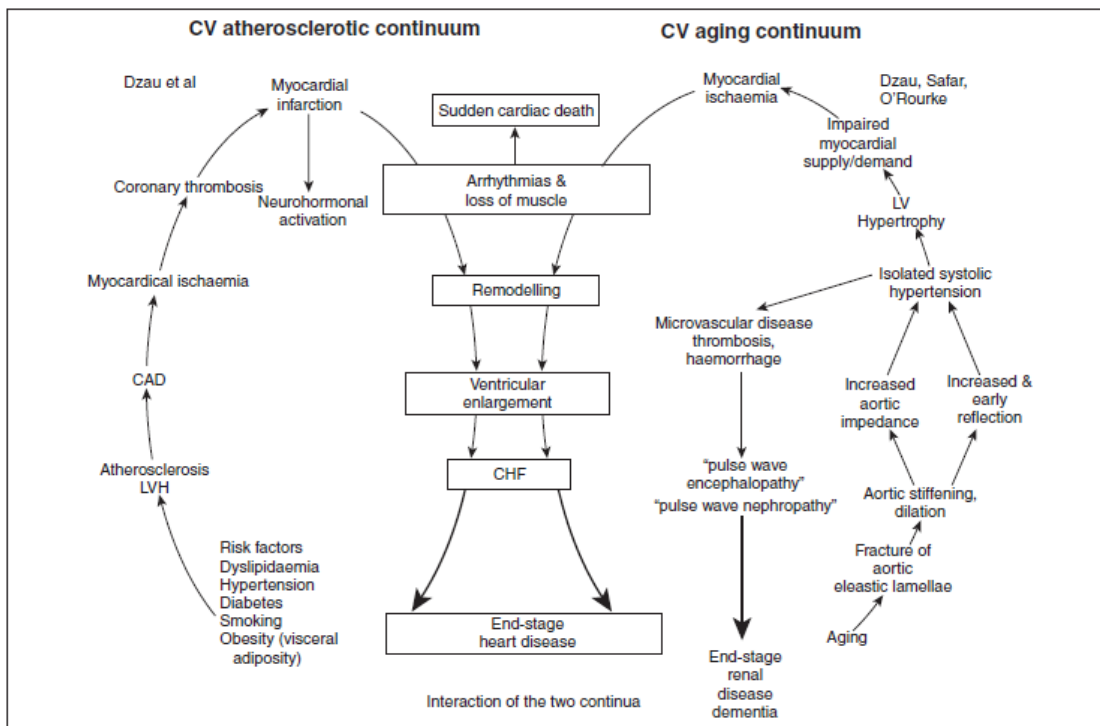


**Figure 2.11:** Two faces of the cameo: the Cardiovascular Continuum (left) and the Aging Continuum (right), and their interaction. Reproduced from O’Rourke *et al.* (O’Rourke, Safar, and Dzau 2010).

Arteriosclerosis and atherosclerosis have very distinct causes and vascular downstream effects, but can interact and lead to common effects, such as left ventricular (LV) hypertrophy, myocardial ischemia, cardiac failure, and end-stage heart disease. An elegant schematic of the distinctions and interactions of atherosclerosis and vascular aging can be found in the “extended cardiovascular continuum” diagram by O’Rourke (O’Rourke, Safar, and Dzau 2010) (**Figure 2.11**) which integrates the predominantly atherosclerotic “cardiovascular continuum” diagram by Dzau *et al.* (Dzau *et al.* 2006a; Dzau *et al.* 2006b) with the arteriosclerotic processes caused by vascular aging, while also providing a logical explanation of a link between aortic arteriosclerosis and small vessel disease in brain and kidney.

### 2.2.2 Age-related arterial stiffening mechanisms

Due primarily to cyclic fatigue caused by heart pulsations, which expand the arterial lumen of the central elastic arteries of about 10% with each pulse, the elastin lamellae in the medial layer of the arterial wall become thinner and fragmented **Figure 2.12**. Elastin degradation can be considered very similar to the common “wear and tear” mechanism observable in elastic material components of technical machinery. (Nichols et al. 2011)

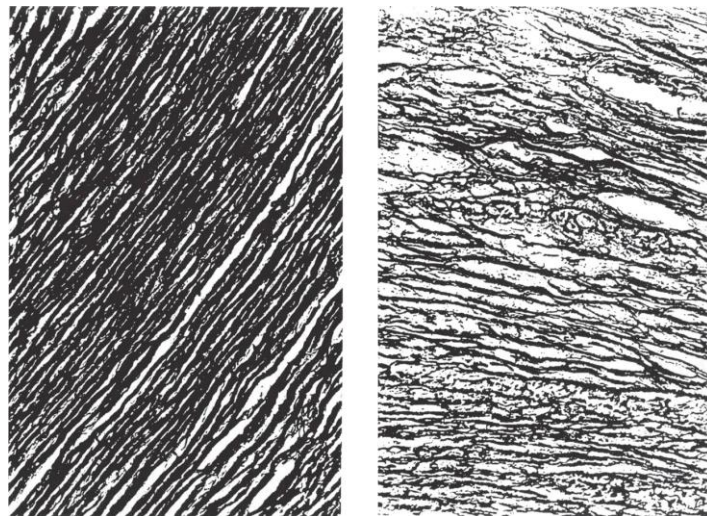


**Figure 2.12:** Comparison of the arterial wall elastin composition in a child (left) with that in an elderly adult (right). Stain: Orcein and Gieson, magnification  $\times 450$ . Prepared by P Lauren, reproduced from O'Rourke *et al.* (O'Rourke et al. 1987). The wall of the older human is disorganized as a consequence of fraying and fracture of the elastic lamellae and loss of muscle attachments, together with increase in collagen fibres and mucoid material.

The progressive fractures of the elastin lamellae in aging arteries cause the pulsatile load to be transferred increasingly to the stiffer collagen component of the medial arterial layer, thus engaging collagen fibres at lower strains when compared to young arteries. This load-bearing shift induces the steepening of the arterial wall stress-strain curve, ultimately increasing the stiffness of the arterial wall (**Figure 2.13**). (McEniery, Wilkinson, and Avolio 2007; Nichols et al. 2011)

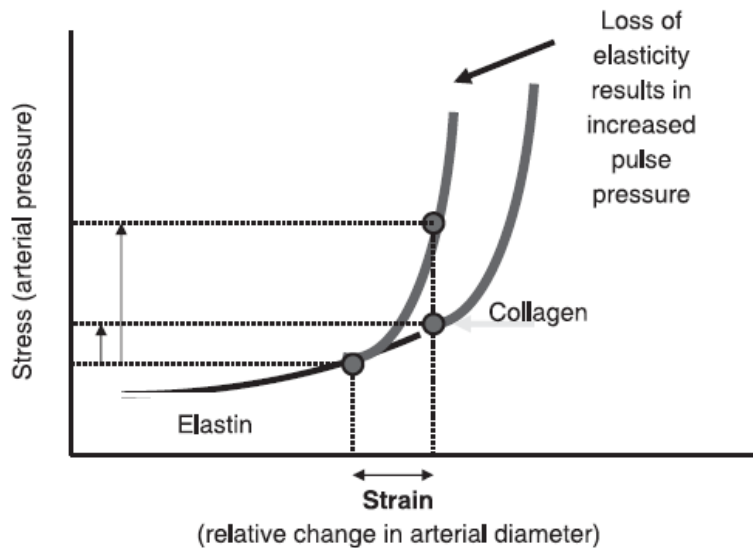


**Figure 2.13:** Stress–strain relationship of the human aorta. Non-linear relationship between arterial stress (pressure) and strain (change in relative diameter). At lower strains, the stress is taken up predominantly by the elastin fibres. At higher strains, the stress is taken up by the stiffer collagen fibres. The effects of age or loss of arterial elasticity are generally to engage the collagen fibres at lower strain, hence effectively increasing pulse pressure for the same strain (as indicated by the arrows). Reproduced from McEniery *et al.* (McEniery, Wilkinson, and Avolio 2007).

Based on extensive experimental evidence, O’Rourke *et al.* (O’Rourke and Hashimoto 2007) theorised that the elastin fragmentation process in human central arteries is first apparent at about 30 years of life (after around 1 billion pulsation cycles) and progresses with age, to complete medial disorganization at age 80 after approximately 3 billion cycles. This theory is supported by the fact that elastin is mainly inert in the body and remains unchanged for decades (Wagenseil and Mecham 2012). This fact, a well established engineering theory, associated with decrease in elastin synthesis and activation of proteolysis, determines the mostly “irreversible” nature of the aging process of central arteries. (O’Rourke and Hashimoto 2007)

Arterial stiffening with age is not noticeable in peripheral, more muscular arteries, where the lumen expansion at each cycle is far smaller than in the central elastic arteries, and therefore the cyclic strain on the elastin lamellae is much lower (Nichols *et al.* 2011; Boutouyrie *et al.* 1992). Neither is age-related stiffening observable in the arteries of experimental mammals,

for similar reasons; these animals have a much shorter lifespan and therefore reach a lower pulsation cycle number, never reaching the elastin fibres “breaking point” due to fatigue.

In addition to elastin degradation, other biochemical processes occur in the medial layer of the aging arterial wall, which may contribute to arterial stiffening: decrease in elastin synthesis, fibrous remodelling, increased calcification, increased collagen deposition, and formation of non-enzymatic cross-links across collagen fibres (McEniery et al. 2005; McEniery, Wilkinson, and Avolio 2007; Yu and Blumenthal 1965; Najjar, Scuteri, and Lakatta 2005). The latter mechanism is of particular therapeutic interest and was the object of several recent studies: it has been proven that the cross-links development between adjacent collagen fibrils, by formation of advanced glycation end products (AGEs), which increases with age, determines increased arterial stiffness in animal models (Vaitkevicius et al. 2001; Wolffenbuttel et al. 1998) and in humans (Kass et al. 2001).

Furthermore, recent studies have demonstrated that levels of endothelial nitric oxide (NO) modulate arterial stiffness, thus suggesting that the observable decrease in NO production with age may be an additional determinant of age-related arterial stiffening (McEniery, Wilkinson, and Avolio 2007; Schmitt et al. 2005). The mechanisms underlining this effect are thought to be the regulation of vascular smooth muscle tone (Lakatta and Levy 2003b) and the implication of NO in the modification of the extracellular matrix structure (Jung et al. 2013; Avolio et al. 2011). Alternatively demonstrated levels of NO in the media may be due to greater loss in the greater transit distance between endothelial cells and media in aged arteries (personal communication with M. O’Rourke).

### 2.2.3 Functional effects of arterial stiffening

The age-related increase in stiffness of central elastic arteries, and in particular the ascending aorta, causes impairment in the arterial function of buffering heart pulsations. The decreased aortic compliance determines a rise in aortic characteristic impedance, which heads to increased aortic input impedance modulus at most harmonic components (O'Rourke and Hashimoto 2007) (**Figure 2.15**). The work of Nichols *et al.* (Nichols et al. 1985) showed that aortic characteristic impedance measured in healthy subjects had a 134% increase within the 20 to 60 age range.

The increased arterial impedance, coupled with unchanged ventricular ejection, determines a concomitant increase in aortic pulse pressure and consequently a rise in aortic systolic pressure. The alteration in diastolic pressure varies: it can decrease if mean arterial pressure is unchanged, or it remains in the normal range if there is a rise in mean arterial pressure due to increased peripheral resistance. (O'Rourke 1976)

Stiffening of the central elastic arteries also determines a higher central PWV, which causes a return of pulse wave reflections in late systole instead of diastole (unlike what happens in the young healthy cardiovascular system). This causes the reflected pressure peak to overlap the systolic ejection peak, thus further increasing systolic pressure (**Figure 2.14**). In addition, the lack of reflection peak in diastole further decreases mean diastolic pressure. Moreover, the increased aortic PWV determines a steeper rise of the pressure wave in early systole, when wave reflections are not present. (O'Rourke and Hashimoto 2007; Nichols et al. 2011)



**Figure 2.14:** Pressure waveforms synthesized for the ascending aorta from the measured brachial artery waveforms in 3 women of the same family—an 18-year-old at left, a 48-year-old at centre, and a 97-year-old at right. Pulse pressure is increased almost 4-fold in the ascending aorta. Reproduced from O’Rourke and Hashimoto (O’Rourke and Hashimoto 2007).

In the frequency domain, the increased PWV corresponds to a shift “to the right” of the aortic input impedance modulus and phase spectra, with the modulus minimum peak being at roughly double the frequency for the old stiffened aorta compared to the corresponding peak in the young aorta (**Figure 2.15**). The combined effects of increased characteristic impedance and rightward shift of the impedance modulus spectrum contribute to a four-fold increase of aortic impedance modulus at heart rate frequency between the ages of 20 and 80 years. (O’Rourke and Hashimoto 2007; Nichols et al. 2011)

Central arterial stiffening then, through increased aortic characteristic impedance and higher PWV, determines a rise in pulse pressure amplitude and systolic pressure, with a decreased or unchanged diastolic pressure, which result in the onset of isolated systolic hypertension. (Nichols et al. 2011)

The increase in LV afterload associated with augmented mean systolic pressure and increased pressure gradient in early systole lead to LV hypertrophy, LV concentric remodelling, and therefore overall increased myocardial blood requirements and metabolic needs (O’Rourke, Safar, and Dzau 2010; Braunwald 1969). These changes induce a slower and prolonged contraction and delayed relaxation of the left ventricle, causing a longer systolic ejection

period. This, combined with the reduced mean diastolic pressure, determines a decreased coronary perfusion, which exacerbates the myocardial metabolic impairment caused by increased oxygen requirements (O'Rourke, Safar, and Dzau 2010).

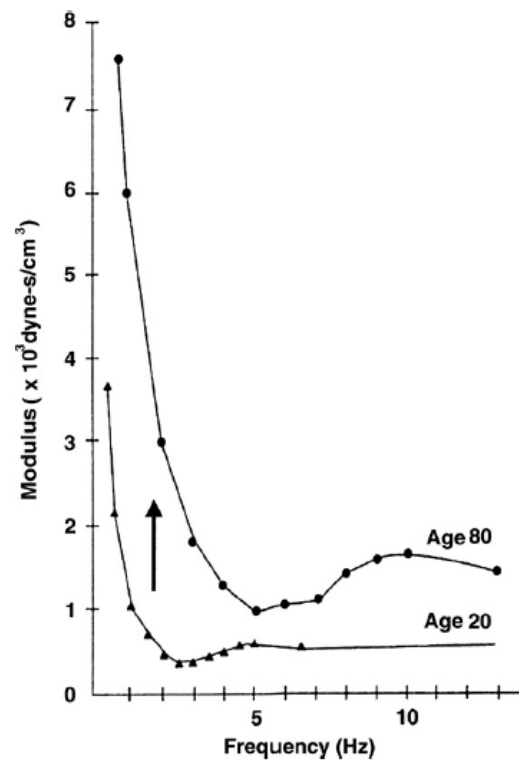


**Figure 2.15:** Ascending aortic impedance shown schematically in a young 20-year-old and in an 80-year-old human subject showing the effect of doubling of characteristic impedance (older curve set higher) and early return of wave reflection (first minimum at double the frequency). In consequence of both, impedance modulus at heart rate frequency is increased 4-fold. Reproduced from Nichols *et al.* (Nichols et al. 2011)

This cascade of changes in the hemodynamics and biology of the cardiovascular system eventually lead to myocardial hypo-oxygenation, congestive heart failure, and potentially chronic heart disease (CHD) and death. (O'Rourke, Safar, and Dzau 2010; Katz 1994)

A further consequence of augmented pulsatility in the central arteries is the transmission of such increased pulse to peripheral arterial beds, especially those characterized by high resting blood flow, such as the brain and the kidneys (**Figure 2.16**). This high peripheral pulsation



causes microvascular lesions: the high shear and tensile stress in the smaller organ arteries induce endothelial damage, inflammation, thrombosis, and micro-ruptures of the vessels (O'Rourke, Safar, and Dzau 2010; O'Rourke and Safar 2005; Safar, Nawar, and Plante 2007; Franklin 2012). In the brain, this microvascular damage is associated with increased white matter lesions and can eventually lead to pulse wave encephalopathy in the elderly, stroke, cognitive impairment, and dementia (Bateman 2002; Henry Feugeas et al. 2005); in the kidneys, it can lead to proteinuria and chronic renal disease (O'Rourke and Safar 2005; Franklin 2012). Therefore, decreasing aortic stiffness and high pulse pressure in the central arteries can positively affect, or prevent, cerebral and kidney dysfunction typical of old age (Hirata et al. 2006; Dufouil et al. 2005).

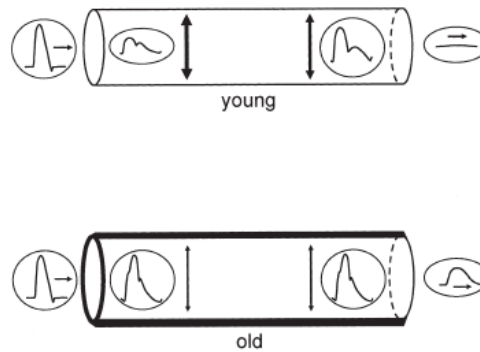


**Figure 2.16:** Simple tubular models of the arterial system, connecting the heart (left) to the peripheral circulation (right) in a young (top) and old (bottom) subject. In the young subject, the tube is distensible, whereas in the old subject it is stiff. The distal end of the tube constitutes a reflection site where the pressure wave travelling down the tube is reflected back to the heart. The wave travels slowly in the young distensible tube so that the reflected wave boosts pressure in diastole when it returns to the proximal end. The wave travels faster in the old stiffer tube, returns earlier, and boosts pressure in late systole. Flow input from the heart is intermittent in both young and old subjects. In the young subject, pulsations are absorbed in the distensible tube so that outflow is steady or almost so. In the old subject with stiff tube, pulsations cannot be absorbed, and so output from tube into peripheral microvessels is pulsatile. Reproduced from O'Rourke and Hashimoto (O'Rourke and Hashimoto 2007).

## 2.3 Isolated Systolic Hypertension

### 2.3.1 ISH and arterial stiffness

Hypertension, defined as abnormally elevated blood pressure, affects approximately one billion people worldwide, with higher prevalence in population over 50 years of age (Franklin 2012; Chobanian et al. 2003). Hypertension is an important determinant of cardiovascular morbidity and mortality. (Nichols et al. 2011)

Isolated systolic hypertension (ISH) is a sub-class of hypertension, defined by values of brachial systolic pressure (SP) above 140 mmHg and brachial diastolic pressure (DP) lower than 90 mmHg. ISH is the most common form of hypertension in the elderly, with a prevalence of 80% in the >50 year-old population (**Figure 2.17**). (Franklin et al. 1997; Franklin et al. 2001; Franklin 2012)

ISH is markedly distinct from mixed hypertension, which is instead characterized by high values of both brachial SP and DP (>140 mmHg and >90 mmHg, respectively); mixed hypertension is induced by a rise in mean arterial pressure (MAP) and affects the majority of untreated hypertensive population below the age of 50 (**Figure 2.17**). (Franklin et al. 2001; Nichols et al. 2011)

The difference between these two typologies of hypertension lies in the biomechanical factors that generate them: while the rise in MAP in mixed hypertension generally derives from increased peripheral resistance, ISH is instead mainly driven by a rise in pulse pressure (PP) caused by the age-related increase in central arterial stiffness. (McEniery, Wilkinson, and Avolio 2007; Nichols et al. 2011)

Patients with ISH have an increased risk of stroke, myocardial infarction, and congestive heart failure, and the augmented PP typical of ISH has been associated with increased risk of cardiovascular mortality (Kostis et al. 2001). ISH is therefore a major risk factor for cardiovascular disease and mortality (SHEP 1991; Rutan et al. 1988)

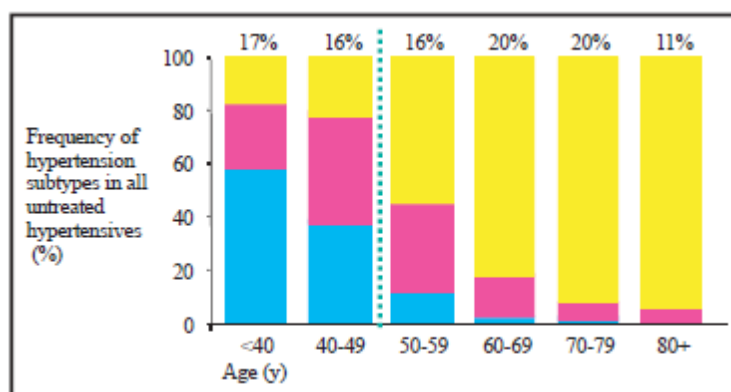


**Figure 2.17:** Frequency distribution of untreated hypertensive individuals by age and hypertension subtype. The numbers at the tops of the bars represent the overall percentage distribution of all subtypes of untreated hypertension in the age group (the Third Report of the National Health and Nutrition Examination Survey, 1988–1994). Isolated diastolic hypertension (systolic blood pressure [SBP] <140 mm Hg and diastolic blood pressure [DBP] >90 mm Hg) shown in yellow, systolic-diastolic hypertension (SBP >140 mm Hg and DBP >90 mm Hg) shown in red, and isolated systolic hypertension (SBP >140 mm Hg and DBP <90 mm Hg) shown in aqua. Reproduced from Franklin *et al.* (Franklin 2012).

Similarly, age-related arterial degradation that underlies the onset of ISH is considered to be an important independent determinant of cardiovascular morbidity and mortality. In particular, aortic stiffness is a major marker of cardiovascular risk: it has been shown to have independent predictive value for cardiovascular and all-cause mortality, coronary events, and fatal strokes in hypertensive, patients with type 2 diabetes, end stage renal disease patients, elderly subjects, and the general population. (Safar 2007; Mitchell et al. 2010; Charalambos Vlachopoulos, Aznaouridis, and Stefanadis 2010; Laurent et al. 2006)

The Framingham heart study, started in 1948, brought to light the age-related nature of ISH, showing its increased prevalence with advancing age. In a cohort of normotensive and

untreated hypertensive subjects belonging to the Framingham study, Franklin *et al.* (Franklin *et al.* 1997) demonstrated that SP increases progressively with age, whereas DP increases in the first 20 years, reaches a plateau, and then starts to decrease after the sixth decade; these patterns of SP and DP determine a steep increase of PP after 50 years of age, consistently with the age-related increase in central arterial stiffness (**Figure 2.18**). Furthermore, the study proved that the age-related increase in SPB and PP is higher in subjects with higher baseline SP.

Thus, ISH and central arterial stiffness (in particular aortic stiffness) go hand in hand as both risk factors and manifestations of cardiovascular disease in the old population. As explained in the previous section on arterial stiffness, ISH is the natural consequence of increased pulsations derived from central arterial age-related stiffening, but it is also a determinant of further arterial stiffening as higher blood pressure accelerates the vascular damage responsible for the stiffening itself (Franklin 2012; Franklin *et al.* 1997). ISH can therefore be seen as an accelerated form of arterial aging (Nichols *et al.* 2011).

### **2.3.2 Current treatments of ISH**

Since the evidence presented by the Systolic Hypertension in the Elderly Program (SHEP) study in 1991 and the Hypertension in the Very Elderly Trial (HY-VET) in 2008, it is well established that treatment of ISH is beneficial at any age and decreases morbidity and mortality (SHEP 1991; Perry *et al.* 2000; Franklin 2012; Beckett *et al.* 2008). Anti-hypertensive treatment decreases the incidence of CVD, stroke, congestive heart failure, renal insufficiency, and coronary artery disease (SHEP 1991; Perry *et al.* 2000; Kostis *et al.* 1997; Kostis *et al.* 2001; Safar 2007). SHEP showed that anti-hypertensive treatment in ISH patients above 60 years of age decreased the incidence of stroke by 36% and of cardiovascular events

by 32%, with a concomitant average decrease in pulse pressure of 18 mmHg. (SHEP 1991; Perry et al. 2000)

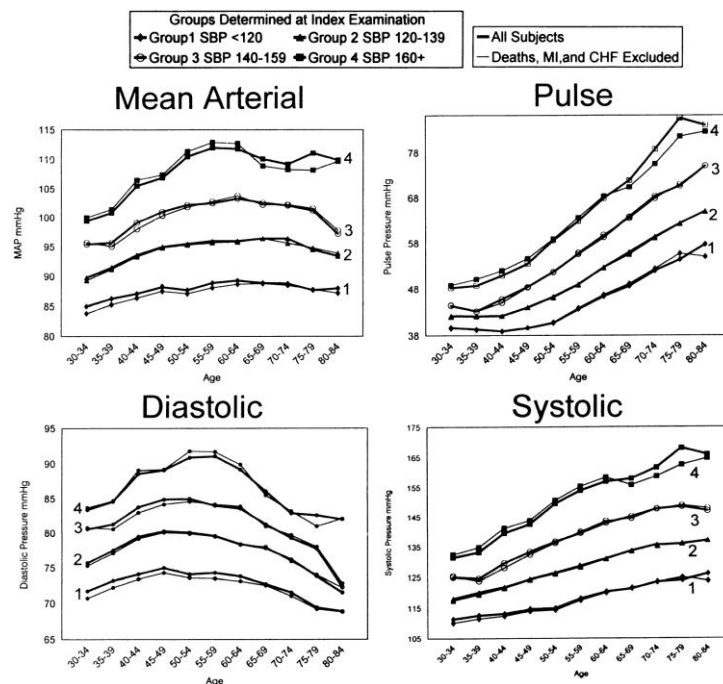


**Figure 2.18:** Arterial pressure components by age: group averaged data for all subjects and with deaths, myocardial infarction, and chronic heart failure excluded. Averaged blood pressure levels from all available data from each subject within 5-year age intervals (30 to 34 through 80 to 84) by SBP groupings 1 through 4. Thick line represents entire study cohort (2036 subjects); thin line represents study cohort with deaths and nonfatal myocardial infarction and chronic heart failure excluded (1353 subjects). Reproduced from Franklin *et al.* (Franklin et al. 1997).

Yet, ISH presents a high percentage of treatment-resistance: according to the National Health and Nutrition Examination Survey (NHANES III) results, 82% of >50 year-old treated hypertensive patients failed to achieve their SP target goal (Franklin et al. 2001). This low rate of success of anti-hypertensive drugs on elderly patients can be explained by the biomechanical nature of ISH onset. Current hypertension treatments, especially angiotensin converting enzyme (ACE) inhibitors, are aimed at vasodilatation of muscular arteries in order to lower arterial peripheral resistance, therefore inducing a decrease in MAP; this can also passively decrease aortic stiffness mainly by shifting the “working point” of the aortic stiffness pressure dependency curve towards the left, where stiffness is lower, therefore slightly decreasing PP (O’Rourke, Safar, and Dzau 2010; Safar 2007). Moreover, vasodilators

and nitrates have been proven effective in lowering the peripheral wave reflection coefficient, thus reducing the magnitude of the reflected pressure wave and ultimately decreasing SP (London et al. 2004; Safar 2007; O'Rourke and Nichols 2005; Latson et al. 1988).

Nevertheless, the pressure-lowering effect of current anti-hypertensive drugs has a limited effect on ISH patients because these drugs act on peripheral resistance and reflection coefficient but do not affect the actual cause of the augmented SP, which is increased PP driven by higher aortic stiffness (Franklin 2012; O'Rourke and Nichols 2005; O'Rourke, Safar, and Dzau 2010). To achieve a fully successful ISH treatment, thus, it seems more effective to restore higher central elastic stiffness, i.e. shifting the aortic pressure-volume curve towards “young” values, achieving lower pressures for similar ventricular ejection values (**Figure 2.19**).

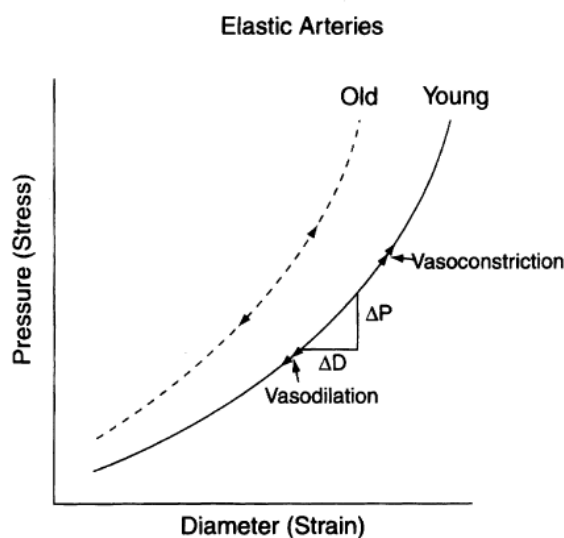


**Figure 2.19:** Pressure (P)-diameter (D) or stress-strain relations for elastic arteries. Elastance can be estimated as the slope ( $\Delta P/\Delta D$ ) of the pressure-diameter curve. With advancing age the curve for elastic arteries shifts to the left, indicating increased elastance for all diameters. Drugs have little direct effect on elastic arteries; however, they do have a passive effect. Vasoconstrictor drugs cause an increase in pressure, diameter and elastance while vasodilator drugs cause a decrease in pressure, diameter and elastance. The pressure-diameter curve does not shift. Reproduced from Nichols *et al.* (Nichols and Edwards 2001).

Drugs that act by delaying or reversing age-related damage to the arterial walls are then the best candidate to successfully treat resistant ISH, rather than those which act only on lowering

peripheral resistance (Lakatta and Levy 2003a; O'Rourke and Nichols 2005). As explained in the previous section on age-related aortic stiffening mechanisms, degenerative changes in elastin structure in the aortic media are irreversible due to the inert nature of elastin in the medial layer; therefore elastin changes in the aorta are unlikely to be potential targets for treatment (O'Rourke, Safar, and Dzau 2010; O'Rourke and Nichols 2005).

On the other hand thought, AGEs cross-links between collagen fibres, which are also implicated in the age-related stiffening of aortic walls, can be targeted; it has thus been suggested that cross-link breakers, i.e. anti-AGE agents, are a potential treatment strategy to decrease arterial stiffness in old patients (Lakatta and Levy 2003a; McEniery 2006; Najjar, Scuteri, and Lakatta 2005). Anti-AGE agents could then “reverse” the age-related arterial stiffening process, in contrast with the “irreversibility” theory proposed by the mechanistic view which considers arterial stiffening as a mere consequence of elastin fibres “wear and tear”. An anti-AGE agent, ALT-711, has been shown to decrease PP in experimental animals and human subjects (Vaitkevicius et al. 2001; Wolffenbuttel et al. 1998; Kass et al. 2001; Safar 2007), although results are not sizable and further studies are limited (O'Rourke and Nichols 2005).

## **2.4 The Aortic Wrap**

### **2.4.1 What is the aortic wrap**

As explained in the previous section, age-related increase in stiffness of the central elastic arteries, and in particular the aorta, is the major determinant of isolated systolic hypertension, and consequently of cardiovascular morbidity and mortality. Both ISH and increased aortic stiffness have been strongly associated with increased risk of heart failure, stroke, and renal disease (Nichols et al. 2011). Therefore, the high percentage of anti-hypertensive treatment

resistance among ISH patients over 60 years is a concern and a therapeutic challenge that needs to be addressed.

The novel concept proposed in this thesis, and originally introduced by Iliopoulos in 2006, is the Aortic Wrap (AW): a new therapeutic device able to restore high levels of aortic distensibility and thus reduce central PP, ultimately aiming at treating ISH and congestive heart failure.

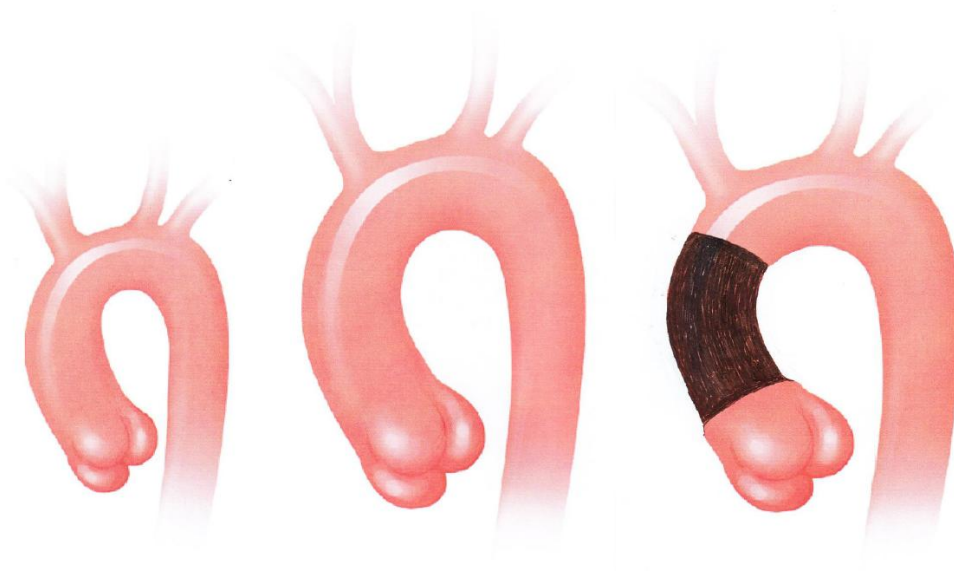


**Figure 2.20:** Scheme of the Aortic Wrap design concept: a young thoracic aorta (left), an old dilated and stiffened thoracic aorta (centre), and an old aorta (right) in which the ascending aortic lumen is restored to young values by means of the Aortic Wrap (in black).

The AW basic principle is the concept of *unloading*: by surgically clipping a piece of elastic distensible material (the AW) around the AA and decreasing the vessel lumen by collapsing the aortic wall inside the AW, it should be possible to unload the vessel walls and shift the pulsatile load to the AW (**Figure 2.20**); this load-bearing shift allows the distensible wrap to better buffer the heart pulsation, mimicking a young distensible aorta. It is hypothesized therefore that the AW will then be able to decrease PP and SP in the aorta, thus reducing the myocardial afterload and the pulsatile power needed by the heart to deliver the stroke volume.



The potential of the AW lies in the fact that it tackles ISH by acting on its core cause: age-related increased arterial stiffness. This factor differentiates the AW from the great majority of current anti-hypertensive therapies, which only target vascular peripheral resistance and/or peripheral wave reflection by vasodilatation of small muscular arteries. It is hypothesized that the central action of the AW will affect the aortic pulse wave markedly by increasing arterial characteristic impedance. It is expected that the AW will restore a “younger” distensibility in the old stiffened aorta, decreasing PP without impacting on peripheral resistance or MAP. This will ultimately benefit elderly ISH patients with stiffened and dilated thoracic aortas who display resistance to common pharmaceutical anti-hypertensive treatments; similarly, the other main potential clinical target are patients affected by heart failure presenting age-related aortic stiffness.

#### **2.4.2 Comparison with commercial device-based treatments of heart failure**

The AW can be compared to current biomedical implantable devices aimed at treating heart failure, defined as ventricular assist devices (VADs). In particular, the intra- and extra-aortic inflatable counterpulsation devices are of interest.

The intra-aortic balloon counterpulsation pump, first devised in 1962 (Moulopoulos, Topaz, and Kolff 1962), consists of a synthetic balloon inserted in the thoracic descending aorta; it is deflated during systole, thus lowering myocardial afterload and increasing forward blood flow, and it is inflated during diastole, promoting coronary perfusion and myocardial oxygenation (**Figure 2.21**).

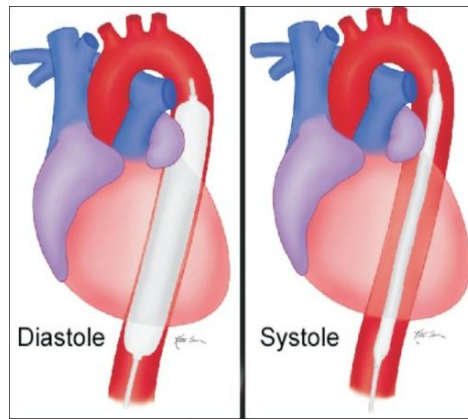


**Figure 2.21:** Schematic diagram of the intra-aortic balloon pump inserted in the thoracic aorta, operating during diastole (left) and systole (right).

The extra-aortic balloon (EAB), also known with the commercial name C-Pulse (Sunshine Heart, Eden Prairie, USA), consists of an inflatable cuff placed around the ascending aorta, which is inflated in diastole and deflated in systole, with a similar mechanism to the intra-aortic balloon pump (**Figure 2.22**). EAB counterpulsation showed augmentation of coronary flow and reduction of LV afterload in preliminary studies on patients affected by heart failure, but its safety and efficacy need to be further investigated in larger clinical trials. (Legget et al. 2005; Hayward et al. 2010; Mitnovetski et al. 2008)

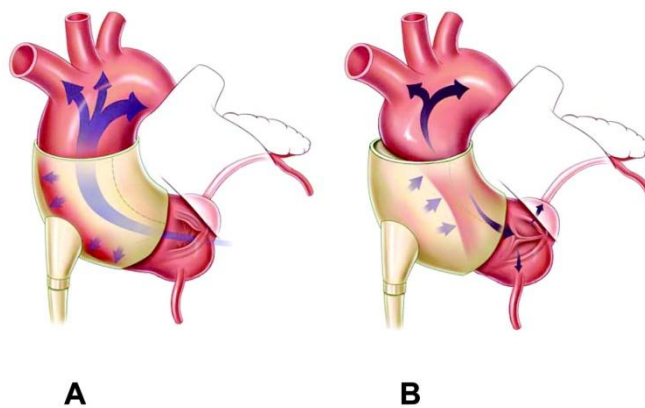


**Figure 2.22:** Schematic diagram of the extra-aortic balloon counterpulsation device. A) Deflation during diastole and B) inflation during systole. Reproduced from Legget *et al.* (Legget et al. 2005)

Compared to these devices, the AW has more than one advantage. Firstly, the AW is a passive device which does not require any kind of external energy source; therefore it is totally implantable and does not require a percutaneous wire, which can be prone to infection

and cause discomfort to the patient. The passive nature of the AW also implies minimal consequences in case of malfunctioning or rupture: if the implanted AW breaks, the positive effects on pulse pressure reduction would be lost but there would be no potential threat to the survival of the patient. Moreover, the AW being an extra-vascular device, it will not require severing of major arteries and will present less risk of thrombosis and hemolysis compared to the intra-aortic counterpulsation balloon.

Finally, the AW will also require a less invasive surgical procedure for implantation compared to VADs and counterpulsation devices. The thoracic aorta is easily accessed and the AW can be most readily applied to the proximal ascending aorta before the origin of the brachiocephalic artery, or to the descending thoracic aorta between the intercostal arteries. The procedure could be initially performed in patients who require other surgery as well (e.g. coronary artery bypass or aortic root replacement in Bentall procedure), and later by minimally invasive thoracoscopy. The ascending aortic site is particularly attractive in humans since it dilates and elongates with age to a greater degree than other arteries (Sugawara et al. 2008; Hickson et al. 2010; Redheuil et al. 2011), and it has no branches between the coronaries and brachiocephalic trunk.

### **2.4.3 Experimental evidence of “stiffening” aortic wraps**

It is well known that a minimal intervention on the stiffness of the AA alone can have a great impact on the whole aortic compliance and therefore on central pulse pressure. On this matter, Ioannou *et al.* (Ioannou et al. 2003) proved that the proximal thoracic aorta accounts for about half of the total arterial compliance, being the AA the most distensible and largest section of the arterial tree.

Several experiments have been carried out on decreasing the aortic compliance by the application of synthetic rigid material on the AA and observing the effects of this procedure on arterial impedance and cardiovascular hemodynamics. A landmark experiment was carried out by O'Rourke in 1967 (O'Rourke 1967), in which portions of the brachiocephalic artery and thoracic aorta of dogs were stiffened with extra-aortic ferrules and pressure and flow waves were measured *in vivo* (**Figure 2.23**); the study demonstrated that lower compliance of the proximal aorta achieved via surgical application of "stiff wraps" determined a marked increase in the ratio of pulsatile to total cardiac work, and therefore a decrease in cardiac efficiency, suggesting a potential detrimental effect on cardiac function.

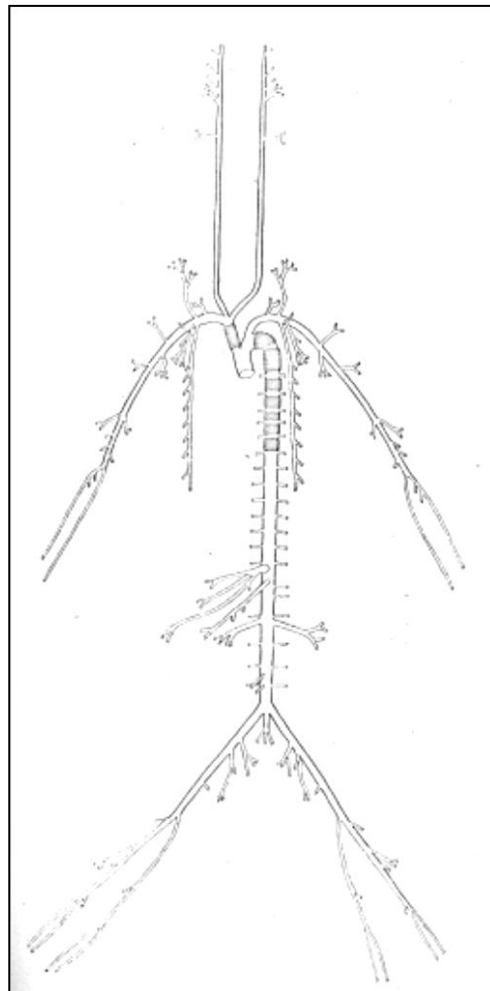


**Figure 2.23:** Diagram of the dog arterial system reproduced from (O'Rourke 1965), showing how arterial distensibility was reduced by applying ferrules to the brachio-cephalic artery and descending thoracic aorta. similar wrapping pattern could be used for destiffening of the aorta.

Some decades later, the study by Kelly *et al.* (Kelly, Tunin, and Kass 1992) proved that a stiff plastic prosthetic aorta decreased the aortic compliance by 60%-80% and caused an increase in myocardial oxygen consumption to maintain adequate flow.

More recently, Ioannou *et al.* (Ioannou et al. 2009) have wrapped rigid Teflon prostheses on the aortic arches of 6 pigs and showed that the procedure reduced aortic compliance by around 50% on the second post-operative day. This led to a late systolic augmentation of the pressure wave, an increase in both systolic and pulse pressure (of 41% and 86% respectively), and to a concomitant increase in aortic characteristic impedance, while peripheral resistance and cardiac output remained unchanged. Moreover, the banding caused concentric hypertrophy of the left ventricles.

As a natural progression of this line of experimental work, it seems then logical to reverse the hypothesis: instead of *stiffening* the proximal aorta with synthetic prostheses and obtain increased impedance and PP, the aim is at *destiffening* the AA via a distensible elastic material, in order to increase AA compliance; this is expected to restore the AA pulsation dampening function, with a subsequent drastic effect on arterial characteristic impedance, pulse wave shape, PP and SP magnitude, and ultimately cardiac function. The Aortic Wrap is then the proposed method to obtain said AA *destiffening*.

#### **2.4.4 Initial study on the Aortic Wrap**

An initial investigation on the AW concept was carried out by Iliopoulos in 2006 (Iliopoulos 2006). He performed an experimental study on sheep: the aged stiff and dilated aorta was simulated by the resection of a segment of the descending aorta and the surgical implant of an oversized Dacron graft; subsequently an elastic wrap was clipped around the prosthesis with a decreased diameter, to simulate the AW procedure, and alterations of stiffness were measured *in vivo* under physiologic pressure and flow conditions (**Figure 2.24**). The application of the

elastic wrap to the Dacron prosthesis achieved a reduction in functional stiffness of the wrapped segment up to a factor of 7.6.

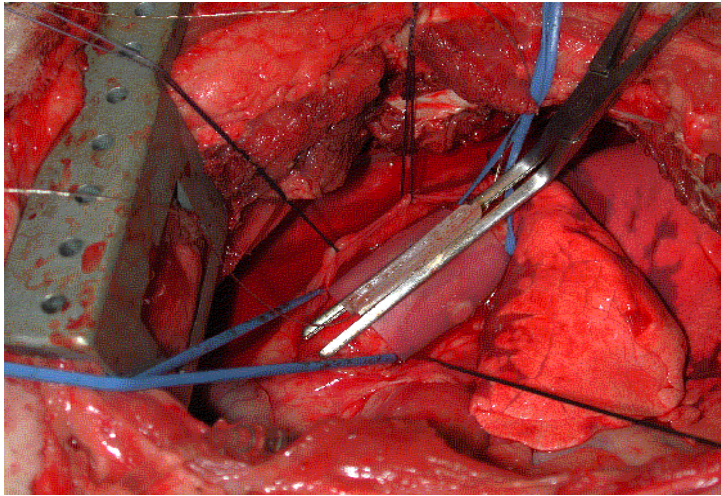


**Figure 2.24:** Picture of an implanted AW in an experimental sheep model. Reproduced from Iliopoulos. (Iliopoulos 2006)

The preliminary results of his study, thus, proposed the Aortic Wrap as a promising therapeutic concept to restore aortic distensibility and decrease pulse pressure in the stiffened, enlarged ascending aorta typical of elderly ISH patients. It became therefore necessary to perform a more accurate investigation on the hemodynamic aspects of the AW procedure, proving the concept from an engineering perspective and exploring its efficacy.

### **2.4.5 Aim of the thesis**

This thesis aims at investigating the efficacy of the AW on restoring higher distensibility and reducing pulse pressure in stiff models of the ascending aorta. To achieve this goal, different biomedical engineering methods will be used.

Firstly, a computational multibranched model of the arterial circulation was used to simulate the effects on AA pulse pressure of the reduction in diameter and the hypothesized increased compliance occurring after wrapping.

Subsequently, experiments on tubular silicon and fabric models of the aorta were conducted to assess the actual efficacy of the elastic wrapping procedure to unload the aortic wall and increase distensibility of the wrapped arterial segment. Then, a multibranched 1:1 scaled silicon model of the human arterial tree was used in connection with a mock circulation to simulate the effects of the AW on pulsatile hemodynamics and assess its efficacy in lowering pulse and systolic pressure in different heart rate and stroke volume configurations.

Finally, a potential problem related to the use of the AW on the AA is the narrowing of the arterial lumen associated with it: although necessary to allow the collapse of the arterial wall inside the surrounding elastic wrap in order to achieve the load-bearing switch, the decreased lumen may have an impact on the hemodynamic patterns, causing abnormal endothelial shear stress and wall tension in the AA. Some of these aspects have been investigated via computational fluid dynamic modelling of the aorta.

# Chapter 3

## *Simulation of reduction of proximal aortic stiffness by an elastic wrap and effects on pulse pressure*

**This Chapter is reproduced from the following refereed conference proceedings:**

Giudici, F, Y Qian, M O'Rourke, and A Avolio. 2012. "Simulation of Reduction of Proximal Aortic Stiffness by an Elastic Wrap and Effects on Pulse Pressure." In *Engineering in Medicine and Biology Society (EMBC), 2012 Annual International Conference of the IEEE*, 2012:657–660.

### **3.1 Background**

Age-related increase in arterial stiffness is determined by changes in the aortic wall properties including stretching and fragmentation of the elastic lamellae within the vessel wall, caused by the repetitive cyclic stresses induced by the heart pulsations on the arterial walls. (Nichols et al. 2011)



In particular, stiffening of the ascending aorta with aging is a major determinant of hypertension and cardiac failure, because of its fundamental role in the arterial “Windkessel” function, converting the pulsatile flow from the heart into a more steady flow in the peripheral vasculature. The ascending aorta, rich in elastin content, buffers the ventricular stroke during systolic expansion, and functions as a reservoir to distribute blood flow during diastolic relaxation. Therefore, a decrease in compliance of this arterial segment, which accounts for about 60% of the total systemic compliance (Ioannou et al. 2003), causes an increase of systemic input impedance ( $Z_{in}$ ) and characteristic impedance ( $Z_c$ ) and increases pulse wave velocity with associated early wave reflection. All these factors contribute in raising aortic pulse pressure (PP), with subsequent onset of hypertension and increase of left ventricular work, which in turn leads to cardiac hypertrophy, higher myocardial metabolic requirements, and potentially heart failure. The increased pulsatile pressure further damages the vascular elastic structure of the arterial wall, leading to further increase in aortic stiffness, in a positive feedback mechanism. (Cavalcante et al. 2011)

Current treatments of heart failure aim to reduce cardiac load, either pharmacologically, by reducing the arterial peripheral resistance, or mechanically, by intra-aortic balloon counterpulsation and ventricular assist devices.

As described in a recent study by Ioannou *et al.*, acute reduction of aortic compliance determines an increase in  $Z_{in}$  and  $Z_c$ , with a subsequent increase in systolic pressure (SP) and PP, leading to cardiac hypertrophy (Ioannou et al. 2009). If, on the contrary, aortic compliance is increased (i.e. stiffness is decreased), inverse results are expected: decreased SP and PP, reduction of  $Z_{in}$  and  $Z_c$ , and reduced ventricular work.

A proposed method to obtain these effects is the aortic wrapping procedure: a wrap made of an elastic material applied around the ascending aortic segment, reducing the aortic diameter to

values similar to those observed in young healthy adults (Redheuil et al. 2010). We hypothesize that, after wrapping, the pulsatile load will be borne by the external elastic wrap rather than the aortic wall, thus reducing the functional stiffness of the vessel. The procedure will therefore lower SP, improving ventricular ejection and decreasing the myocardial oxygen demand, while it will increase diastolic pressure, improving myocardial blood flow. In summary, this procedure is expected to lower PP and the pulsatile external work by the heart, thus increasing the efficiency of the circulation.

In this study, a mathematical model of the arterial circulation has been used to evaluate the effects of the aortic wrap on PP at the aortic root. In an *in vitro* pilot study performed by Iliopoulos on excised aged human aortas connected to a mock hydraulic circuit, wrapping the ascending aorta reduced R to about 80% of the baseline value, the measured functional stiffness (E) of the segment being approximately 20% of the stiffness of the unwrapped native vessel (Iliopoulos 2006). For this reason, special attention has been placed on this specific scenario (80% R and 20% E) when analyzing the data of the simulation.

## 3.2 Methods

A mathematical, multi-segment model of the arterial circulation has been used to investigate the effects of compliance and diameter changes on PP in the ascending aorta. The work of Avolio forms the basis of the model used (Avolio 1980).

The current model consists of 136 segments and 76 nodes, describing the anatomical branching of the arterial tree. Each segment represents one arterial section as a uniform circular thin-walled elastic tube, with internal elastic, viscous, and inertial properties, which are described in terms of the tube physical properties: length, wall thickness, radius (R), Young's modulus (E), Poisson ratio, wall viscoelasticity, blood density, and blood viscosity. The values chosen for all

parameters were typical of elderly subjects, and are derived from the literature and anatomical atlases (Westerhof et al. 1969; Karamanoglu et al. 1994). The model calculates the characteristic impedance of each segment ( $Z_o$ ) from the closed-form solutions of the Navier-Stokes equations for pulsatile flow in elastic tubes (as described by Womersley (Womersley 1957)) and the Moens-Korteweg equation for wave velocity. The viscoelastic properties of the arterial wall are described by the tangent of the angle  $\phi$ , representing the phase lead of pressure in relation to wall displacement. Values of impedance,  $Z_{in}$ , and transmission ratio for each segment are calculated by means of electrical transmission line theory. Pressure can then be determined at any node throughout the arterial tree for a given flow input at the aortic root. Calculations are performed with a constant ventricular ejection wave with maximum velocity of 66 cm/s, systolic ejection period of 490 ms and cardiac cycle length of 830 msec. The ejection wave was typical of an old subject (Nichols et al. 2011).

The effect of variations in elastic properties and geometrical features were then determined. In particular, the wrapping procedure was simulated by incrementally varying  $E$  and  $R$  of the ascending aortic segment, and the subsequent changes in PP and impedance were calculated at the aortic root.

The model and the post-processing of the results were run in Matlab 7.12.0 (The Mathworks Inc., Natick, MA).

### **3.3 Results**

The results presented show the calculated values of PP, SP,  $Z_c$ , and  $Z_{in}$  at the aortic root (first segment of the model), when values of  $R$  and  $E$  are incremented in the central part of the ascending aorta (second segment of the model).

All variable values are normalized, calculated as percent of the respective variable reference values (relative to a control condition in which R and E are unchanged). The reference values are expressed with the termination “100” (PP100, SP100,  $Z_c$ 100,  $Z_{in}$ 100, E100, R100).

E varies from 5% to 195% of E100 in 30 increments of 5%, while R varies from 50% to 150% of R100 in 10 increments of 10%.

A 3D mesh plot of the calculated PP changes vs. the total range of R and E variations is presented (**Figure 3.1**). PP increases when R is reduced, whereas an inverse pattern is observed for the E variations. Moreover, the sensitivity of PP changes, for every R value, is higher for E values  $<20\%E_{100}$ , compared to the symmetric situation of E values  $>180\%E_{100}$ , where instead the PP curves reach a plateau.

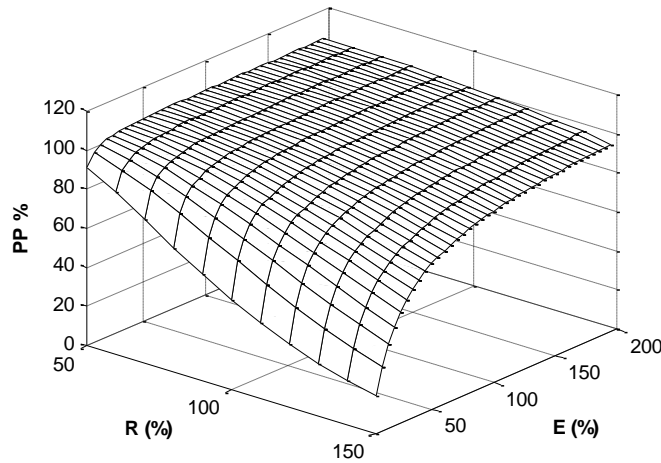


**Figure 3.1:** PP (as % of PP100) calculated by the model for the aortic root vs. variations in R (as % of R100) and E (as % of E100) of the ascending aortic segment.

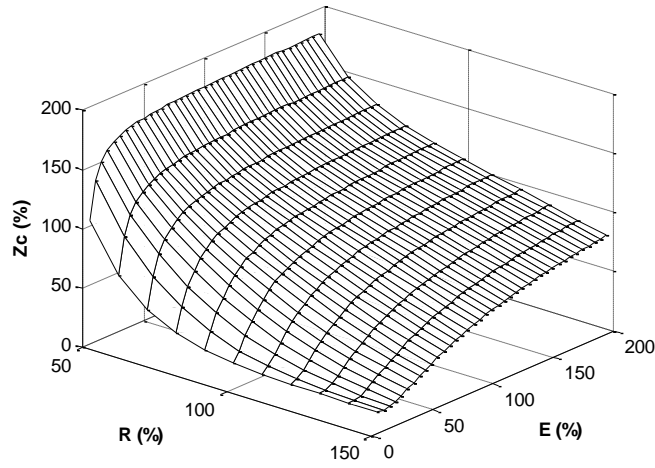


**Figure 3.2:**  $Z_c$  (as % of  $Z_{c100}$ ) calculated by the model for the aortic root vs. variations in  $R$  (as % of  $R_{100}$ ) and  $E$  (as % of  $E_{100}$ ) of the ascending aortic segment.

Changes in  $Z_c$  vs. variations of  $E$  and  $R$  are shown in a 3D mesh plot (**Figure 3.2**). Similarly to the PP trend, an increase in  $Z_c$  is observed for  $R$  reduction and for  $E$  augmentation, but the sensitivity of the curve is higher for smaller  $R$  ( $<70\%$ ) for every  $E$  value.

The  $Z_{in}$  modulus is plotted for the first 20 harmonics (**Figure 3.3**). Two different scenarios are described: the baseline scenario (solid line), in which there is no variation of  $R$  and  $E$ , and the “realistic” wrapped scenario (dotted line), in which values of  $R$  (80%  $R_{100}$ ) and  $E$  (20%  $E_{100}$ ) are chosen, as expected to occur after the wrapping procedure according to the *in vitro* pilot study results. The values of  $Z_{in}$  are normalized to the value of the baseline impedance at the first harmonic. A decrease in  $Z_{in}$  is observed for the wrapped scenario at every harmonic component.

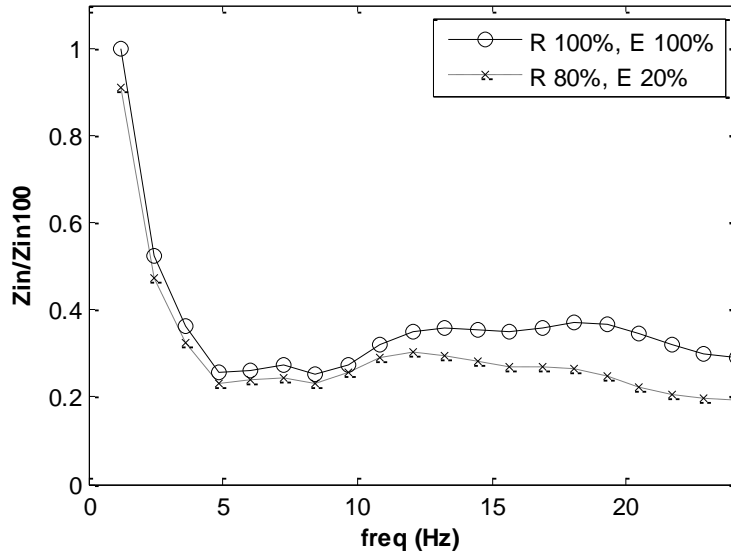


**Figure 3.3:** Modulus of  $Z_{in}$  calculated by the model at the aortic root, when no variations are imposed ( $R = 100\%$   $R_{100}$ ,  $E = 100\%$   $E_{100}$ , solid line) and for variations that simulate what is expected to occur after wrapping ( $R = 80\%$   $R_{100}$ ,  $E = 20\%$   $E_{100}$ , dotted line).

In summary, the changes in PP, SP, and  $Z_c$  are shown in **Table 3.1**, for the R and E variation ranges expected to occur in a real surgical wrapping procedure. As shown by the table, for an R value of 80% $R_{100}$ , an E value of 20% $E_{100}$  is needed to achieve a drop in PP to a value of 91.2% $PP_{100}$ , corresponding to a SP of 89.4%  $SP_{100}$  and a  $Z_c$  of 78.4%  $Z_{c100}$ .

### 3.4 Discussion

The mathematical model described was used in this study to simulate the changes in PP, SP, and  $Z_c$  at the aortic root determined by incremental variations of R and E of the ascending aortic wall. In particular, it was used to predict the effects on pressure and impedance of the proposed aortic wrapping procedure, which can be represented by reduced R and E.

**Table 3.1:** Changes in pressure (PP and SP) and impedance ( $Z_c$ ) values in the ascending aorta, induced by six variations of E and two variations of R. All values calculated as % of the respective reference values (PP100, SP100,  $Z_c$ 100, E100, R100).

E%	PP%		SP%		$Z_c$ %	
	R 100%	R 80%	R 100%	R 80%	R 100%	R 80%
5	45.6	63.5	40.0	58.0	21.8	32.3
10	64.3	79.8	58.8	75.7	30.0	51.7
15	74.2	87.1	69.4	84.3	40.4	67.3
20	80.4	91.2	76.3	89.4	50.0	78.4
25	84.5	93.9	81.2	92.7	58.0	86.4
30	87.6	95.7	84.7	95.1	64.7	92.4

Results show that the effect of PP reduction associated with a decrease in functional stiffness of the wrapped aortic segment is able to override the increase in PP associated with a reduction in radius. That is, the model predicts that if the ascending aorta is wrapped and its radius is reduced by 20% ( $R = 80\%$  R100), a reduction in functional stiffness by 80% ( $E = 20\%$  E100) is required to induce a drop in PP by 8.8% ( $PP = 91.2\%$  PP100).

The model results are in good agreement with values measured during the *in vitro* pilot study (described in section 3.1) in which human aged aortas were connected to a pulsatile flow pump in a mock hydraulic circuit (Iliopoulos 2006); the aortas ( $n=9$ ) were wrapped with two different wraps made of materials with different stiffness (material A, characterized by 4% increase in diameter with each pulsation, and material B, characterized by a 12% increase), and the radius of the wrapped segment was set to three different R values (91%, 82%, and 70% of the baseline values). To allow for a comparison between the *in vitro* and modelled data, four 2D projections of the modelled 3D surface described in fig. 1 are plotted on the PP-E plane for four different values of R variation (70%, 80%, 90%, and 100% of R100), chosen as the closest values to the experimental R values (**Figure 3.4**). On the same graph, six data points are plotted with different geometrical markers, corresponding to six different *in vitro*

experimental set-ups (three different R values and two different wrap materials), whose values are averaged for the 9 samples. As shown by the graph, the two data points relative to R reduction of 30% ( $R = 70\%$ ) fit on the relative calculated curve. The four experimental set-ups relative to R reductions of 18% and 9% instead correspond to values of PP which are slightly underestimated by the mathematical model.

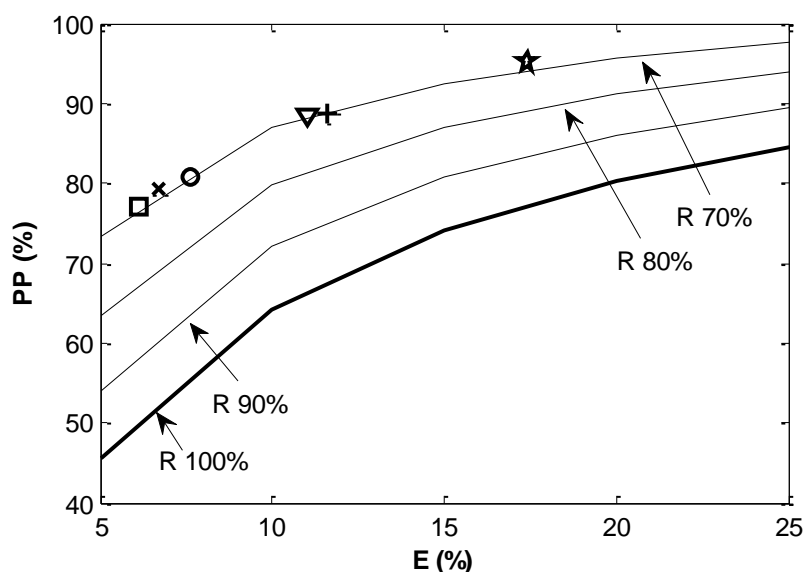


**Figure 3.4:** Solid lines represent PP calculated by the model (as % of PP100) at the aortic root, vs. E variations (as % of E100) of the ascending aortic segment, for four different R variations (100%, 90%, 80%, and 70% of R100). Six data points measured in the *in vitro* pilot study are plotted over the model lines with the following markers: star (material B,  $R = 91\%$  R100), triangle (material A,  $R = 91\%$  R100), plus sign (material B,  $R = 82\%$  R100), circle (material A,  $R = 82\%$  R100), x sign (material B,  $R = 70\%$  R100), square (material A,  $R = 70\%$  R100).

In conclusion, the predicted values of PP reduction and the cardiac unloading suggested by the reduction of  $Z_c$ , for realistic values of R and E reduction achievable by aortic wrapping, could be beneficial in the treatment of hypertension and cardiac failure. The modelling findings, supported by the pilot *in vitro* results, indicate the aortic wrapping procedure as a promising non-pharmacological hypertension treatment, whose efficacy needs to be further investigated.



# Chapter 4

## *In vitro investigation of the effects of the Aortic Wrap on distensibility of a rigid cylindrical model of the aorta*

### **4.1 Introduction**

In previous work (Giudici et al. 2012), as detailed in Chapter 3 of this thesis, a multibranched computational model of the arterial circulation was used to demonstrate that a decrease in diameter of 20% coupled with a decrease in functional stiffness of 80% in the ascending aorta induces a decrease in pulse pressure of 8.8% at the aortic root, which leads to a concomitant reduction in systolic pressure. As a consequence of these promising computational results, it is therefore imperative to prove that the significant decrease in stiffness which produces the desired blood pressure reduction can actually be achieved by means of aortic wrapping.

The Aortic Wrap, as a method to restore high distensibility in old stiffened aortas, is not a straightforward notion: the fact that wrapping and constricting a stiff segment of the aorta with an elastic band results in an increased compliance can be somewhat counterintuitive. What underlies the effectiveness of the Aortic Wrap in increasing distensibility is the concept of *unloading*: by reducing the aortic diameter with the wrap, it is possible to make the aortic wall collapse within the wrap and to shift the pulsatile load from the wall to the elastic wrap; it is then the wrap material that expands and contracts, buffering the heart pulsations, instead of the aortic wall. In the unloaded condition, the aortic wall becomes essentially a passive vessel to contain the blood. This increase in compliance causes a decrease in pulsatile pressure, which in turn induces a decrease in systolic pressure, which is seen as the ultimate target of successful treatment of isolated systolic hypertension (ISH) (Franklin 2012).

It is then necessary to prove this concept *in vitro*, in the most simple and unambiguous way. Hence, the first step of this experimental investigation on the Aortic Wrap efficacy was to quantify its effects on the distensibility of the wrapped aorta. In order to conduct such experiments, models of both the aorta and the Aortic Wrap were created and optimized. Young's modulus, the prime "candidate" for testing the mechanical properties of materials and measured by means of a tensile test, could not be utilised for the purposes of this study: the wrapped aortic segment is a complex system characterised by the interaction between the AW and the collapsed aortic walls, as well as the "unloading" mechanism which constitutes the very core of its efficacy; for this reason, the mechanical properties of the system could not be assessed with a tensile test. A more suitable parameter was then identified: distensibility, which is an ideal measure of compliance changes for wrapped elastic conduits filled with water.

The experimental procedure designed for this study consisted of increasing volume ( $\Delta V$ ) in closed aortic models and measuring the associated increase in pressure ( $\Delta P$ ), in order to characterize the models' elastic properties by means of pressure-volume curves. Compliance ( $C = \frac{\Delta V}{\Delta P}$ ) and distensibility ( $Dist = \frac{1}{V} \frac{\Delta V}{\Delta P}$ ) were then calculated for unwrapped and wrapped model configurations and compared.

## 4.2 Methods

### 4.2.1 Aortic models

To model the aorta in static *in vitro* experiments, two different types of models were used, both of straight cylindrical shape but made of different materials. The difficulties encountered with the first model, which was an *ad hoc* silicon tube with aorta-like distensibility, induced the creation of a second model, made of fabric, which was able to better mimic the behaviour of the wrapped aorta and presented less technical working issues.

**A) *Silicon model:*** The first model used was a 20 cm long silicon tube, with 3 cm internal lumen diameter and 1.5 mm wall thickness. The model was custom made and had distensibility in the physiological range ( $0.002 \text{ mmHg}^{-1}$ ).

**B) *Fabric model:*** The second model was constructed by sewing a length of rigid fabric into a tube. The fabric was porous; therefore a highly distensible rubber cylinder was placed within the tube in order to provide a waterproof lining that would not interfere with the mechanical behaviour of the fabric. The model was 14 cm long and had a 3.5 cm diameter.

Each aortic model was then attached to two custom made *ad hoc* connectors. The “plug” connector completely closed one end of the aorta, while the “inlet” connector attached the other end of the aorta to a 3-way valve to which it was possible to connect a pressure sensor and a syringe at the same time (**Figure 4.1**).

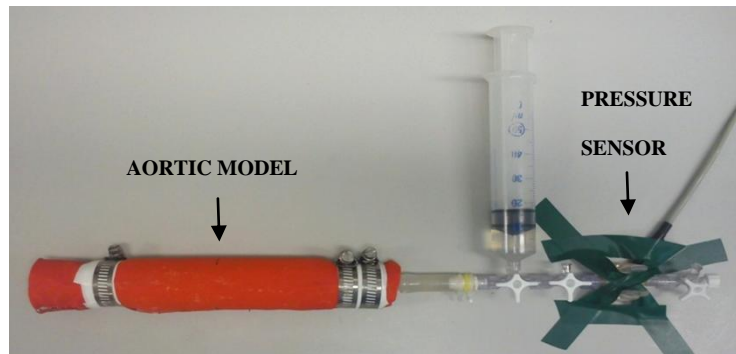


**Figure 4.1:** Typical experimental set up: the silicon aorta is closed at one end by the “plug” connector and is connected to a pressure transducer and a syringe via the “inlet” connector and 3-way valve.

The “plug” connector consisted of a round stiff cylinder wrapped with several layers of Tygon tubing in order to fit the size of the aortic model (**Figure 4.2**). The Tygon layers and the rigid cylinder were glued together so that all the microscopic holes were filled and the irregularities in shape were smoothed. The connector was further wrapped with a layer of special silicon tape, in order to minimize the roughness when in contact with the inner surface of the aortic model.



**Figure 4.2:** “Plug” connector composed of a rigid cylindrical core and several external layers of Tygon sealed with silicon glue and hot glue.

The “inlet” connector was built similarly to the “plug” connector (**Figure 4.3**). Several layers of Tygon were wrapped and glued around a commercially available barbed reducing fitting,

which decreased the lumen diameter from 1.3 cm to 0.8 cm; the whole connector thus reduced the lumen diameter from 3 cm to 0.8 cm. On the other end of the barbed connector, a further reduction with smaller tubing and barbed fitting was necessary to be able to attach a luer 3-way valve. This connector was lined with special plumbing silicon tape as well.

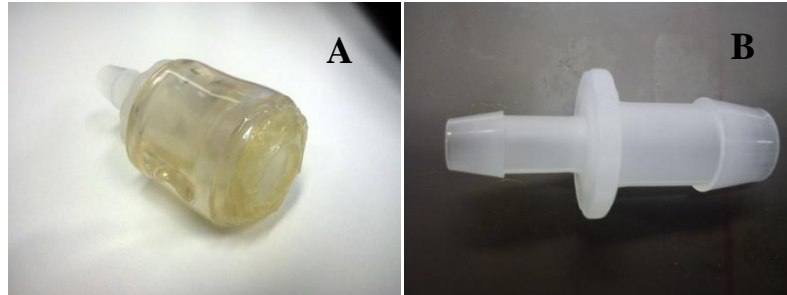


**Figure 4.3:** A) “Inlet” connector, composed by Tygon layers around a barbed connector. B) Barbed reducing connector used as core for the “inlet” connector.

The aorta was secured on the two connectors with commercially available plumbing metal rings, to avoid any leakage, and subsequently filled with water at atmospheric pressure.

#### 4.2.2 Elastic wraps

To create a model for the aortic wrap, different types of elastomeric material with different shapes were used. At this initial stage of investigation, where the main aim was to prove the aortic wrap efficacy, the focus was not on aspects of the material such as biocompatibility or resistance to fatigue, but merely on its elastic properties; in this *in vitro* investigation the only requirement considered in the choice of the wrap material was its higher distensibility compared to the aortic model.

After several trials, the two main typologies of wrap chosen were the following:

- A) **Rectangular:** A wrap of rectangular shape was cut out of a flat portion of an easily distensible elastic material, which could be a big inflatable balloon or of a

physiotherapy elastic band. Various lengths and widths could be achieved, depending on the available material. With a permanent marker, two parallel lines were drawn across the width of the wrap, so that the distance between them corresponded to a specific value of interest. For example, the distance could be equal to the length of a circumference with a diameter which was 80% (or 70%) of the aortic lumen diameter. When the wrap was placed around the aorta, metal haemostats or clips were placed over the drawn lines and clamped firmly; in this way, the wrap had then the diameter of interest and forced the wrapped portion of the aorta to collapse and assume a “folded” shape inside the wrap.

**B) Tubular:** A straight tubular inflatable balloon was cut into 7 cylindrical segments of 1 cm diameter and 3.5 cm length. The segments were slipped on the aortic model from the closed end, one at a time, and they were placed adjacent to one another. As described for the previous wrap typology, the aorta had to be folded and collapsed to accommodate the smaller diameter of the wraps.

For both wrap typologies, lubrication was used between the wrap and the silicon aortic model to minimize friction, which could interfere with the distending behaviour of the wrap during the execution of the experiments. For the fabric aortic model, instead, no lubrication was required.

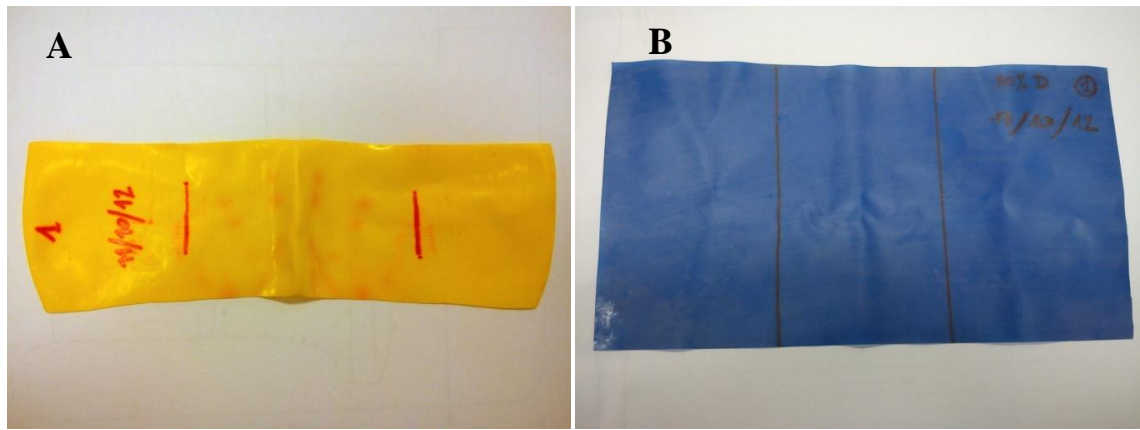


**Figure 4.4:** A) Wrap obtained from a rubber inflatable balloon. B) Wrap obtained from a physiotherapy elastic band.

### 4.2.3 Execution of the experiments

The aortic model, after being filled with water, was connected to a physiological pressure transducer (SP 844, Memcap AS, Skoppum, Norway) via a 3-way valve. The line was flushed with water to eject any potential residual air bubbles in the pressure sensor.

The pressure transducer was connected to a computer via a Quad Bridge Amp (AD Instruments, Bella Vista, Australia) and a PowerLab console (AD Instruments, Bella Vista, Australia), which amplified and digitalized the pressure signal. The signal was then visualized and manipulated on the computer with the software LabChart (AD Instruments, Bella Vista, Australia), and recorded for the whole length of the experiments. Before starting the experiments, the sensor was calibrated with a sphygmomanometer (Tycos, Welch Allyn Inc., Skaneateles Falls, NY, USA).



**Figure 4.5:** A) Pressure transducer. B) Quad Bridge Amp and PowerLab acquisition system. C) Sphygmomanometer.

At the beginning of the experiments the 3-way valve was opened and the aortic model was allowed to collapse until an internal pressure of 0 mmHg was achieved; the valve was then closed and the volume reached was considered the initial volume  $V_o$  for the purposes of these experiments.  $V_o$  varied at every experiment: depending on the aortic model used and the wrapping configuration, zero pressure was reached at a different volume every time; for this reason, in the analysis phase volumes were always normalized to  $V_o$ .

A 60 ml syringe full of water was then connected to the 3-way valve. Incremental volumes ( $\Delta V$ ) of 5 ml of water were injected into the aorta every 5 seconds approximately, until a pressure of about 200 mmHg was reached. If the syringe was emptied before reaching the goal pressure, it was disconnected, refilled with water, and reconnected to the system and injection was continued. The experiment was repeated multiple times to assess reproducibility.

Subsequently, one or more wraps were positioned on the collapsed aortic model and clipped around it; the wrapped experiments were conducted in the same way described for the unwrapped configuration: the valve was kept open in order to allow water to overflow until an internal pressure of 0 mmHg was obtained, corresponding to “unstretched” and “unloaded” AW and arterial walls, according to Laplace’s Law. Again, reproducibility was determined by repeating the experiment multiple times.



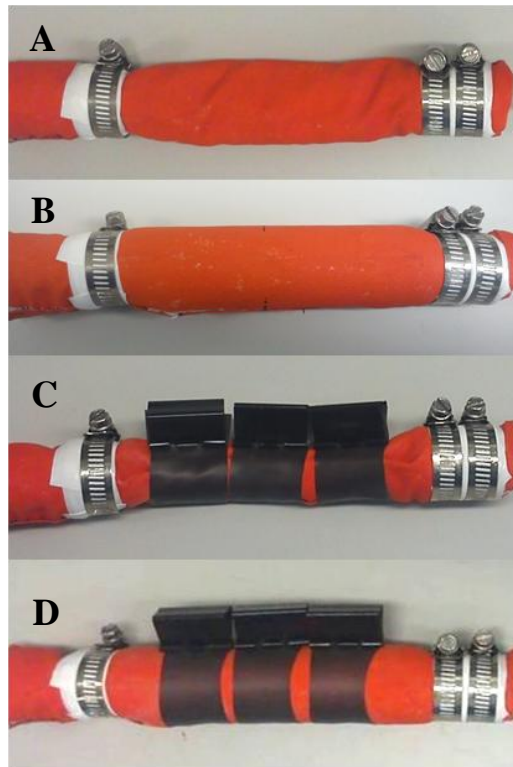


**Figure 4.6:** A) fabric aortic model at 0 mmHg (beginning of the experiment); B) fabric aortic model at 200 mmHg (end point of the experiment); C) wrapped fabric aortic model at 0 mmHg (beginning of the experiment); D) wrapped fabric aortic model at 200 mmHg (end point of the experiment).



**Figure 4.7:** Beginning of experiment with a single rectangular wrap derived from a physiotherapy elastic band. A) Wrapped silicon aortic model at zero pressure; B) detail of the wrap.

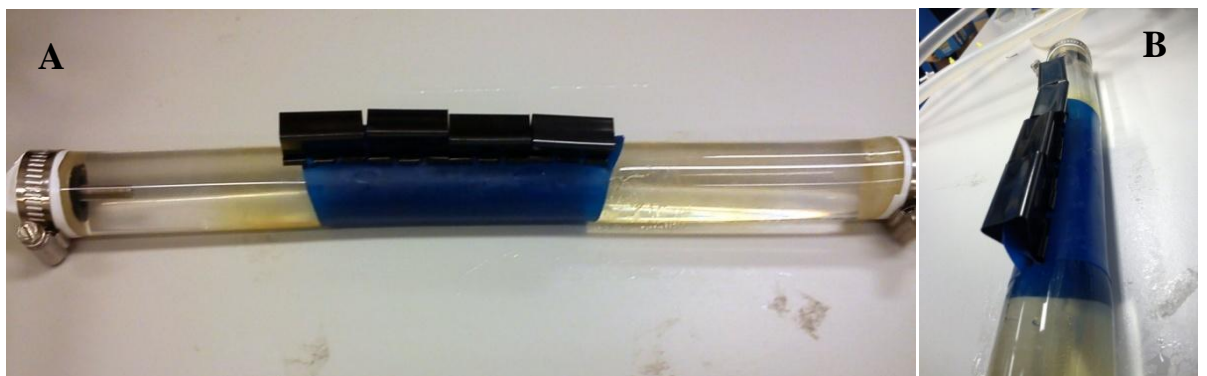


**Figure 4.8:** End of experiment with a single wrap derived from a physiotherapy elastic band. A) Wrapped silicon aortic model under pressure; B) detail of the wrap.

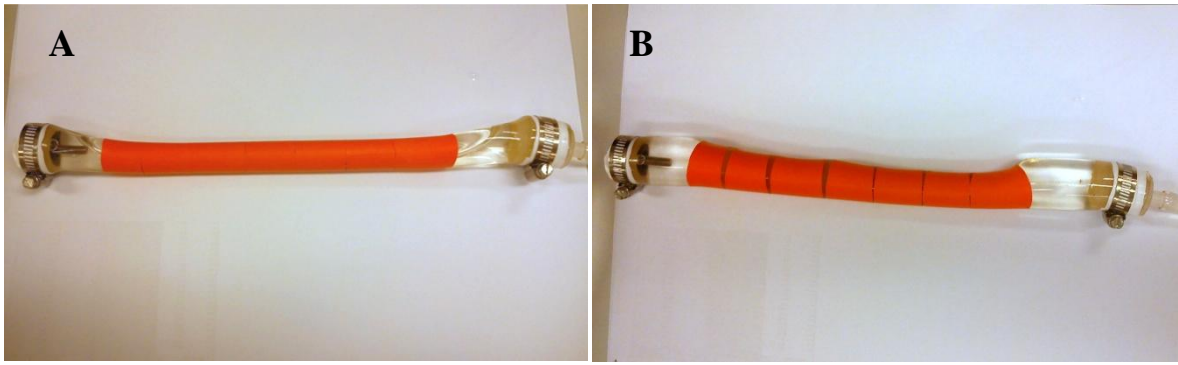


**Figure 4.9:** Experiment with multiple cylindrical wraps derived from rubber balloons. A) Beginning of the experiment – wrapped aortic model at zero pressure. B) End of the experiment – model under pressure.

#### 4.2.4 Data analysis

The pressure ramp obtained was then visualized on LabChart, and the data points of interest were chosen to be the initial points of each step increase in pressure, which corresponded to each imposed step increase in volume. At the end of each experiment, the interest points were manually selected on the GUI and exported to Microsoft Excel and subsequently to Matlab for further analysis.

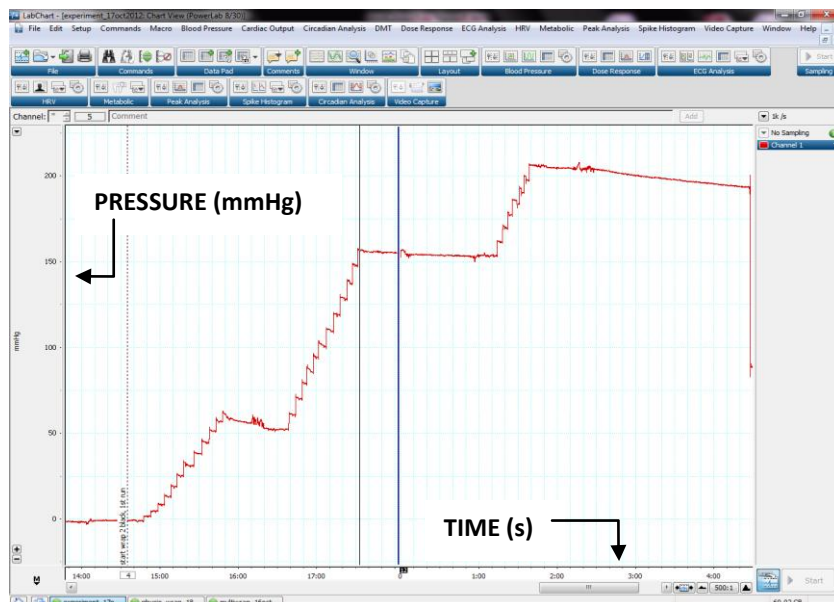


**Figure 4.10:** Typical “ramp” of pressure values recorded during an experiment and displayed on the computer monitor via LabChart. Each pressure increment occurs after every volume injection via the syringe. The longer plateaux correspond to the pauses in which the syringe had to be disconnected to be refilled with water. In this particular experiment, a value of about 200 mmHg was reached after 31 volume steps (i.e. after injecting 155 ml).

The pressure points of interest  $P$  were then plotted against the absolute volume  $V$  ( $V = V_0 + \Delta V$ ), to obtain pressure-volume curves. From values of  $P$  and  $V$  it was then possible to calculate compliance ( $C$ ) and distensibility ( $Dist$ ), as per the following equation:

$$Dist = \frac{1}{V} \times C = \frac{1}{V} \times \frac{\Delta V}{\Delta P} \quad (11)$$

Furthermore, the concept of *critical pressure*  $P_c$  was introduced: it is defined as the value of  $P$  at which the wrapped distensibility curve intersects the unwrapped curve; this was chosen as an indicator of the pressure at which the wrap stops having an effect on distensibility, i.e. when the arterial wall is completely distended inside the wrap and is thus fully loaded.

## 4.3 Results

### 4.3.1 Reproducibility

In order to assess the reproducibility of pressure measurements, the experiment was performed multiple times for both an unwrapped and a wrapped model configuration. The aortic silicon model was used for this purpose; the wrap was obtained from a rubber balloon and was 5 cm wide. For the wrapped configuration, an 80% diameter reduction was chosen. Five P-V curves were obtained for each configuration, and average, standard deviation, and coefficient of variation of pressure values were calculated for each step of volume increase (**Figure 4.11**): the direct monitoring of the coefficient of variation at each iteration directed the choice of the number of repetitions sufficient to obtain the desired level of reproducibility (chosen to be corresponding to a coefficient of variation <15% at all volume steps for every wrapping configuration).

The experiment demonstrated high levels of reproducibility for both configurations: after only 5 repetitions, for the unwrapped experiment the coefficient of variation varied from a maximum of 31.9% for the first  $\Delta V$  step to a minimum of 0.41% for the last step and was on average 4.29%; similarly, for the wrapped configuration the coefficient of variation decreased with increasing pressure and was on average 13.77%.

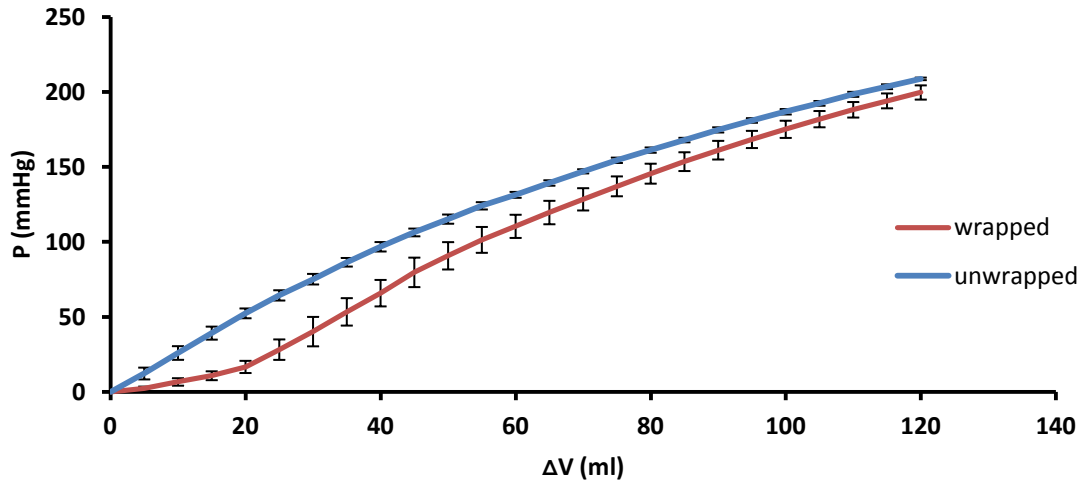


**Figure 4.11:** Reproducibility experiment: average P-V curve for the unwrapped (blue line) and wrapped (red line) configurations; standard deviation is represented by vertical error bars.

### 4.3.2 Experiment A

In order to mimic elastic aortic wrapping, a straight cylindrical rubber tube was cut into 7 rings which were placed adjacent to one another around the silicon aortic model, as described in the *methods* section of this chapter, for a total wrapping length of 17.5 cm; a 33% diameter reduction was achieved. The distensibility of the unwrapped and wrapped model were calculated from measured values of pressure and volume; similarly, the distensibility of the wrap material was calculated by performing the same experiment on the initial cylindrical rubber tube, before cutting it into rings.

A typical wrap-associated distensibility pattern was observed (**Figure 4.12**): the wrapped configuration had an initial Dist approximately 4 times higher than the unwrapped one, but

dropped after  $P_c$  was reached (around 50 mmHg). In particular, Dist of the wrapped segment “followed” Dist of the wrap material (around  $0.01 \text{ mmHg}^{-1}$ ) until  $P_c$ ; then, after a spike due to the tension released by the brisk change in aortic lumen shape, Dist dropped and stabilized on lower values, comparable to those of the unwrapped silicon model (around  $0.002 \text{ mmHg}^{-1}$ ). This Dist behaviour clearly demonstrated the *unloading* concept which underlies the effective function of the AW in restoring higher distensibility in stiff vessels.

$P_c$  was lower than typical hypertensive systolic pressures (150 – 200 mmHg), thus determining the inefficacy of this specific wrap in increasing distensibility of this specific aortic model for the pressure range of interest.

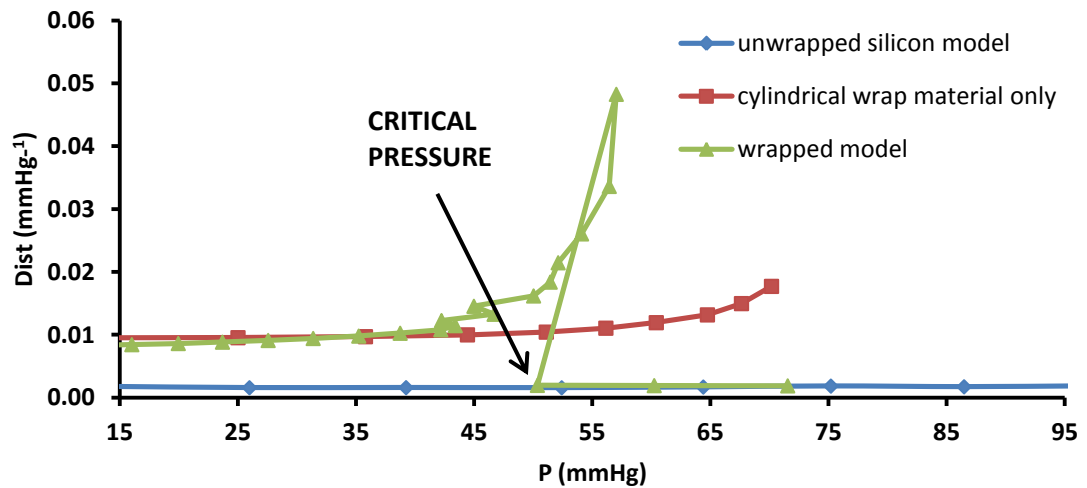


**Figure 4.12:** Experiment A: Dist ( $\text{mmHg}^{-1}$ ) plotted against pressure (mmHg), calculated for the unwrapped (blue line) and tubular wrapped (green line) configurations and for the wrap material (red line) in its tubular initial shape (before the wraps were created). Dist of the wrapped model “follows” Dist of the wrap material for pressures below  $P_c$  (here approximately 50 mmHg), indicating that the wrap material is determining the global behaviour of the whole wrapped segment. When  $P_c$  is reached, the silicon model “unfolds” from its collapsed lumen shape to its round “loaded” shape: this brisk change creates a tension release that causes the spike in Dist observable in the picture. After the shape change occurs, for pressures above  $P_c$  the silicon model is completely distended inside the wrap, and is therefore bearing the pulsatile load; as a consequence, Dist of the wrapped segment drops to values comparable to those of the unwrapped model configuration.

### 4.3.3 Experiment B

Rectangular wraps were used in order to achieve higher critical pressures and investigate the effects of variation of wrapping diameter and length on distensibility. The experiment was

repeated for every combination of 2 different wrapping diameters (70% and 80%) and 3 different wrapping lengths, achieved by using one, two, or three identical rectangular wraps placed adjacent on the model.

Pressure was plotted for normalized values of volume (**Figure 4.13**): P-V curves of wrapped configurations are characterized by a less steep initial slope and then “follow” the unwrapped curve after reaching  $P_c$ ; in the case of the triple wrap configurations, the P-V curve present an increased steepness compared to the unwrapped one.

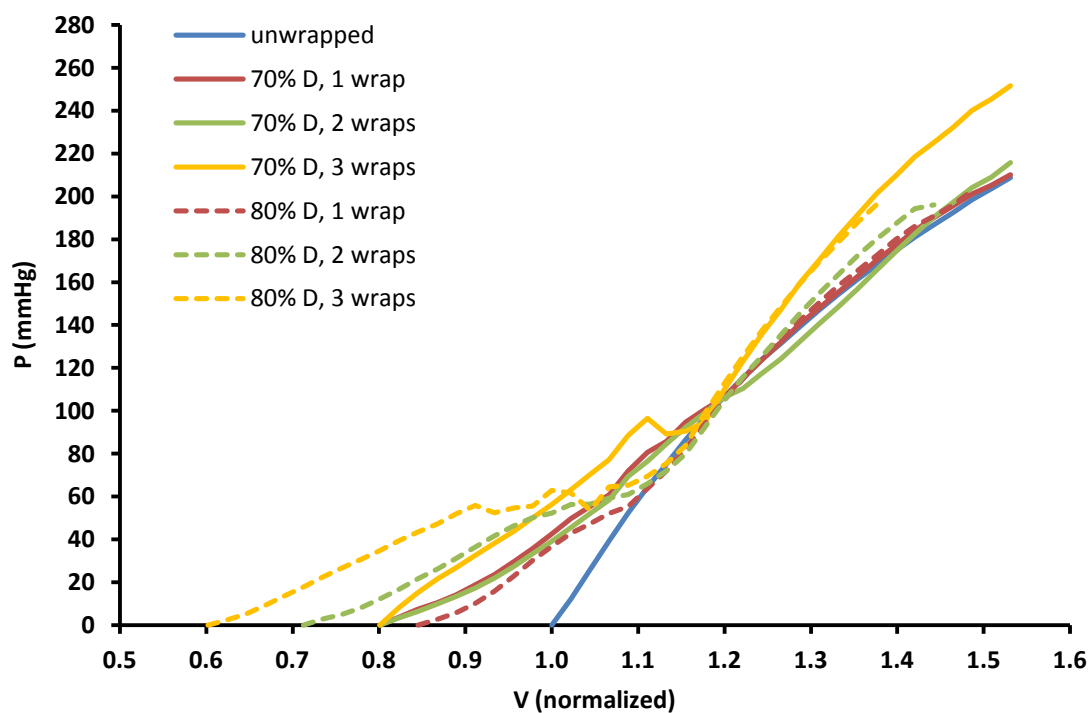


**Figure 4.13:** Experiment B: normalized P-V curves obtained for the unwrapped configuration (blue line), and wrapped configurations characterized by a combination of 2 different diameters - 70% (solid lines) or 80% (broken lines) of the unwrapped diameter - and 3 different wrapping lengths – 1 wrap (red lines), 2 wraps (green lines), or 3 wraps (yellow lines).

Dist-P curves of every configuration are shown in **Figure 4.14**, and mean distensibility values for the first 50 mmHg (corresponding to the “folded” state of the aortic model inside the wrap) were calculated and are presented in

**Table 4.2.** Dist was higher for all wrapped configurations compared to the unwrapped one; in particular, the 80% D configurations achieved higher Dist values compared to the respective 70% D ones.

Finally,  $P_c$  was identified for every configuration, as shown in **Table 4.1**: it was on average higher for the 70% D configurations (114.04 mmHg) compared to the 80% D ones (71.08 mmHg), but still below the ISH systolic pressure range.

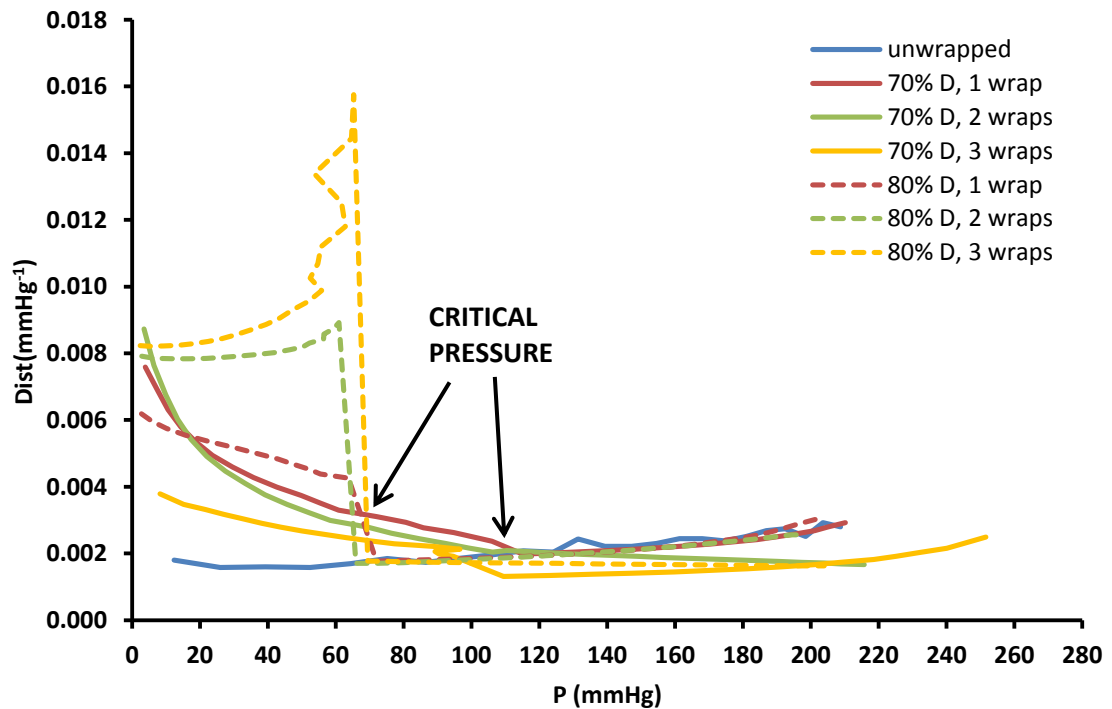


**Figure 4.14:** Experiment B: Distensibility curves obtained for the unwrapped configuration (blue line), and wrapped configurations characterized by a combination of 2 different diameters - 70% (solid lines) or 80% (broken lines) of the unwrapped diameter - and 3 different wrapping lengths – 1 wrap (red lines), 2 wraps (green lines), or 3 wraps (yellow lines).

**Table 4.1:** Experiment B: Critical pressure (mmHg) calculated for the 6 different wrapping configurations (1, 2, or 3 wraps, and diameters 70% or 80% of the unwrapped diameter).

# wraps	70% D	80% D
1	115.09	71.93
2	117.58	65.95
3	109.46	75.37

<b>Average</b>	<b>114,04</b>	<b>71,08</b>
<b>Standard deviation</b>	4,16	4,77
<b>Coeff. of variability (%)</b>	4	7

**Table 4.2:** Experiment B: Average distensibility ( $\text{mmHg}^{-1}$ ) for the 0-50 mmHg pressure range (“folded state” of the aortic model inside the wraps), calculated for the 6 different wrapping configurations (1, 2, or 3 wraps, and diameters 70% or 80% of the unwrapped diameter).

# wraps	70% D	80% D
<b>1</b>	0.0053	0.0054
<b>2</b>	0.0055	0.0079
<b>3</b>	0.0032	0.0095
<b>Average</b>	<b>0.0047</b>	<b>0.0076</b>
<b>Standard deviation</b>	0.0013	0.0021
<b>Coeff. of variability (%)</b>	27	28

#### 4.3.4 Experiment C

A custom made tubular fabric model of the ascending aorta was used, as detailed in the *methods* section of this chapter: the higher stiffness of this model determined a better simulation of the mechanical behaviour of old aortas. The model was wrapped with 3 adjacent wraps, each 3.2 cm long, and the wrapping diameter was 80% of the unwrapped one.

Normalized average P-V curves were obtained for both unwrapped and wrapped configurations (**Figure 4.15**): the slope of the curve was flatter for the wrapped experiments up to a  $P_c$  of 200 mmHg. Distensibility was calculated and plotted in **Figure 4.16**: in the pressure range of interest (50 - 200 mmHg) the wrapped model shows a consistently higher distensibility compared to the unwrapped model; moreover, the average distensibility was calculated in that pressure range and it was 0.0038 and 0.0008  $\text{mmHg}^{-1}$  for the wrapped and unwrapped configurations respectively, showing an almost 5-fold increase after wrapping.



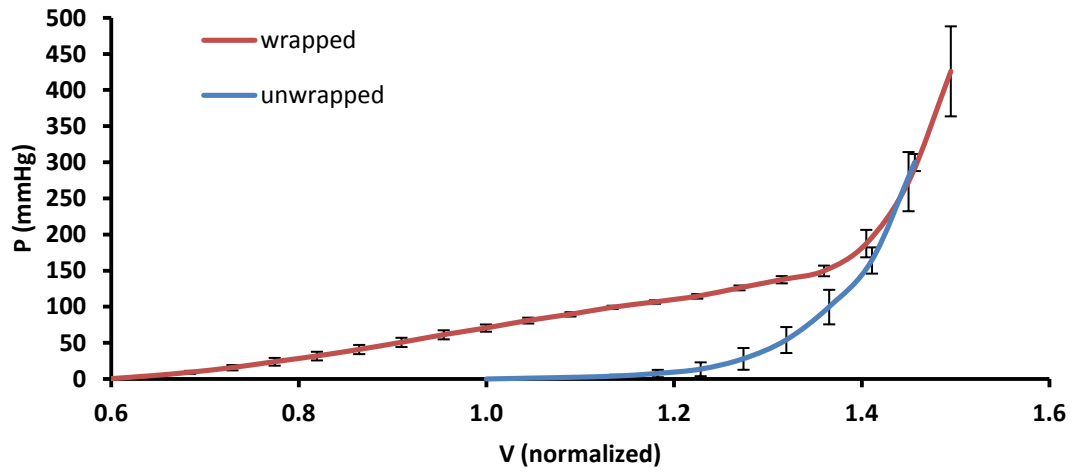


**Figure 4.15:** Experiment C, on fabric aortic model: Average normalized P-V curve measured for the wrapped (blue line) and unwrapped (red line) experiments. Standard deviation is represented by vertical error bars.

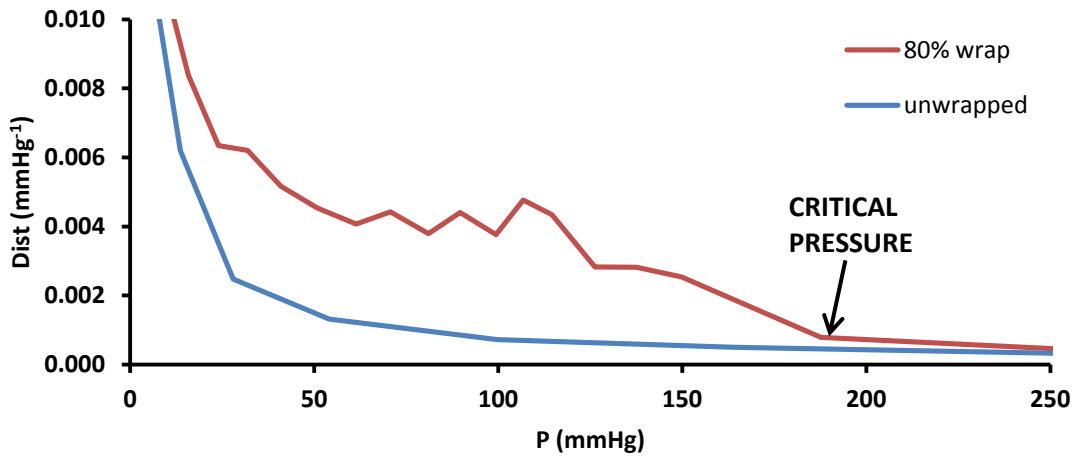


**Figure 4.16:** Experiment C, on fabric aortic model: Distensibility measured for the wrapped (blue line) and unwrapped (red line) experiments.

## 4.4 Discussion

### 4.4.1 Limitations of the wrap models

The development of both a suitable wrap model and a realistic aortic model underwent an optimization process, after a series of pilot experiments.

The first prototypes of aortic wrap models were fashioned with commercially available inflatable balloons and used to wrap the ad hoc silicon aortic model. The material of the balloons was clearly too distensible for the purposes of this study: wraps made of this material distended too easily at pressures that were much lower than the physiological pressures of interest; therefore, the wrapped silicon aorta regained its round distended shape too early in the experiments. More specifically, the  $P_c$  values for these initial experiments were below 50 mmHg: this meant that the aorta was totally distended and bore the pressure load instead of the wrap for values of pressure higher than 50 mmHg. This behaviour can be explained in terms of P-V curve steepness: at  $P_c$  values, the P-V curves had an inflection point, indicating a shift in elastic behaviour from higher compliance at values  $< P_c$  (when the wrap was the load-bearing component of the system) to lower compliance for values  $> P_c$  (when the aorta is fully distended and is thus bearing all the pulsatile load).

The physiotherapy elastic bands, on the contrary, seem to be a more suitable source of material for the wraps, showing  $P_c$  values around 100 mmHg when applied to the silicon aortic model, and very promising  $P_c$  values around 200 mmHg when used on the fabric aortic model. This suggests that a material with comparable elastic properties should be chosen for potential future applications in animal models and clinical trials; in addition, it is advisable that the future wrap material of choice satisfies stringent requirements of biocompatibility, low thrombogenicity, and resistance to cyclic stresses and fatigue; for these reasons, potential candidates are highly elastic and distensible synthetic materials already utilised as endoprostheses, such as silicon, used in a variety of implantable devices, and polyurethane, employed for medium-to-low calibre vascular grafts.

#### 4.4.2 Silicon aortic model

The custom-made silicon aortic model showed a sub-optimal elastic behaviour when wrapped with any of the chosen aortic wrap models. After wrapping, when the model collapsed inside the wrap, one big fold was created: this gave the lumen a characteristic “C” shape (**Figure 4.17**). During water injection, the “C” shaped lumen gradually expanded and the fold became smaller; finally, when the critical pressure was reached, the circular shape was restored with a brisk change of shape. The abrupt shape change created spikes in the recorded pressure values and consequently in the calculated distensibility values. This behaviour did not accurately mimic reality: the real aorta is expected to collapse inside the wrap by simply reducing its internal lumen, as a decrease in wall tension caused by the external application of the wrap will determine a reduction of lumen radius, according to Laplace’s law.



**Figure 4.17:** Detail of the folded shape that the silicon aortic model assumed after wrapping.

Finally, when compared to literature (Redheuil et al. 2010), the distensibility of the silicon aortic model was considerably higher than the one typical of old stiffened aortas (**Table 4.3**). The silicon model distensibility was in the range  $0.0018 - 0.0028 \text{ mmHg}^{-1}$ , typical of 50 - 70 yrs old subjects, whereas the ideal pursued distensibility had to be below  $0.0016 \text{ mmHg}^{-1}$ , corresponding to >70 yrs old subjects, in order to better mimic ISH patients.

Notwithstanding the various limitations of this aortic model, it still proved to be extremely useful in the initial phase of this experimental study. It enabled the optimization of the experimental procedure, identifying its weaknesses, thus leading to the development of an improved aortic model. In particular, experiment A, performed with multiple cylindrical wraps (**Figure 4.12**), proved in a straightforward way that the wrap-induced aortic wall unloading can effectively restore higher values of distensibility; it showed that, if the wrap had a smaller diameter and higher compliance than the aortic model, the distensibility of the whole wrapped segment “followed” the distensibility of the elastic wrap alone, indicating that the wrap material was bearing the load and was therefore determining the global distensibility of the wrapped segment; with increasing pressure, when the aortic model was fully distended and the lumen had regained a round shape, i.e. when critical pressure was reached, distensibility of the wrapped segment dropped to values typical of the unwrapped silicon model, indicating that the latter was then taking on the load, determining an increased global distensibility and effectively cancelling the effects of the wrap.

#### **4.4.3 Fabric aortic model**

Given the limitations of the silicon aortic model highlighted by the experiments A and B, a new model was created, which could better mimic the aortic behaviour during elastic wrapping and could generate more realistic P-V curves. The second aortic model was made of rigid fabric material assembled in a tubular shape. The collapsed wrapped shape of this model was characterized by various small folds, evenly distributed along the circumference; these smaller folds had little effects on the P-V relationship, since they allowed a less brisk unfolding phase with a smoother transition between wrapped and unwrapped lumen geometry.

When compared to values of ascending aortic distensibility found in literature (Redheuil et al. 2010), the average distensibility calculated for the new unwrapped model for pressures between 50 and 200 mmHg was  $0.0008 \text{ mmHg}^{-1}$  and thus fell into the distensibility range of >70 year-old subjects, satisfying the need for an accurate model of the old stiffened ascending aorta (**Table 4.3**).

**Table 4.3:** Typical values of ascending aortic distensibility measured in human subjects, averaged for six age groups, derived for literature (Redheuil et al. 2010).

Age (years)	Distensibility ( $\text{mmHg}^{-1}$ )
20 - 29	0.010
30 - 39	0.008
40 - 49	0.004
50 - 59	0.002
60 - 69	0.0016
>70	0.001

More importantly, after wrapping the fabric aortic model with elastic wraps and decreasing the lumen diameter of 20%, a considerable rise in average distensibility was observed: distensibility changed from  $0.0008$  to  $0.0038 \text{ mmHg}^{-1}$ , thus increasing more than 4.5 times. Again, when comparing these values to ascending aortic distensibility values found in literature (Redheuil et al. 2010), the Aortic Wrap is able to restore the distensibility of a > 70 year old subject to that typical of 40-49 year-old subjects.

## 4.5 Conclusions

In conclusion, this *in vitro* study, and in particular experiment C on the fabric aortic model, proved in an unambiguous way that aortic wrapping can effectively decrease the vascular age of a rigid aortic model by 20-30 years, supporting the proposal of the Aortic Wrap as an effective method to reduce stiffness of old ascending aortas. Results of such magnitude, if

achieved in ISH patients, would have invaluable benefits in terms of dampening of pulse pressure and reduction of systolic pressure.

The successful results achieved by this investigation of the elastic behaviour of wrapped aortic models lead the way to a pulsatile investigation. After proving that the Aortic Wrap can restore higher aortic distensibility via unloading of the aortic wall, it is necessary to examine the direct effects of the unloading mechanism on pulsatile pressure and consequently systolic pressure.

# Chapter 5

## *In vitro investigation of the effects of the Aortic Wrap on pressure and impedance in a silicon model of the arterial circulation*

### **5.1 Introduction**

The Aortic Wrap (AW) is the proposed device-based method to lower blood pressure in elderly patients affected by isolated systolic hypertension (ISH). It is hypothesized that lower central pulse pressure (PP), as well as lower central systolic pressure (SP), can be achieved in an old stiffened ascending aorta (AA) by wrapping it with a more distensible material and reducing its diameter; the diameter reduction is the mechanism responsible for unloading the stiff AA wall, thus placing the pulsatile load on the distensible elastic wrap. The restored higher distensibility of the AA wrapped segment, represented by decreased arterial input impedance ( $Z_{in}$ ), can consequently lower the cardiac afterload, PP, and ultimately SP.

Our previous computational modelling study (Giudici et al. 2012) on the AW effects on aortic pressure demonstrated that pulse pressure can be effectively reduced by 8.8% if the AW achieves a 80% decrease in stiffness of the wrapped AA segment with a 20% diameter reduction. This theoretical model prediction needs to be supported by an *in vitro* demonstration of the AW efficacy in lowering pressure.

In Chapter 4 of this thesis, the effects of the AW on the measured distensibility of a rigid model of the aorta were investigated *in vitro*, providing proof and demonstration of the practical efficacy of the wrap in increasing distensibility of the wrapped model.

It seemed thus necessary to move to a pulsatile experimental setting, in order to analyze the effects of the AW on hemodynamics. Investigations were conducted in a distributed silicon model of the arterial system connected to a pulsatile pump that mimicked physiological conditions; flow waves were measured at the inlet and pressure waves at 10 different locations along the model, comparing the results obtained before and after elastic wrapping of the ascending aorta of the model. Characteristic and input impedance were computed and compared, to investigate the effects of the AW on cardiac afterload.

## **5.2 Methods**

### **5.2.1 Arterial tree model**

For this *in vitro* hemodynamic study a distributed silicon model of the arterial circulation was used (**Figure 5.1**); this model and its prototypes have been constructed, validated and extensively used by other research groups (Segers et al. 1998; Segers and Verdonck 2000; Matthys et al. 2007; Alastruey et al. 2011). The model is a 1:1 scale replica of the simplified



arterial network of an adult human subject. It is composed of 37 tapered arterial segments, of which 16 are terminal arteries (reaching approximately 2 cm lumen). Both geometry and elastic properties mimic the human arterial system; in particular, the AA has a 2.8 cm diameter and moderately high stiffness (arch PWV around 5.4 m/s), comparable to subjects in their 5<sup>th</sup> decade of life. (Matthys et al. 2007)

### 5.2.2 Wrap models

Similarly to what has been done in the static distensibility experimental study detailed in Chapter 4 of this manuscript, the AW was simulated by a rectangular piece of synthetic distensible material, 3.5 cm in length, obtained from commercially available physiotherapy stretching bands.

To allow for diameter reduction, two lines were marked on the surface of the wrap at a distance equal to the circumference corresponding to 70% of the AA diameter, as a guideline to position metal clamps. Once the wrap was secured around the AA with the clamps, a lumen of 1.96 cm diameter (corresponding to 70% AA diameter) could thus be achieved (**Figure 5.3**).

A second wrap, made of the same material as that of the AA and 10 cm long, was created to wrap the thoracic descending aorta of the model (**Figure 5.4**). This wrap will be called the *TA wrap* for the purposes of this study, whereas the first one will be referred to as the *AA wrap*. The diameter reduction and clamping were performed as detailed for the AA wrap.



**Figure 5.1:** Picture of the whole silicon distributed model of the arterial circulation, connected to the pumping system (top). The flow probe is placed around the ascending aorta and the Millar catheter is inserted via a dedicated inlet at the left common iliac artery.

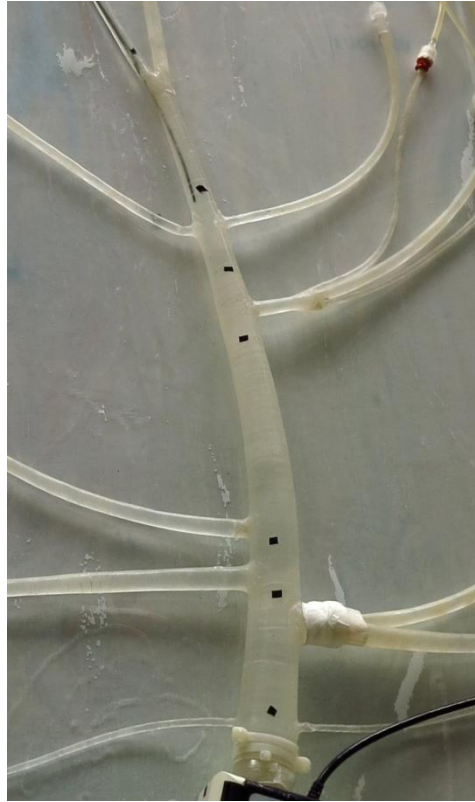


**Figure 5.2:** Detail of the model aorta (inlet at the bottom of the picture, iliac bifurcation at the top); the black spots are the measurement locations at which the Millar catheter tip was placed.

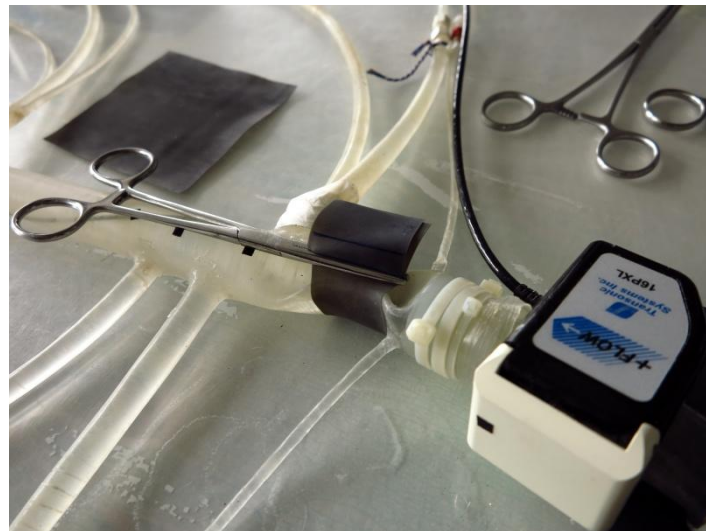


**Figure 5.3:** Detail of the single AA wrap clamped around the aorta inducing a diameter reduction, placed at location 2 distal to the coronary branches.

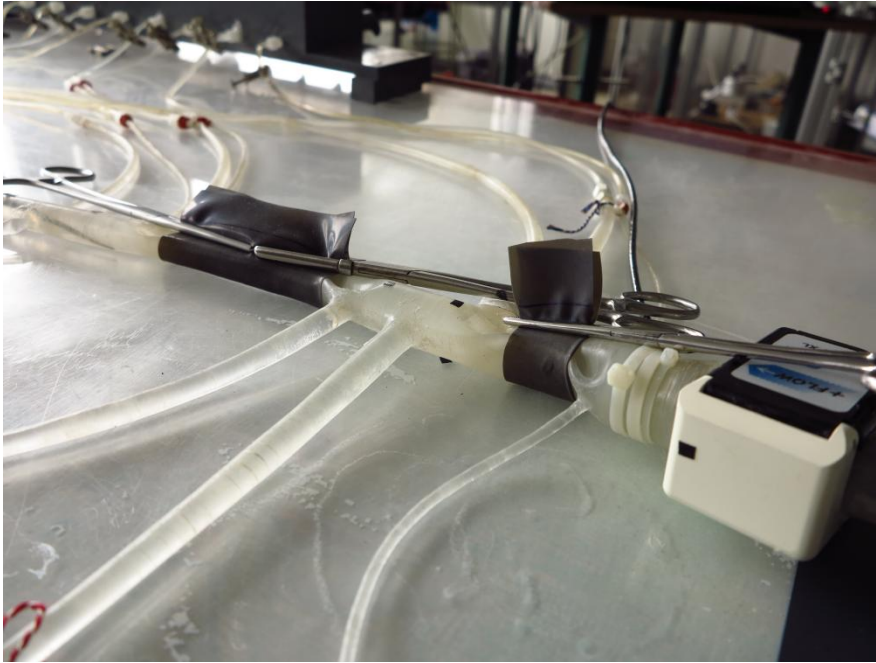


**Figure 5.4:** Detail of both AA and TA wraps clamped on the arterial model.

### 5.2.3 Hydraulic set-up

The silicon model was connected to a hydraulic set-up aimed at simulating physiological pressure and flow conditions. The flow was delivered by a pulsatile pumping system formed by an upstream pump (Pulsatile blood pump 1423, Harvard, USA) which delivered water into a downstream realistic left ventricular pump: here, the water entered a rigid chamber and squeezed a collapsible synthetic ventricle, which in turn pumped spurts of water into the circulatory model, creating realistic flow waves. The pumping system was flexible and the parameters that could be regulated were: stroke volume, pumping frequency (i.e. heart rate), and systole-to-diastole ratio.

The water entered the ventricular model from a pulmonary reservoir, where a constant pressure of 15 mmHg was maintained in order to simulate ventricular preload.

Between the ventricle and the arterial model, a water/air chamber (i.e. a Windkessel) was placed to modify the pressure waves and simulate central arterial compliance; however, for

the purposes of this study it was filled with water so that its effects were eliminated: since the aim was to focus solely on the changes in distensibility in the thoracic aortic segment determined by the AW procedure simulation, it was decided to eliminate any other compliance “source”, i.e. the Windkessel chamber, so that the only significant location with high distensibility in the whole model was the thoracic aorta.

At the distal ends of the arterial model, the outlet branches were connected to rigid silicone tubes, which ended into outflow reservoirs, which could be connected to volumetric surveys for mean flow measurements or, alternatively, to the central reservoir (**Figure 5.5**). At every end of the semi-rigid tubes, metal clamps were placed to regulate variable end resistances, in order to assess the desirable outflow distribution. The water in the central reservoir was pumped back to the pulmonary reservoir, thus creating a closed hydraulic loop.

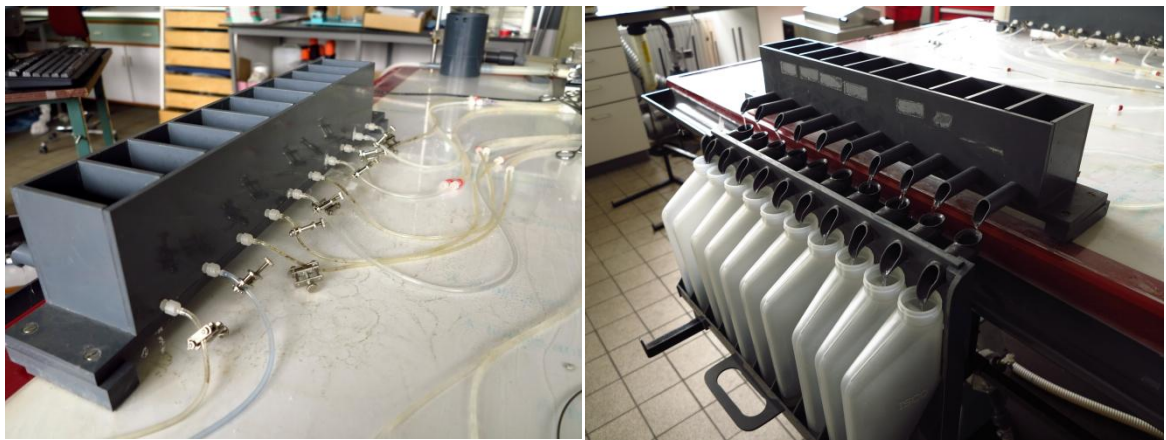


**Figure 5.5:** Detail of outflow reservoirs, seen from the model side (left) and from the outflow volumetric surveys side (right).

#### 5.2.4 Measurements

Pressure profiles were measured via a micro-tip catheter pressure sensor (Millar Instruments, Houston, TX, USA) (**Figure 5.1**). The measurements were performed at 10 different locations along the model, permanently marked on the surface of the model, as described in **Table 5.1**.

**Table 5.1:** List of 10 pressure measurement locations along the arterial model.

Denomination of measurement location	Position
1 inlet	At the inlet
2 AA	10.3 cm from inlet
3 aortic arch, between brachiocephalic and left common carotid	6.7 cm from location 2
4 aortic arch, between left common carotid and left subclavian	3.1 cm from location 3
5 descending thoracic aorta	2 cm from location 4
6 descending thoracic aorta	10.1 cm from location 5
7 abdominal aorta, between celiac trunk and renal bifurcation	4.7 cm from location 6
8 renal artery	2.9 cm from renal bifurcation
9 abdominal aorta, after renal bifurcation	4.7 cm from location 7
10 common iliac artery	2.2 cm from iliac bifurcation

The flow profile was measured with a transonic flowmeter (TS420; Transonic Systems Inc., Ithaca, NY, USA), whose probe (Transonic Flowprobe ME16PXL202) was placed around the rigid silicone tube connecting the Windkessel to the model inlet.

The signals of the transducers were connected to a data-acquisition unit (SC-2345; National Instruments, Austin, Texas, USA). The amplified signals were sampled at 1000 Hz and sent to a PC. The acquisition software was an in-house program written in LabVIEW 7.0 Express (2003) (National Instruments Inc., Austin, Texas, USA).

Calibration of pressure and flow signals was performed prior to the execution of the experiments. The pressure signal was calibrated by means of a water column. The flow signal had a two step calibration: “zero flow” was set when the pump was switched off by a dedicated command on the flowmeter; the mean flow was calculated by measuring the total outflow of the system (i.e. the volume of the water contained in the outflow volumetric surveys described in the section above) in a definite time interval, and later used in the post-processing phase to scale the recorded flow data.



### 5.2.5 Execution of the experiments

The experiment was performed on the unwrapped model first; subsequently, the AA wrap was placed around the AA segment of the model and the experiment was repeated; finally, a second wrap, the TA wrap, was placed between locations 5 and 6 and the experiment was performed a third time, with both wraps in place (**Figure 5.6**).

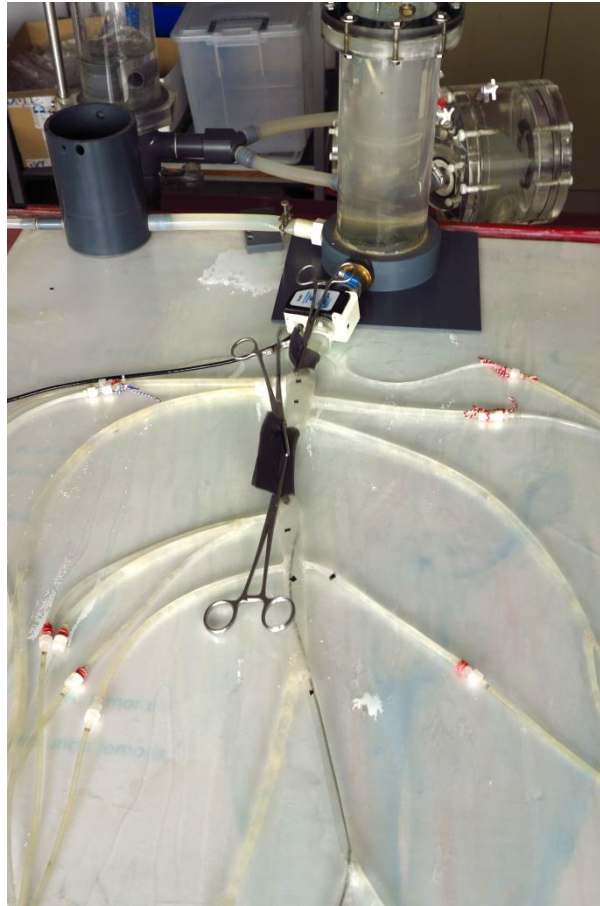


**Figure 5.6:** Execution of the double wrap experiment; both wraps are in place around the AA and TA, secured with metal clamps in order to induce a 70% diameter reduction at the respective aortic locations.

At the beginning of each experiment, the Millar catheter was inserted through a specific inlet in the femoral artery, positioned at the model inlet location for the first measurement, and then slowly retracted and stopped at each of the following 9 locations. Simultaneously, the inflow profile was always recorded as reference for the pressure measurements at every location. Pressure and flow signals were acquired for three seconds for every measurement location.

During each experiment, the stroke volume (SV) and heart rate (HR) of the pumping system were varied in the physiological range; the measurements were repeated for every combination of three different SVs (50, 60, and 70 ml) and three different HRs (50, 65, and 80 bpm).

The pressures achieved with this experimental set up were around 160/15 mmHg (SP/DP) at the AA site for 50 bpm heart rate and 70 ml stroke volume. Although mean and diastolic pressures were below the physiological range, pulse pressures were around 145 mmHg: the model was therefore useful to analyze PP reduction induced by AW.

### **5.2.6 Data analysis**

The data analysis was performed off-line using Matlab 7.0 (MathWorks, Natick, Massachusetts, USA) and Microsoft Excel (Microsoft Corporation, Redmond, Washington, USA).

A one-second pressure signal (corresponding to one beat) was extracted from every 3-seconds pressure and flow signal; the starting time reference was taken as the time instant 200 ms before the corresponding inflow curve maximum. This method allowed the time alignment of the measured pressure profiles, which could then be plotted as though recorded simultaneously.

It was then possible to compute and compare PP and SP for every wrapping configuration, at every location, and corresponding to every combination of HR and SV.

In the frequency ( $\omega$ ) domain, we calculated input impedance ( $Z(\omega)_{in} = P(\omega)/Q(\omega)$ ) of the arterial system for every wrapping configuration and SV-HR combination, using the pressure signal recorded at the input location, upstream from the AW.



Furthermore, characteristic impedance ( $Z_c$ ) was computed as the slope of a linearized section of the P-Q curve (using the pressure signal of the inlet location), corresponding roughly to the initial slope; more precisely, the linearization was made on the P-Q curve from 10% to 25% of the time frame between min and max of the pressure signal (**Figure 5.7**).

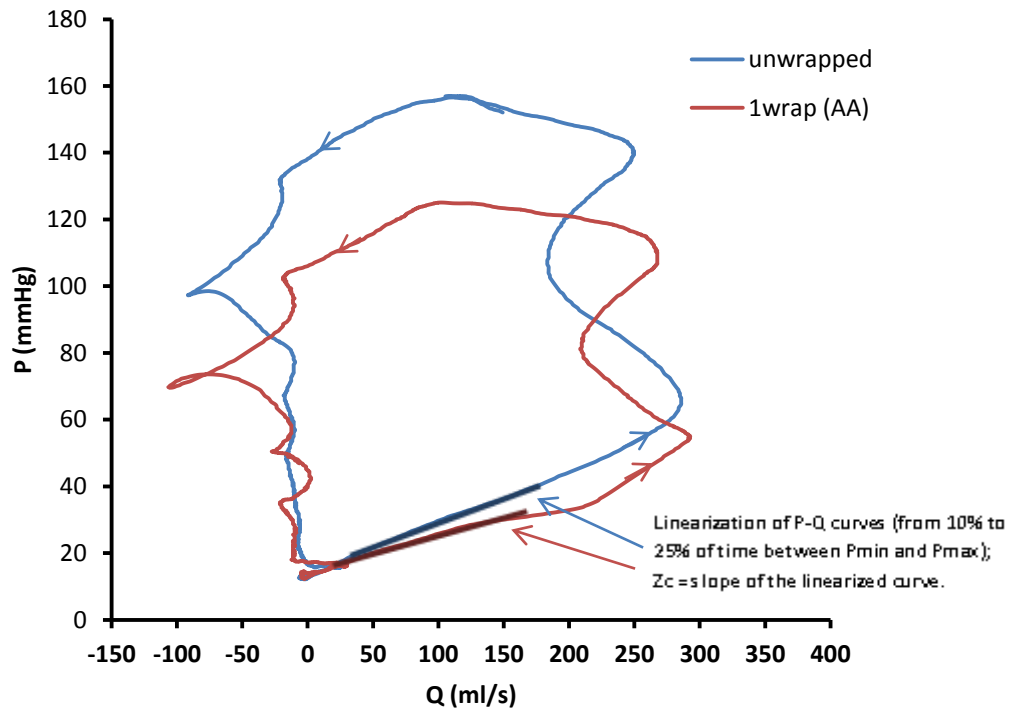


**Figure 5.7:** Calculation of  $Z_c$  as the slope of the curve (thick line) obtained by linearization of the P-Q curve (thin line loop), considering only the time frame from 10% to 25% of the time between the  $P_{min}$  and  $P_{max}$ .

## 5.3 Results

### 5.3.1 Reproducibility of the experiments

The reproducibility of the experiments was preliminarily tested by repetitive measurements at the inlet location, performed with a Millar catheter pressure sensor. The pressure signal was recorded for an arbitrary number of consecutive pulses; subsequently, PP was computed and its mean, standard deviation, and coefficient of variation were calculated. The signals recorded for the unwrapped, single wrap, and double wrap configurations were acquired

during different experiments. As shown in **Table 5.2**, the coefficient of variation was 0.33 %, 0.26%, and 0.07% for the unwrapped, single wrap, and double wrap configurations, respectively, thus ensuring a high reproducibility of the measured pressure values in each wrapping condition.

**Table 5.2:** Reproducibility test on PP measurements for unwrapped and wrapped experiment configurations.

	# Pulses	Mean PP (mmHg)	Std. Dev. (mmHg)	Coeff. Variation (%)
<b>unwrapped</b>	10	109.2	0.37	0.33
<b>1 wrap</b>	27	113.8	0.30	0.26
<b>2 wraps</b>	6	101.6	0.07	0.07

### 5.3.2 Pressure wave shape

Pressure and flow profiles at the AA location were plotted for a specific HR-SV combination, for the unwrapped and the two wrapped configurations, in order to have a qualitative indication of the pressure shape changes induced by wrapping. As shown in **Figure 5.8**, PP is visibly decreased after wrapping, with the greatest reduction of SP achieved by the AA wrap configuration without the additional TA wrap.

The same comparison was made for the pressure signals recorded at the renal artery location (**Figure 5.9**): again, the greatest drop in PP and SP was observed for the single AA wrap configuration.

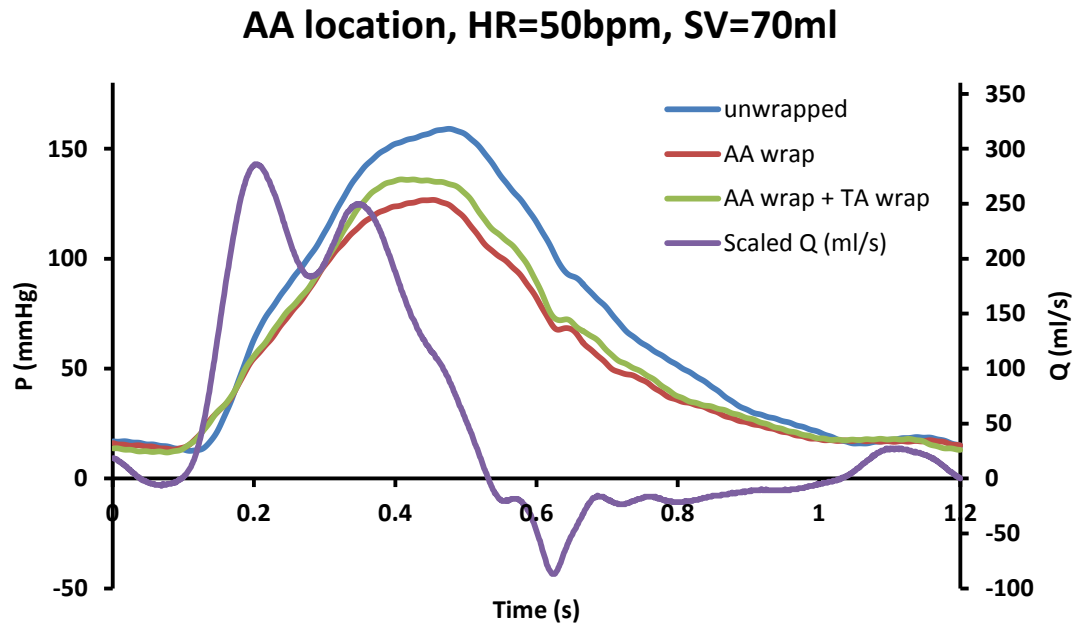


**Figure 5.8:** Graph of the synchronized pressure profiles (in mmHg) recorded at the AA location, for the unwrapped (blue line), single AA wrapped (red line), and double AA+TA wrapped (green line) configurations, for the 50 bpm - 70 ml HR-SV combination; a reference flow profile (in ml/s) is represented by the purple line.

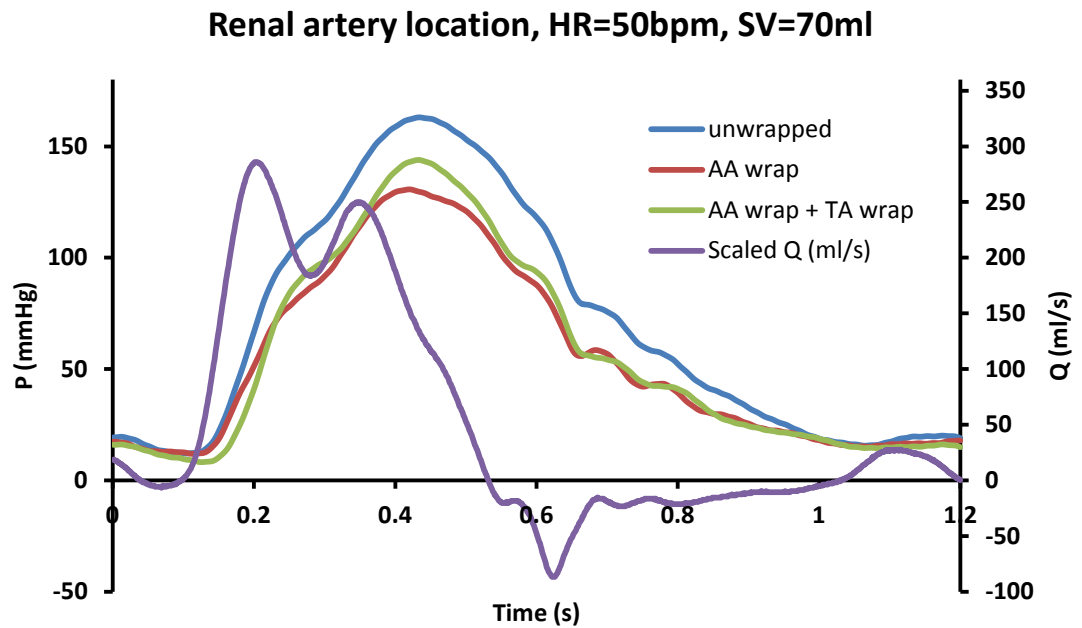


**Figure 5.9:** Graph of the synchronized pressure profiles (in mmHg) recorded at the renal artery location, for the unwrapped (blue line), single AA wrapped (red line), and double AA+TA wrapped (green line) configurations, for the 50 bpm - 70 ml HR-SV combination; a reference flow profile (in ml/s) is represented by the purple line.

### 5.3.3 PP and SP changes

In **Figure 5.10**, values of PP measured along the model at 10 different locations are plotted, both absolute (in mmHg) and normalized (divided by the value at the inlet), for the HR-SV combination of 50 bpm and 70 ml, for the unwrapped and the two wrapped configurations. A general PP amplification pattern towards the periphery of the model was observed for every configuration, but it was more evident for the wrapped configurations, especially for the (AA + TA) wrap. Moreover, a pulse pressure reduction effect after wrapping was observed at every location, with the maximum reduction obtained with the AA single wrap application. At the AA location (location 2) PP is decreased by 32.7 mmHg and 22.7 mmHg with the AA single wrap and the AA+TA double wrap respectively; similar values are observed at more distal locations.

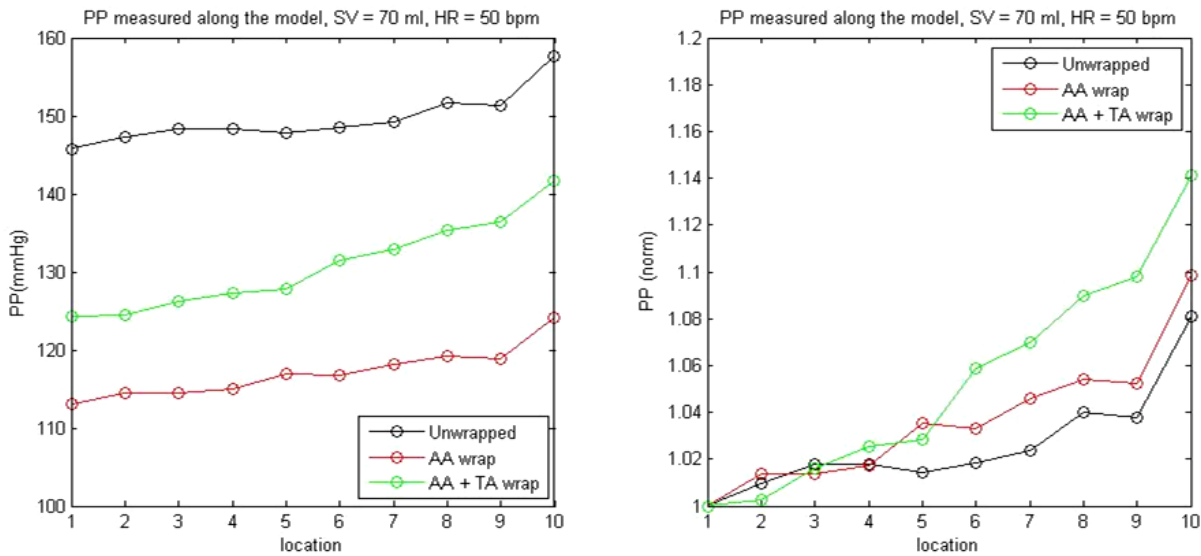


**Figure 5.10:** PP amplification measured at 10 different locations along the model, for the 50 bpm – 70 ml HR-SV combination, for the unwrapped (black line), single wrap (red line), and double wrap (green line) configurations. On the left panel, absolute values of PP at every location are represented in mmHg; on the right panel, PP at each location is represented as normalized to the PP value at the inlet for each wrapping configuration.

As shown by the plots in **Figure 5.11**, the PP drop measured after wrapping (calculated as the difference in PP between the wrapped and the unwrapped configurations, expressed as % of the unwrapped value at that location) was negative for almost all SV-HR combinations, for

almost every measurement location, for both wrapping configurations. The only exception was observed for the highest HR (80 bpm): after wrapping, depending on the HR-SV combination, PP slightly decreased (values  $> -5\%$ ), did not decrease, or slightly increased (values between 0 and 5 %); the latter scenario was observed for the double wrap configuration at the highest SV (70 ml). The maximum PP drops, instead, were measured for the lowest HR (50 bpm), for every configuration and every SV. The single AA wrap configuration achieved the highest absolute PP drops (-22.2%), measured for the HR-SV combination of 50 bpm and 70 ml, but the double AA+TA wrap configuration produced higher PP drops compared to the single wrap for low (50 ml) and medium (60 ml) SV values combined with low (50 bpm) and medium (65 bpm) HR values.

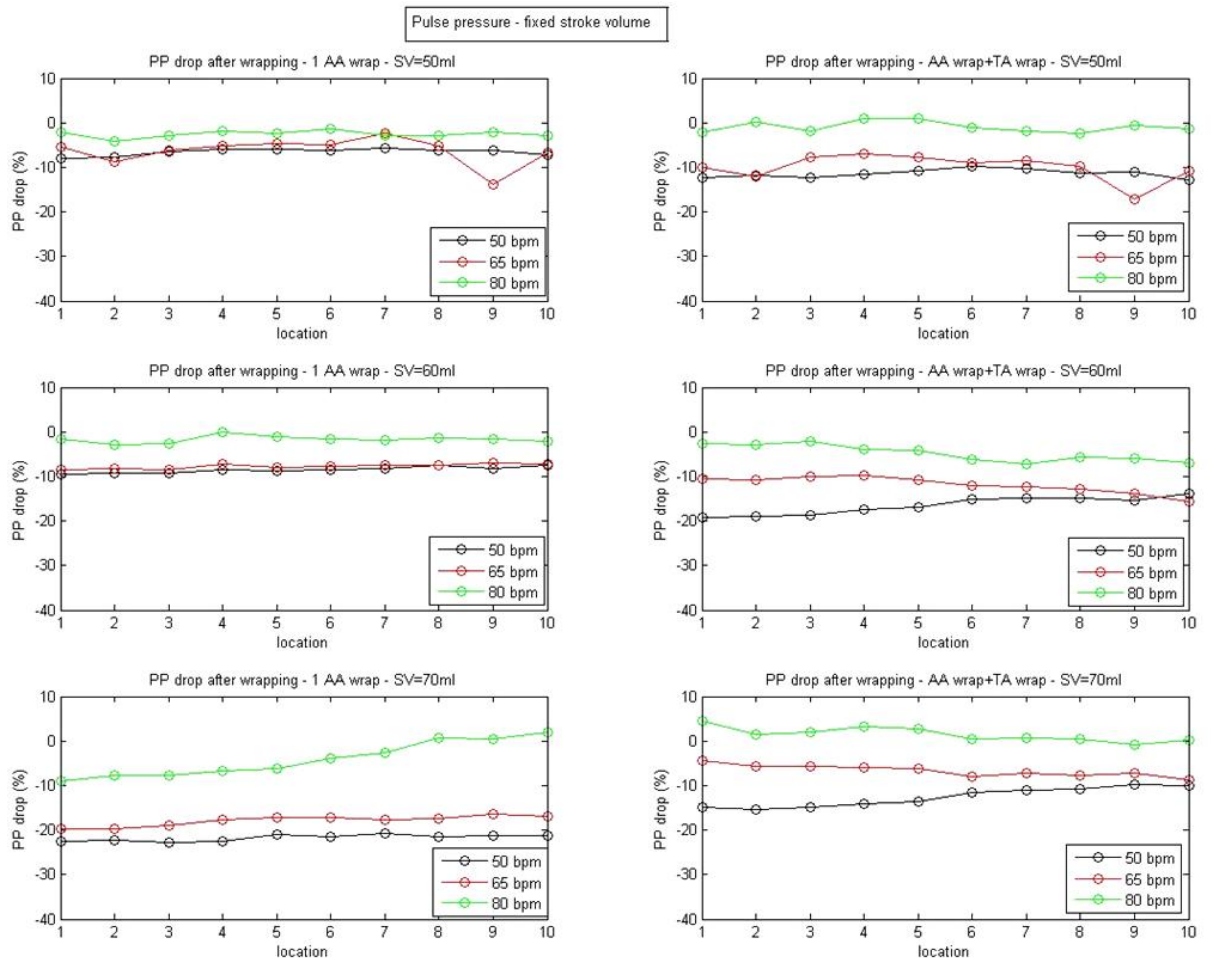


**Figure 5.11:** PP drop (calculated as difference in PP after wrapping) measured at 10 different locations along the model, for the single wrap (left panels) and double wrap (right panels) configurations, for 50 bpm (black line), 65 bpm (red line) and 80 bpm (green line) HR values, for 50 ml (upper row), 60 ml (middle row), and 70 ml (bottom row) SV values.

Similar patterns were observed for the SP changes after wrapping (**Figure 5.12**). The highest HR (80 bpm) produced the lowest SP drops after wrapping, whereas the largest drops were achieved at the lowest HR (50 bpm) for every wrapping configuration and every SV value. The largest SP reduction measured at the AA location was 30% of unwrapped SP and was obtained at 50 bpm HR, 70 ml SV, and single AA wrap configuration.

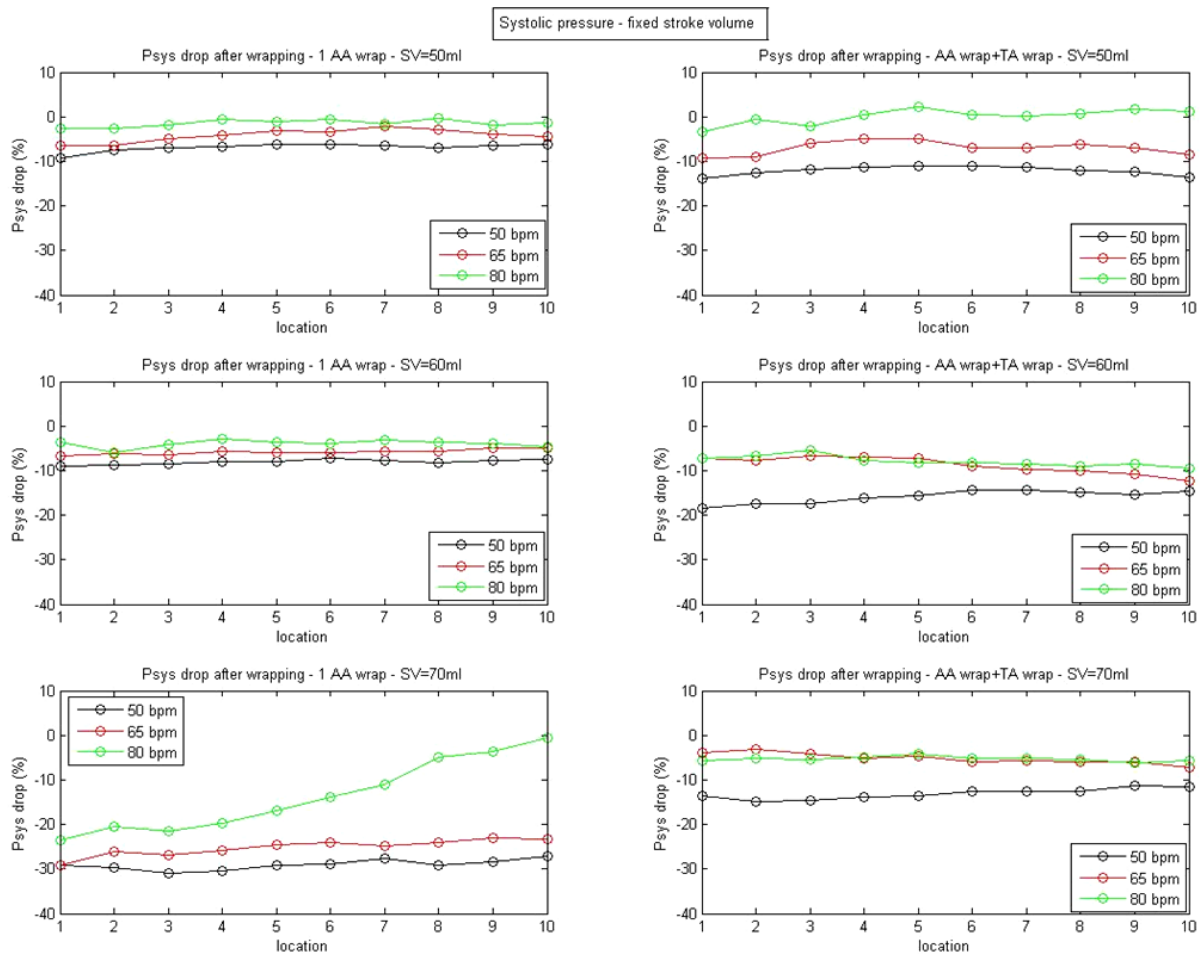


**Figure 5.12:** Systolic pressure drop (calculated as difference in SP after wrapping) measured at 10 different locations along the model, for the single wrap (left panels) and double wrap (right panels) configurations, for 50 bpm (black line), 65 bpm (red line) and 80 bpm (green line) HR values, for 50 ml (upper row), 60 ml (middle row), and 70 ml (bottom row) SV values.

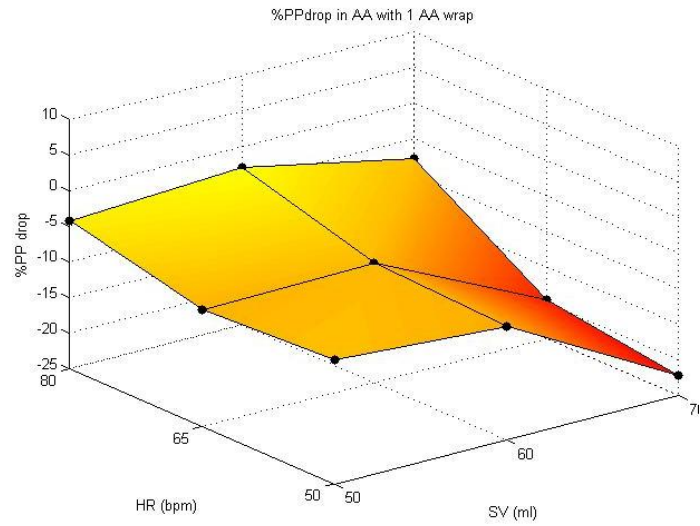


**Figure 5.13:** 3D plot of PP drop (as the difference in PP between wrapped and unwrapped configurations) for the single AA wrapped configuration measured at the AA location, for every HR-SV combination, expressed in % PP of the unwrapped configuration.

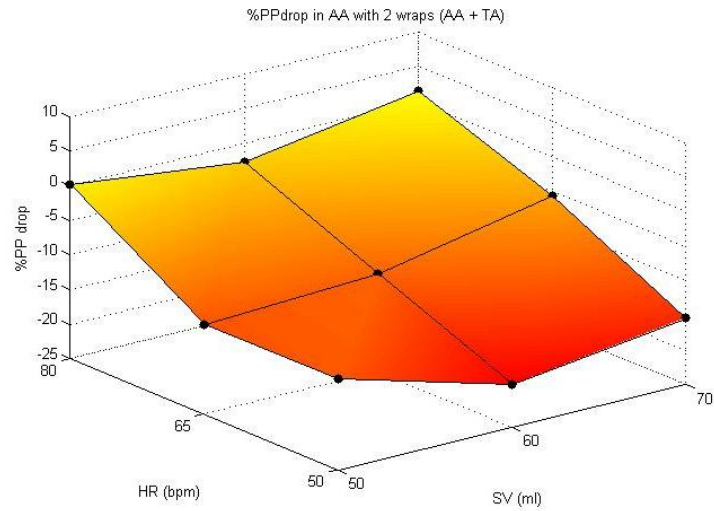


**Figure 5.14:** 3D plot of PP drop (as the difference in PP between wrapped and unwrapped configurations) for the double AA+TA wrapped configuration measured at the AA location, for every HR-SV combination, expressed in % PP of the unwrapped configuration.

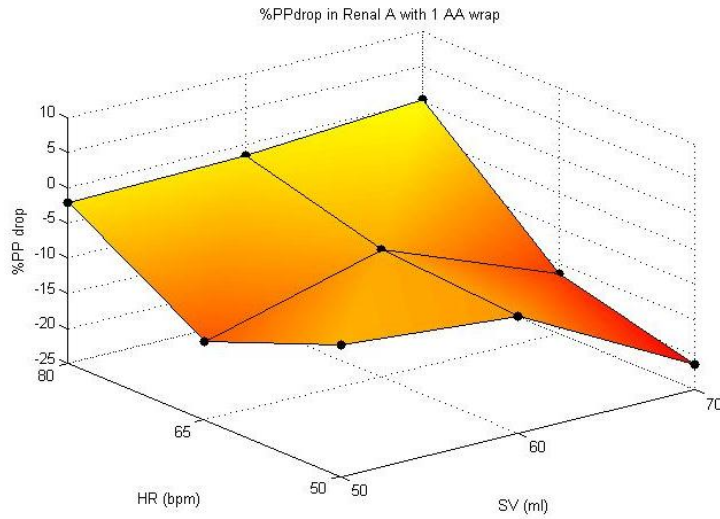


**Figure 5.15:** 3D plot of PP drop (as the difference in PP between wrapped and unwrapped configurations) for the single AA wrapped configuration measured at the renal artery location, for every HR-SV combination, expressed in % PP of the unwrapped configuration.

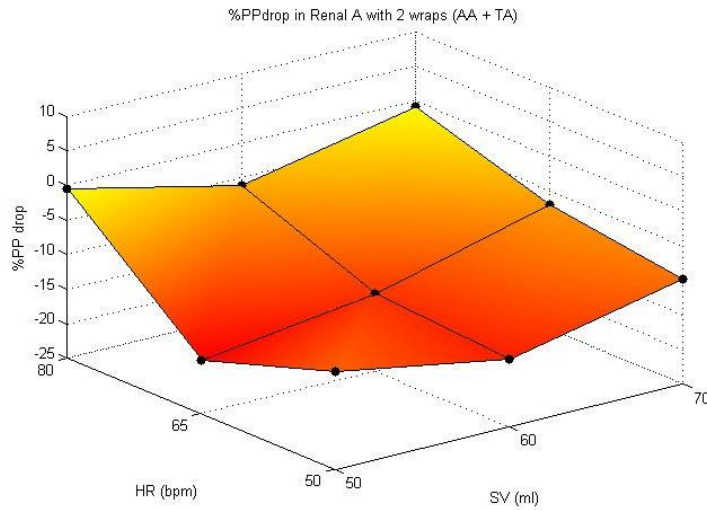


**Figure 5.16:** 3D plot of PP drop (as the difference in PP between wrapped and unwrapped configurations) for the double AA+TA wrapped configuration measured at the renal artery location, for every HR-SV combination, expressed in % PP of the unwrapped configuration.

In **Figure 5.13, 5.14, 5.15** and **5.16**, 3D plots of PP changes are shown, measured at the AA and renal artery locations, as % drops in PP after wrapping; they are represented for every SV and every HR, for both single and double wrap configurations. The graphs demonstrate the dependence of the PP drop on SV and HR: at both locations, for both wrapping configurations, the worst results (i.e. the smallest PP drops) are obtained at the highest HR (80 bpm). The biggest PP drops, instead, are reached at the lowest HR (50 bpm) and highest SV (70 ml) for the single AA wrapping configuration, whereas for the double AA+TA wrapping



configuration the minimum of the PP drop surface varies between middle (65 bpm) and low (50 bpm) HRs and middle (60 ml) and low (50ml) SVs.

### 5.3.4 $Z_c$ and $Z_{in}$ changes

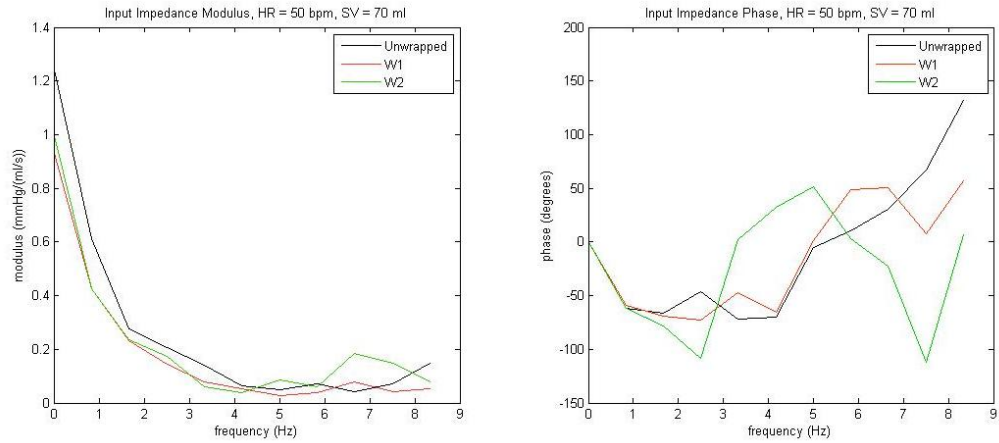


**Figure 5.17:** Input impedance modulus (left panel) and phase (right panel) of the arterial model, calculated for the 50 bpm – 70 ml HR-SV combination, for the unwrapped (black line), single wrap (red line), and double wrap (green line) configurations.

The modulus and phase of  $Z_{in}$  were computed and plotted for the HR-SV combination of 50 bpm and 70 ml, allowing a comparison between unwrapped and wrapped configurations (**Figure 5.17**). Both wrapped configurations determined a drop in every harmonic component of  $Z_{in}$  modulus up to the 5<sup>th</sup> harmonic. In particular, the static and the first harmonic components of both wrapped configurations decreased around 15% compared to the unwrapped one, while the 2<sup>nd</sup>, 3<sup>rd</sup>, and 4<sup>th</sup> components had a reduction of about 5%. Moreover, the  $Z_{in}$  phase of the single wrap configuration presented a similar pattern to the unwrapped one for the first five harmonics; the double wrap configuration, instead, showed a zero-crossing frequency that was about one third of the unwrapped one.

In figures **Figure 5.18**, **5.19**, and **5.20**,  $Z_{in}$  modulus and phase of the three configurations are compared, for every SV-HR combination. For a fixed SV, the largest reduction in the first 5 harmonics of  $Z_{in}$  modulus was obtained at the lowest HR (50 bpm), while at the highest HR

(80 bpm) the effects of wrapping were barely noticeable. The single wrap configuration produced the biggest reductions in  $Z_{in}$  modulus compared to the double wrap one, with the exception of the low SV (50 ml) combinations, in which the latter configuration induced the biggest changes. The  $Z_{in}$  phase graphs showed a lower zero-crossing frequency for both wrapped configurations compared to the unwrapped one, with the lowest zero-crossing frequency almost always produced by the double wrap configuration; these phase difference effect was smaller with increasing SV values.

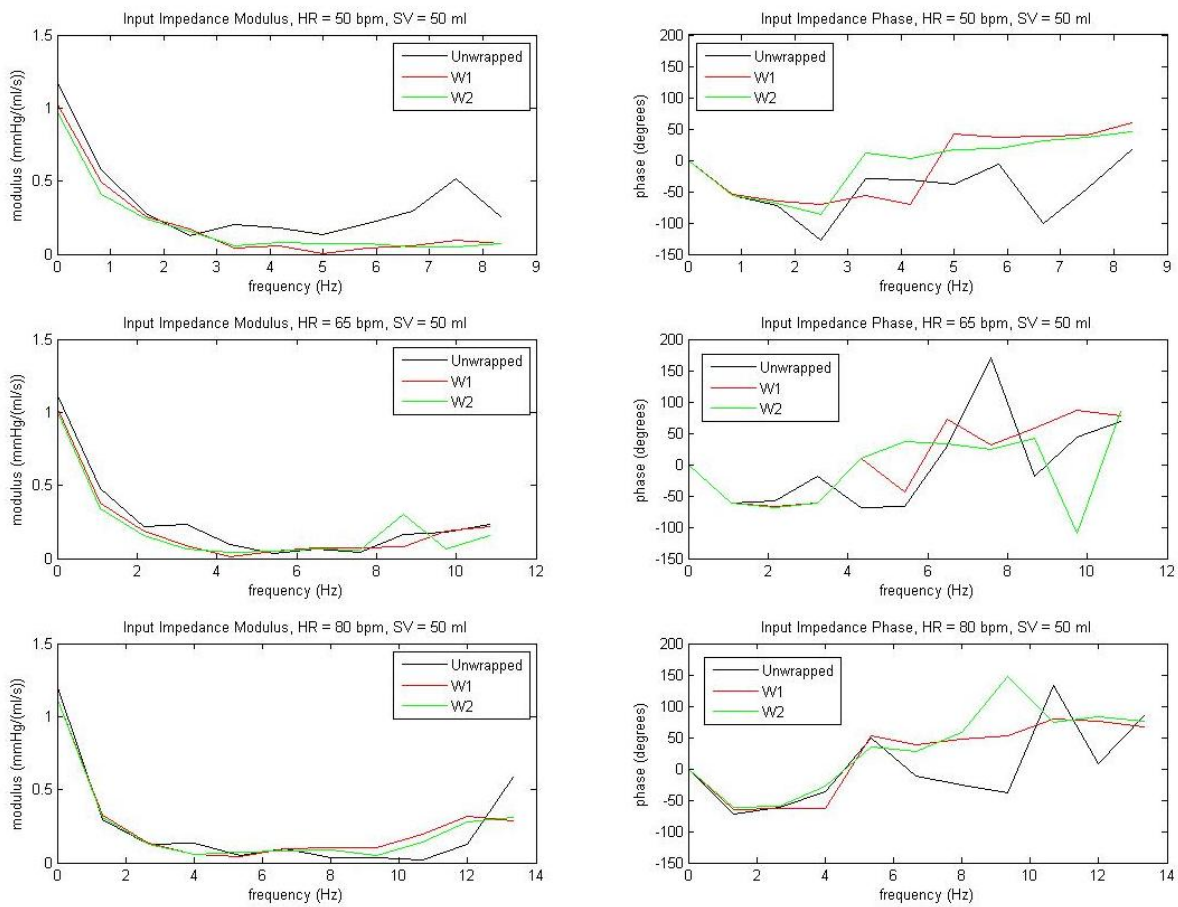


**Figure 5.18:** Input impedance modulus (left panel) and phase (right panel) of the arterial model, for the unwrapped (black line), single wrap (red line), and double wrap (green line) configurations, calculated for a fixed 50 ml SV and three different HRs: 50 bpm (top row), 65 bpm (middle row), and 80 bpm (bottom row).

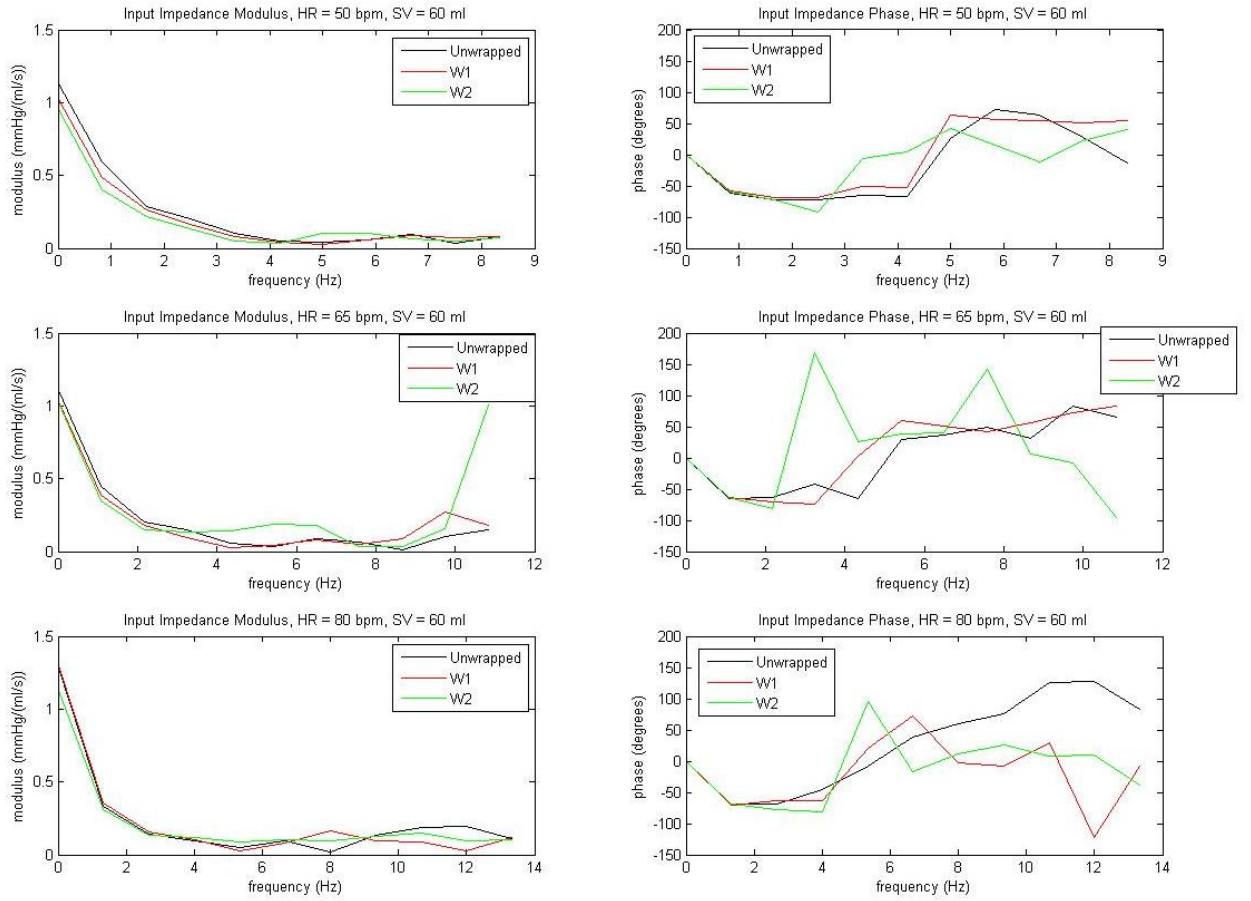


**Figure 5.19:** Input impedance modulus (left panel) and phase (right panel) of the arterial model, for the unwrapped (black line), single wrap (red line), and double wrap (green line) configurations, calculated for a fixed 60 ml SV and three different HRs: 50 bpm (top row), 65 bpm (middle row), and 80 bpm (bottom row).

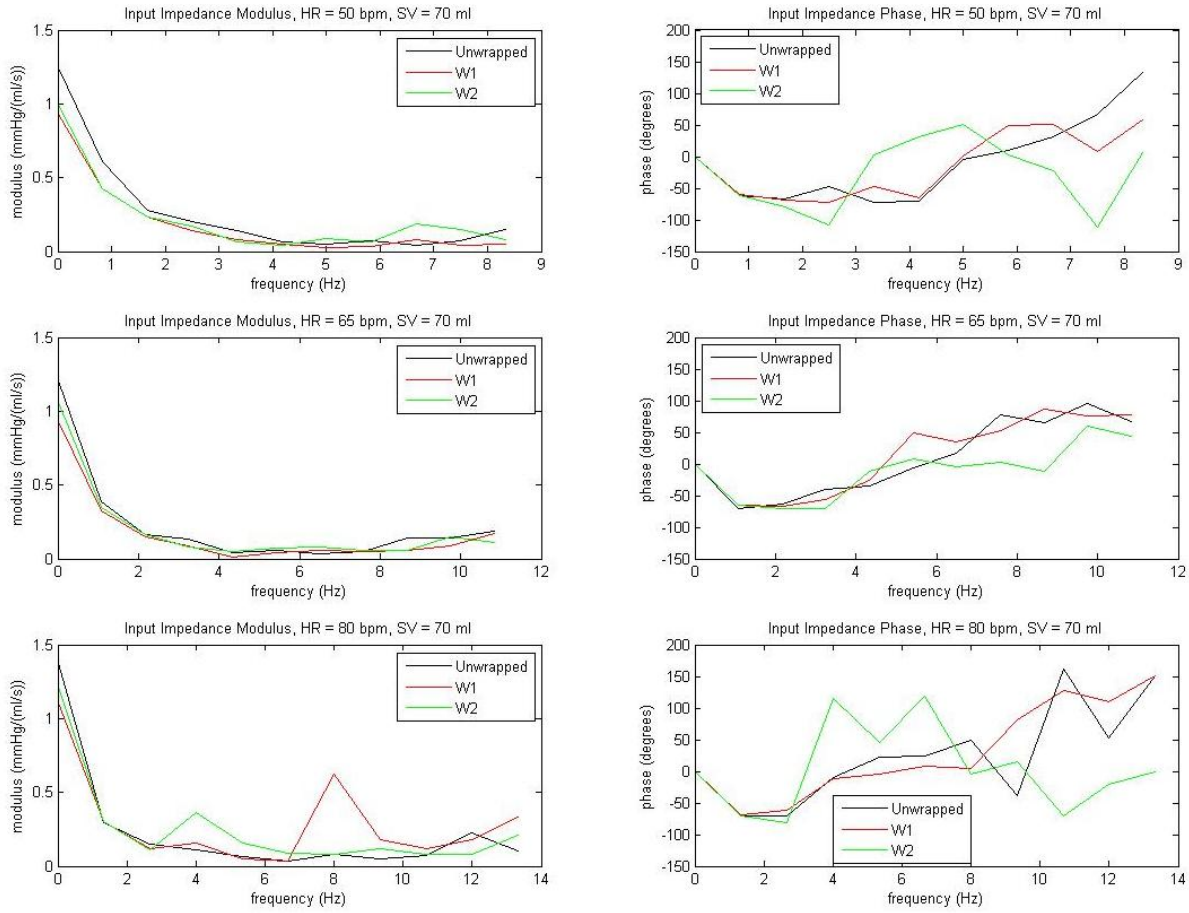


**Figure 5.20:** Input impedance modulus (left panel) and phase (right panel) of the arterial model, for the unwrapped (black line), single wrap (red line), and double wrap (green line) configurations, calculated for a fixed 70 ml SV and three different HRs: 50 bpm (top row), 65 bpm (middle row), and 80 bpm (bottom row).

$Z_c$  was calculated from the initial slope of the P-Q curve, as explained in the *methods* section of this chapter. The effects of wrapping on  $Z_c$  values are presented in **Table 5.3** and **Table 5.4** as absolute (in mmHg/(ml/s)) and relative (in %) difference in  $Z_c$  between each wrapped configuration and the unwrapped one. The single AA wrap configuration induced a reduction of  $Z_c$  across all SV and HR combinations, with the exception of the highest HR (80 bpm) and lowest SV (50 ml) combination, at which no  $Z_c$  was observed. The double AA+TA wrapped configuration, instead, produced a reduction of  $Z_c$  in only 5 out of 9 configurations, as  $Z_c$  increased for all combinations at the highest HR (80 bpm) and for intermediate HR (65 bpm) and SV (60 ml). The biggest  $Z_c$  reduction (-41.9 %) was achieved by the single wrap configuration at the lowest HR (50 bpm) and lowest SV (50 ml).

**Table 5.3:** Difference of  $Z_c$  values between the single AA wrapped configuration and the unwrapped one, expressed in mmHg/(ml/s) (absolute difference) and % of unwrapped  $Z_c$  (relative difference).

<b>Zc absolute drop (mmHg/ml s<sup>-1</sup>)</b>			
	<b>SV (ml)</b>		
<b>HR (bpm)</b>	<b>50</b>	<b>60</b>	<b>70</b>
<b>50</b>	-0.072	-0.049	-0.011
<b>65</b>	-0.060	-0.046	-0.034
<b>80</b>	0.000	-0.006	-0.020

<b>Zc relative drop (%)</b>			
	<b>SV (ml)</b>		
<b>HR (bpm)</b>	<b>50</b>	<b>60</b>	<b>70</b>
<b>50</b>	-41.9	-30.6	-6.0
<b>65</b>	-41.1	-30.4	-29.1
<b>80</b>	0.0	-5.8	-17.5

**Table 5.4:** Difference of  $Z_c$  values between the double AA+TA wrapped configuration and the unwrapped one, expressed in mmHg/(ml/s) (absolute difference) and % of unwrapped  $Z_c$  (relative difference).

<b>Zc absolute drop (mmHg/ml s<sup>-1</sup>)</b>			
	<b>SV (ml)</b>		
<b>HR (bpm)</b>	<b>50</b>	<b>60</b>	<b>70</b>
<b>50</b>	-0.102	-0.036	-0.093
<b>65</b>	-0.002	+0.012	-0.042
<b>80</b>	+0.035	+0.001	+0.024

<b>Zc relative drop (%)</b>			
	<b>SV (ml)</b>		
<b>HR (bpm)</b>	<b>50</b>	<b>60</b>	<b>70</b>
<b>50</b>	-59.2	-22.3	-51.8
<b>65</b>	-1.3	+7.8	-35.9
<b>80</b>	+39.7	+1.3	+20.5

## 5.4 Discussion

### 5.4.1 Efficacy in PP and Z reduction

The pulsatile experiments conducted on a distributed silicon model proved in a definitive way that elastic wrapping of the thoracic aorta produces a reduction of aortic pulse pressure, which translates to a concomitant reduction of aortic systolic pressure, without significant variations of diastolic pressure. This pressure decrease was dependent on the wrapping configuration used (i.e. single AA wrap or double AA+TA wrap) and on the hemodynamic settings of the

experiment: SV and HR were found to influence the results significantly. More specifically, the PP reduction achieved after wrapping varied from -22.2% for the “50 bpm - 70 ml” HR-SV combination with a single AA wrap, to virtually no PP reduction for the double wrap configuration at a high HR (80 bpm) for every SV value. Aortic input and characteristic impedance were also reduced by elastic wrapping and, similarly to PP and SP reduction, the results depended on wrapping configuration and hemodynamic settings. This factor is of high importance for future clinical applications of the Aortic Wrap: it suggests that patient-specific hemodynamic parameters will have to be considered for an optimal wrap choice.

#### **5.4.2 Unloading mechanism**

The principle that determines PP reduction is *aortic wall unloading*: by using highly distensible elastic wraps to reduce the aortic diameter of the model, it was possible to unload the vessel wall and transfer the load-bearing function to the wrap. The unloading mechanism was achieved in the silicon arterial model by collapsing the ascending aortic segment, which assumed a “folded” cross-sectional shape, and acted as a conduit with no buffering function; the latter was taken over by the elastic wrap, consistently with the results obtained for the static investigation detailed in Chapter 4 of this thesis: the increased distensibility of the wrapped arterial segment determined a decrease in input impedance of the arterial tree, thus effectively increasing the pulsation dampening function of the wrapped segment. The unloading mechanism is expected to work similarly *in vivo*: instead of “folding”, the aortic wall is expected to collapse by reducing its diameter and maintaining a round- or elliptical-shaped lumen; the reduction in aortic wall tension caused by an extra-luminal pressure reduction, achieved by wrapping, will translate into a reduction of intra-luminal pressure, according to Laplace’s law.

### 5.4.3 Comparison with “stiffening” wrapping studies

The PP reduction results obtained by the Aortic Wrap can be related to previous studies which investigated the opposite concept: aortic pulse pressure augmentation obtained by means of stiff wraps applied around the thoracic aorta or substitution of healthy distensible segments of the aorta with rigid prosthetic vessels (O’Rourke 1967; Ioannou et al. 2009; Kelly, Tunin, and Kass 1992). In particular, in the study by Ioannou *et al.*, after wrapping the aortas of 6 pigs with rigid Teflon wraps, aortic compliance was reduced by approximately 50% on the second post-operative day and, as a consequence, PP was increased by 86%. Pressure reduction values achieved by the Aortic Wrap in this pulsatile study are not as marked as the pressure increase obtained by Ioannou *et al.*; nevertheless, it should be noted that unloading a pressurized vessel by an external wrap is less efficient and technically more challenging than stiffening said vessel by means of a rigid sleeve. Therefore, a smaller PP variation is expected for a vessel “unloading” experiment compared to a “loading” one.

### 5.4.4 Limitations of the study

The distributed silicon model and experimental set up used in this study proved to be efficient in the investigation of aortic PP and impedance reduction caused by the Aortic Wrap. Nevertheless, the model had some limitations. First of all, realistic diastolic pressures couldn’t be achieved, due to the physical limitations of the model; however, it was possible to obtain high values of systolic pressure, which determined realistic values of pulse pressure, on which the investigation was focused.

Moreover, the “unloading” mechanism of the silicon arterial wall didn’t mimic the expected *in vivo* behaviour of the aortic wall: the big fold that was created in the lumen shape after wrapping is typical of a homogenous synthetic material like silicon; the aortic wall, instead, is expected to collapse keeping a round lumen shape, simply by decreasing internal wall tension,

due to the unloading of elastin lamellae composing the medial layer of the wall. The results obtained by the model can therefore be influenced by the irregular collapsed shape of the silicon model.

The dependence of the AW pressure reduction efficacy on heart rate, stroke volume, diameter reduction, and location of application along the aorta observed in this experimental study indicates that potential clinical results will similarly be dependent on patient-specific cardiovascular parameters. This could constitute a limitation of the AW, which can be seen as not reliable in the delivery of consistent results; on the other hand, though, patient-specificity could be a valuable asset of the AW, enabling a tailored surgical procedure aimed at obtaining optimal pressure-lowering capabilities. Therefore, this characteristic of the AW should be further explored in more accurate models of the arterial system, such as big animal models.



# Chapter 6

## *Computational fluid dynamic study of the effects on velocity patterns and wall shear stress of the ascending aortic diameter reduction induced by wrapping*

### **6.1 Introduction**

The Aortic Wrap (AW) is a proposed device able to restore high distensibility in the old stiffened ascending aorta (AA) and to decrease aortic pulse pressure (PP) as a consequence. The vessel distensibility is increased by means of aortic wall *unloading*: the AW is made of a highly distensible material and is wrapped around the AA by decreasing its diameter; this feature allows the AA walls to be partially collapsed inside the AW, while the latter bears the pulsatile load and function as a PP buffer. Aortic wall unloading is therefore crucial for the

AW effectiveness in reducing PP, and the concomitant aortic lumen reduction is a necessary factor to allow the unloading to take place. Aortic lumen, or diameter, reduction is then obligatory for successful function in AW implementation, but is expected to cause local hemodynamic changes in wall shear stress (WSS) and blood velocity ( $v$ ).

Disturbances in flow and WSS patterns in the thoracic aorta are well established factors in the pathogenesis of cardiovascular disease, and more specifically of endothelial dysfunction, aortic wall remodelling, thrombosis and hemolysis (Nichols et al. 2011). It is safe to assume that the aortic wall geometry modifications caused by AW-associated aortic lumen reduction will have a detrimental impact on the local hemodynamics of the wrapped aortic section and the adjacent ones.

It is therefore important to simulate the geometrical changes induced by the AW, in terms of AA diameter reduction, and investigate the effects of these changes on hemodynamics in the aortic arch as well as in a straight segment of the aorta. For this purpose, geometrical models of the AA and the aortic arch were created and computational fluid dynamic (CFD) simulations were performed.

## **6.2 Methods**

### **6.2.1 Geometrical models**

The aortic region of interest was simulated by 3D geometric models created in ICEM CFD (ANSYS Inc, Cecil Township, PA, USA). The models developed were divided into two categories:

- **STRAIGHT TUBE MODELS**

The unwrapped (UW) model was represented by a straight tube with a diameter of 2.2 cm and length of 22cm. The dimensions were chosen in order to reproduce the geometry of an experimental aortic model used in previous studies (i.e. the fabric aortic model detailed in Chapter 4 of this thesis). The UW geometry was used to create 16 wrapped geometrical configurations, characterized by 4 different wrap lengths (5, 10, 15, 20 cm) and 4 different wrap diameters (90%, 80%, 70%, and 60% of the AA diameter, corresponding to 10%, 20%, 30% 40% diameter reduction). **(Figure 6.4)**

- **REALISTIC ARCH GEOMETRY MODELS**

Real geometrical data typical of > 70 year old human subjects were derived from literature (Redheuil et al. 2011) and used to build realistic 3D models of the unwrapped and wrapped aortic arch (**Figure 6.1**). The model comprised the AA and the aortic arch, with the inlet being the aortic root and the outlet being the end of the arch and the beginning of the descending thoracic aorta (**Figure 6.2**). The AA inlet lumen diameter was 3.32 cm, and it tapered until the centre of the arch, where it reached a constant value of 2.43 cm until the outlet. The arch was characterized by a height of 4.15 cm and a width of 7.85 cm (from the centre of the inlet to the centre of the outlet). The wrapped models were created by reducing the diameter of the AA, keeping a round cross-section and a linear transition between unwrapped and wrapped sections of the model. Different wrapping configurations were simulated and were defined as model A (characterized by a 3.9 cm wrapping length, starting from 0.65 cm from the inlet) and model B (characterized by a 3.25 wrapping length, starting from 1.3 cm from the inlet) (**Figure 6.3**); each model configuration, A and B, had 3

wrapping diameter variations (70%, 80%, and 90% of the AA inlet diameter), therefore achieving a total of 6 different diameter-length wrapping configurations.

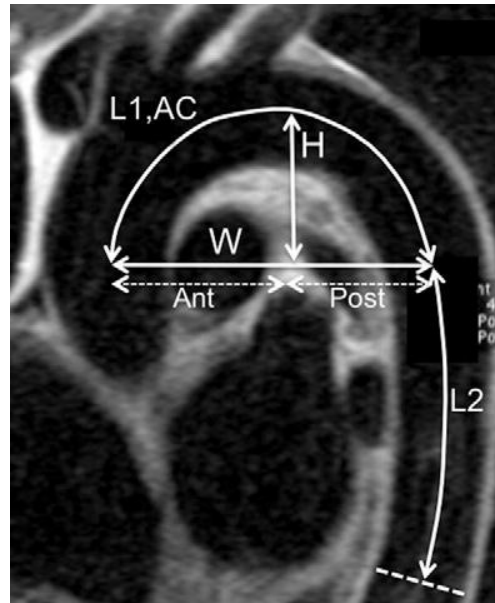


**Figure 6.1:** Sagittal oblique view of the thoracic aorta using MRI acquisition, illustrating thoracic aortic geometry. AC = average arch curvature; Ant = anterior arch width; H = arch height; L1 = length of the aortic arch; L2 = length of the descending aorta; Post = posterior arch width; and W = arch width. Reproduced from Redheuil *et al.* (Redheuil et al. 2011)

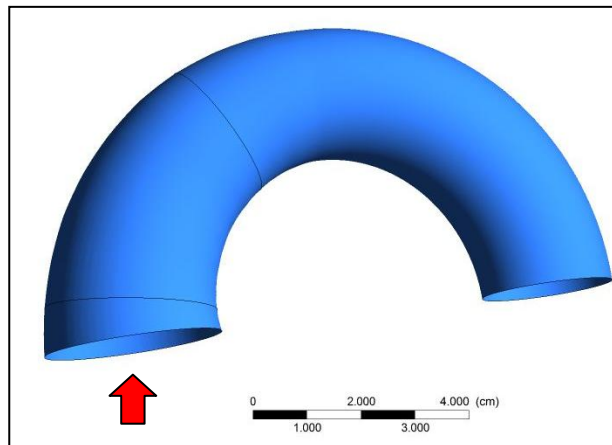


**Figure 6.2:** 3D geometrical realistic model of the aortic arch: unwrapped configuration. The red arrow indicates the inlet.

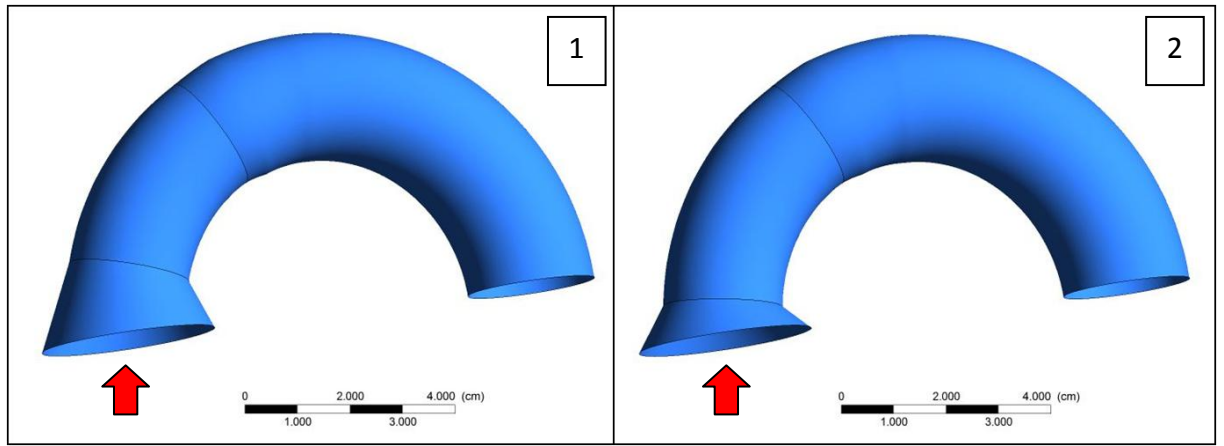


**Figure 6.3:** 3D geometrical realistic model of the aortic arch: panel 1) model type B, shorter wrapping length, 70% D; panel 2) model type A, longer wrapping length, 70% D. Red arrows indicate the inlet.

## 6.2.2 Discretization

The 3D models were subsequently discretized. Mesh sensitivity tests were performed to avoid the dependency of CFD simulation results on the number of mesh elements.

- **STRAIGHT TUBE MODELS:**

A hexahedral mesh with a prismatic layer on the walls was created with ANSYS Meshing 12.1 (ANSYS Inc, Cecil Township, PA, USA). The element size was 0.1 cm and the number of prismatic layers was 8, with growth rate of 1.2 and maximum thickness of 0.3 cm. (**Figure 6.4**). The final total number of elements obtained for every configuration was 62,629.

- **REALISTIC ARCHED MODEL:**

A tetrahedral mesh with a prismatic layer was created with a Delaunay meshing method, using ICEM CFD 12.1 (ANSYS Inc, Cecil Township, PA, USA) (**Figure 6.5**). The maximum element seed size chosen was 0.08 cm and the number of prismatic layers was 6 with height ratio of 1.2. The final element numbers obtained for the different geometrical configurations is shown in **Table 6.1**.

**Table 6.1:** Number of mesh elements obtained for the UW and wrapped configurations.

UW	WRAPPED			
	model type	diameter (% unwrapped diameter)		
		60	70	80
896.687	A	847,132	923,592	1,004,442
	B	879,030	941,917	1,019,261

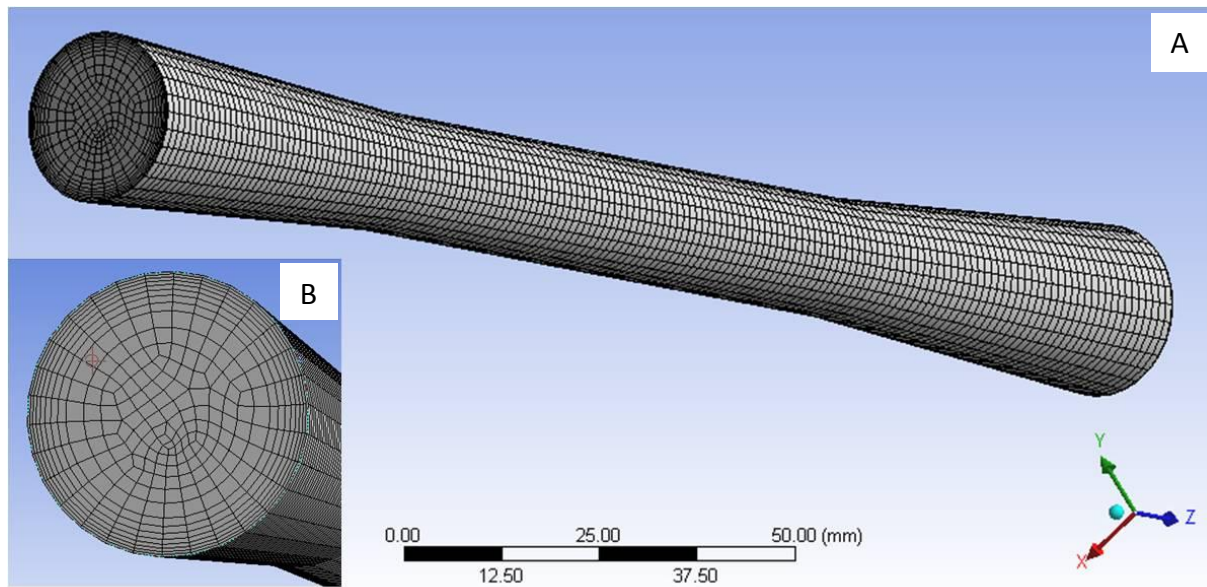


**Figure 6.4:** Example of hexahedral mesh created for the straight models of the aorta. Panel A: whole mesh of the wrapped model characterized by wrapping L of 10 cm and wrapping diameter of 70% D; panel B: detail of the inlet mesh of the model displayed in panel A.

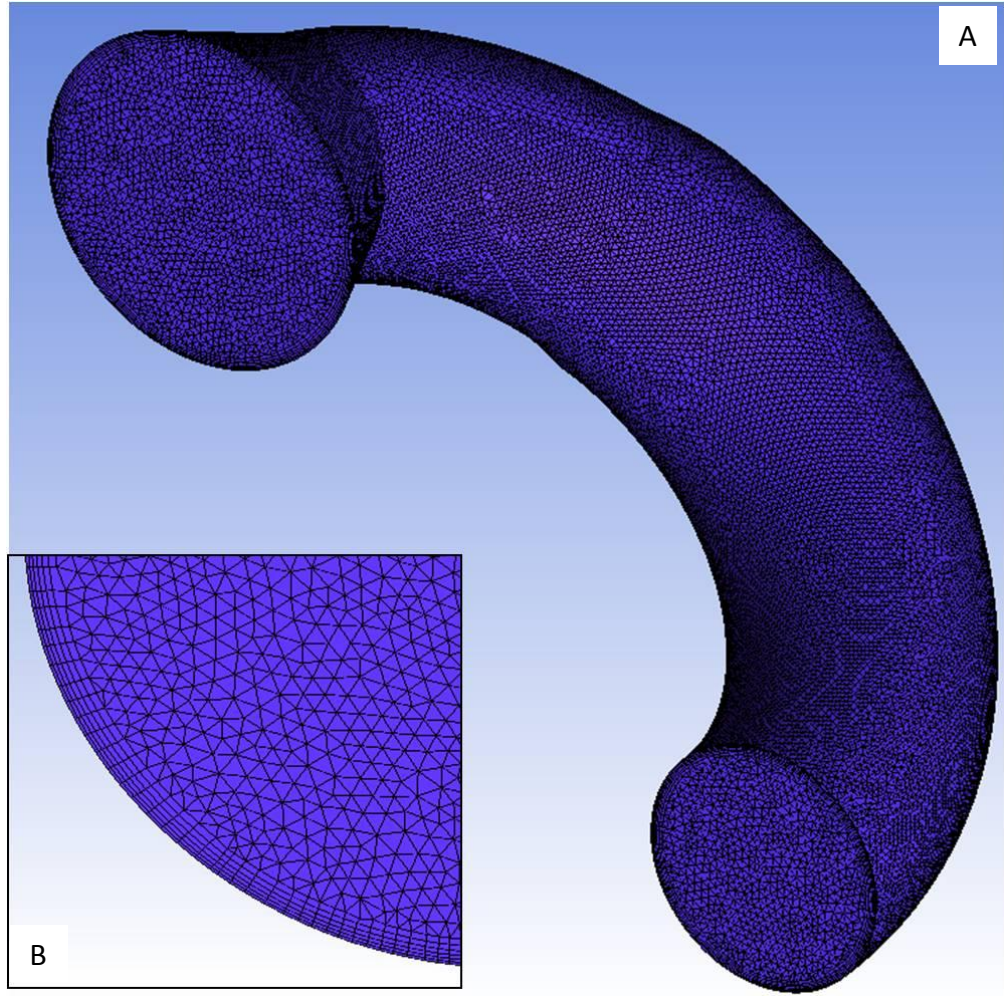


**Figure 6.5:** Example of tetrahedral mesh created for the realistic curved models of the aortic arch. Panel A: whole mesh of the wrapped model type B (characterized by a shorter wrapping length) and wrapping diameter of 70% D; panel B: detail of the inlet mesh of the model displayed in panel A.

### 6.2.3 Fluid dynamic simulations

A CFD investigation was performed with ANSYS Fluent 12.1 (ANSYS Inc, Cecil Township, PA, USA), applying a physiological steady flow velocity at the inlet, imposing a no-slip boundary condition on the walls and a traction-free ( $P = 0$  mmHg) boundary condition at the outlet. The fluid was considered an incompressible Newtonian fluid with blood density ( $\rho = 1050 \text{ kg/m}^3$ ) and viscosity ( $\mu = 0.03 \text{ kg/m} \cdot \text{s}$ ), and the arterial wall deformation was neglected. The solving pressure-velocity coupling algorithm chosen was SIMPLE, with a second order upwind spatial discretization scheme. The solution of the momentum and continuity equations was considered to have reached convergence when residuals became  $< 10^{-4}$ .

The imposed inlet velocity values were calculated for the 2 different model categories starting from the assumption of an average resting cardiac output of 5 l/min: given the AA inlet area, the derived inlet velocity was 0.22 m/s and 0.1 m/s for the straight model and the realistic arch model, respectively.

## 6.3 Results

### 6.3.1 Straight model

Wall shear stress was calculated for the whole surface of the models and maximum values obtained for every configuration are shown in **Table 6.2** and visualized in **Figure 6.6**, normalized for the UW configuration value. Maximum WSS is increased for every wrapping diameter and length combination, with the largest increase (more than threefold the UW value) registered for high diameter reduction (60% D) and longest wrapping length (20 cm); conversely, the smallest maximum WSS increase was obtained for the smallest diameter reduction (90% D) and the shortest wrapping length (5 cm). For every wrapping length, the increase in maximum WSS with decreasing diameter was only slight from 90% D to 70% D, but was subject to a sharp augmentation from 70% D to 60% D, indicating 70% D as a threshold diameter below which the AW effects on WSS increase are more marked.

**Table 6.2:** Maximum WSS values calculated for every geometrical configuration of the straight AA model; values are normalized to the max WSS value of the unwrapped straight model.

D (%)	Max WSS (norm)			
	L wrap (cm)			
	5	10	15	20
60	1.13	1.32	1.70	3.11
70	1.03	1.04	1.07	1.73
80	1.02	1.03	1.05	1.14
90	1.01	1.02	1.04	1.05



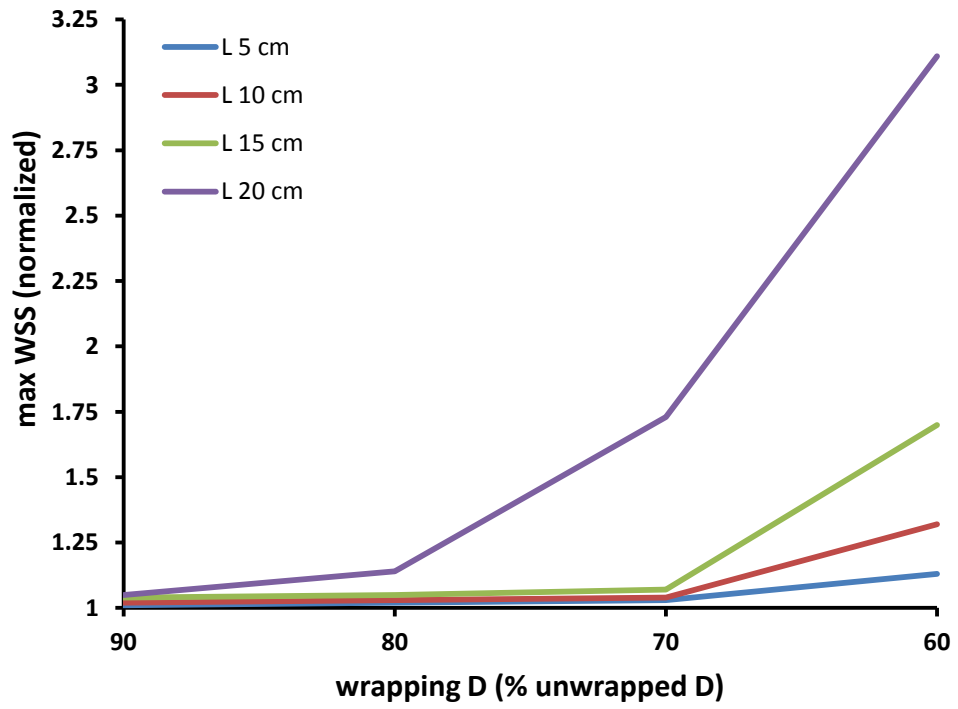


**Figure 6.6:** Maximum WSS values (normalized for the UW maximum WSS) calculated for every wrapped configuration: four different wrapping D (90%, 80%, 70%, and 60% of the UW D, displayed on the horizontal axis) and four different wrapping lengths (5 cm in blue, 10 cm in red, 15 cm in green, and 20 cm in purple).

As shown in **Figure 6.7**, peaks of WSS were located primarily around the inlet of the wrapped section for models with high diameter reductions, or at the inlet wall for the smoother models characterized by smaller diameter reductions.

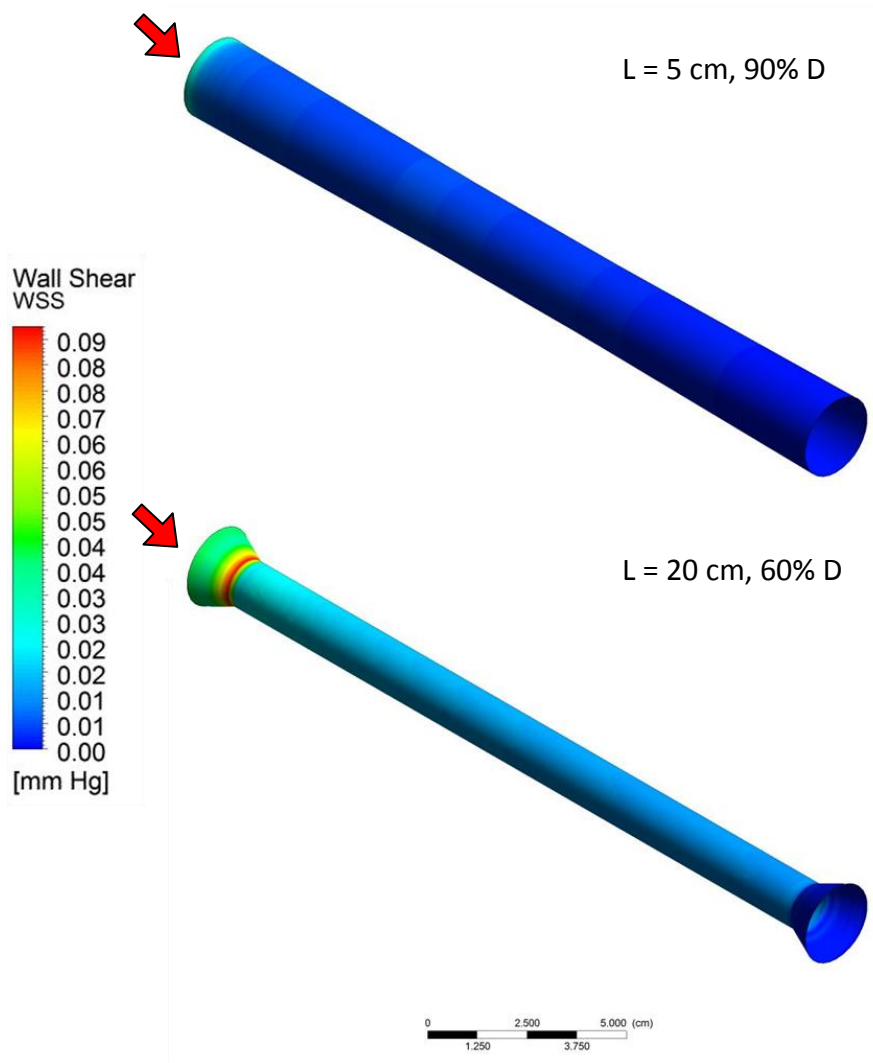


**Figure 6.7:** WSS plots (mmHg) on the surface of two wrapped models; top: model characterized by 5 cm wrapping length and 90% D (lower maximum WSS value), presenting maximum values of WSS located at the inlet wall; bottom: model characterized by 20 cm wrapping length and 60% D (higher maximum WSS value), presenting maximum values of WSS located at the proximal edge of the wrapped section. Red arrows indicate the inlet.

Fluid velocity was calculated and maximum values are presented in **Table 6.3**: for every wrapping configuration maximum velocity increased between 1.13 and 2.74 times compared to the UW model. Maximum values of velocity were obtained for the highest diameter reduction (60% D) and longest wrapping length (20 cm). Similarly to what described for the maximum WSS values, the sharpest increase of max velocity for every fixed wrapping length was observed when the diameter was reduced from 70% D to 60% D. Moreover, for every configuration velocity peaks were located at the outlet of the wrapped section (**Figure 6.8**).

**Table 6.3:** Maximum velocity values calculated for every geometrical configuration of the straight AA model; values are normalized to the max velocity value of the unwrapped straight model.

D (%)	Max v (norm)			
	L wrap (cm)			
	5	10	15	20
60	2.45	2.58	2.67	2.74
70	1.82	1.90	1.96	2.00
80	1.41	1.46	1.51	1.53
90	1.13	1.17	1.19	1.21

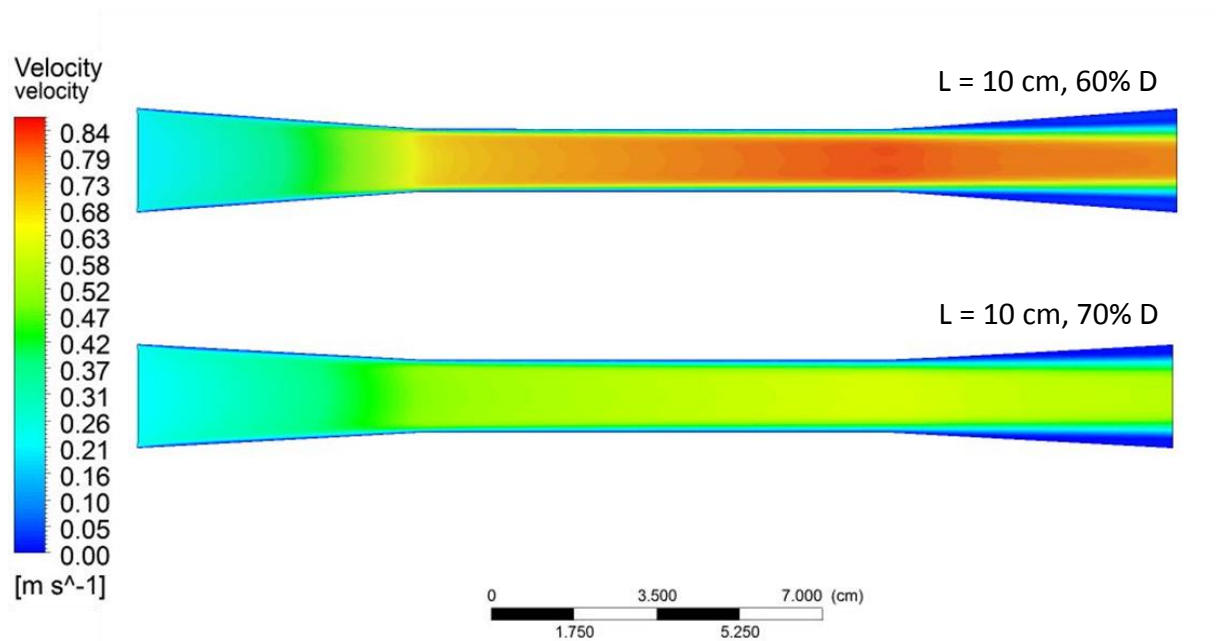


**Figure 6.8:** Velocity profiles (m/s) in two wrapped models. Inlets are on the left of the figure. Top: model characterized by 10 cm wrapping length and 60% D; bottom: model characterized by 10 cm wrapping length and 70% D. A small decrease in diameter from 70% to 60% of the UW diameter induced a marked peak velocity increase (almost 1.5 times).

Pressure drops ( $\Delta P$ ) along the model were calculated (**Table 6.4**): for every wrapped configuration, the pressure drop was increased, varying from 1.43 and 13.22 fold compared to the UW model configuration; once again, the maximum value was registered for the configuration with the largest diameter reduction (60% D) and the longest wrapping length (20 cm), and the largest step increase was observed for the transition between 70% D and 60% D for every wrapping length.

**Table 6.4:** Pressure drops calculated for every geometrical configuration of the straight AA model; values are normalized to the pressure drop value of the unwrapped straight model.

D (%)	P drops (norm)			
	L wrap (cm)			
	5	10	15	20
60	8.39	10.11	11.59	13.22
70	4.18	5.02	5.80	6.71
80	2.30	2.65	3.03	3.54
90	1.43	1.53	1.66	1.86

### 6.3.2 Realistic arch model

Velocity profiles were calculated for the UW model configuration and the 6 different wrapped configurations. As shown in **Figure 6.9** and **Figure 6.10**, different diameter reduction and wrap distance from the inlet influenced velocity patterns; as a consequence, the maximum values of velocity were located in different areas for each model. In particular, compared to the UW model every wrapped configuration had increased velocity in the AA section of the arch; this effect was higher for the models with the larger diameter reduction (60% D), and gradually decreased with increasing wrapping diameter.

As shown by the velocity profile figures (**Figure 6.9** and **6.10**), and further highlighted by the velocity streamlines in **Figure 6.11** and **Figure 6.12**, areas of low velocity and fluid recirculation appeared in the wrapped models; these were more evident for model configurations characterized by the biggest diameter reduction (60% D) and were predominantly located in the internal side of the descending section of the aortic arch. In particular, the model characterized by the smallest wrap diameter (60% D) and the longest wrapping length (model A) showed very evident vortices and flow separation in the area distal to the wrap, in the lower side of the arch.

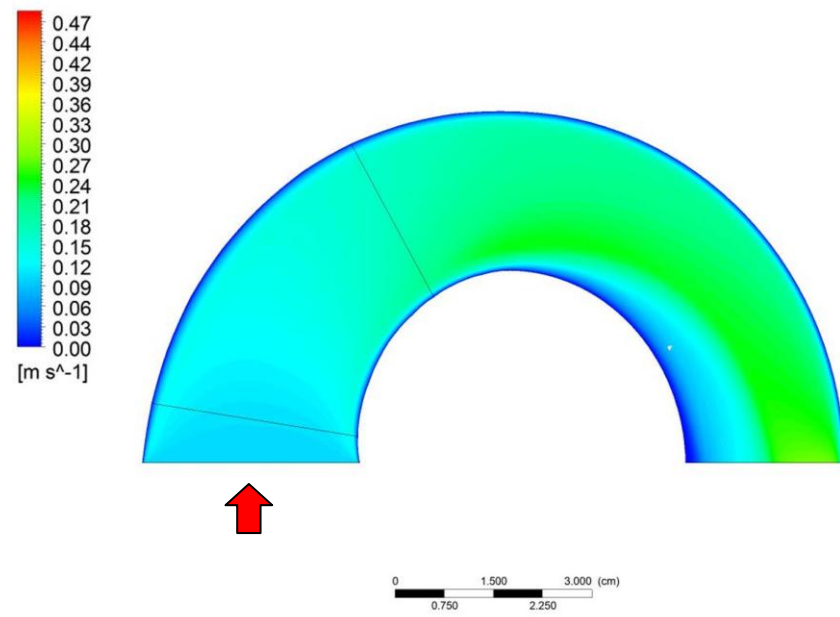


**Figure 6.9:** Velocity profiles (m/s) in the unwrapped model of the aortic arch. The red arrow indicates the inlet.

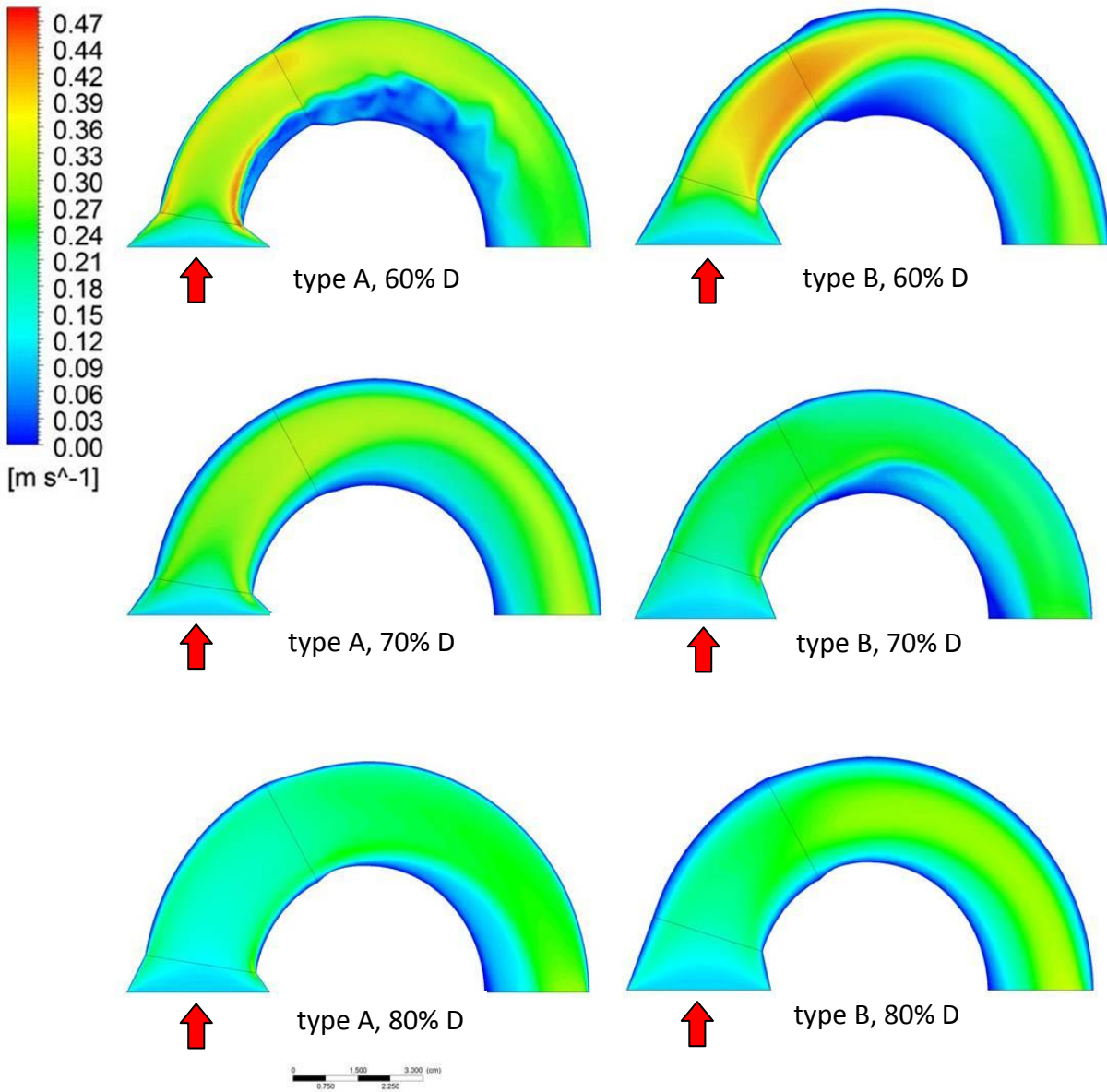


**Figure 6.10:** Velocity profiles (m/s) in the wrapped models of the aortic arch. Red arrows indicate the inlet. Left column: type A models, characterized by longer wrapping length and shorter distance from the inlet; right column: type B models, characterized by shorter wrapping length and larger distance from the inlet. Top row: wrapping diameter 60% of the UW one; middle row: wrapping diameter 70% of the UW one; bottom row: wrapping diameter 80% of the UW one. The combination of different wrapping lengths and diameters produced diverse flow patterns among the models. In every wrapped model the velocity in the AA tract was increased compared to the UW model. A 60% wrapping diameter combined with a short distance of the wrap from the inlet (top left panel) induced the creation of a wide area of flow recirculation immediately distal to the wrapped section of the arch.

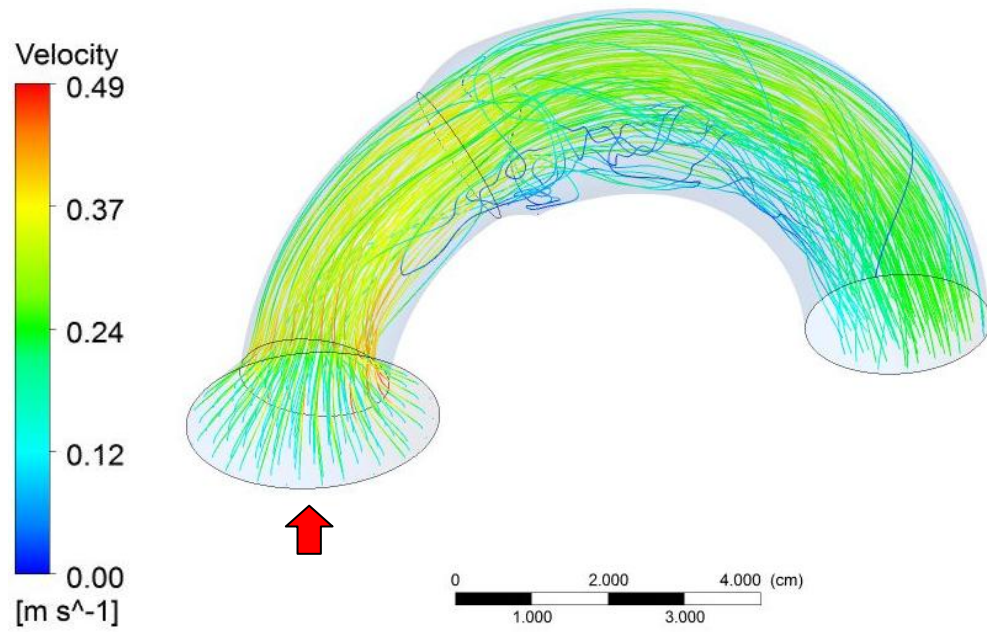


**Figure 6.11:** Velocity streamlines (m/s) in a wrapped model of the aortic arch: type A model with 60% D. This configuration shows the most irregular streamlines, with areas stagnating flow and flow separation distal to the wrap on the lower side of the arch. The red arrow indicates the inlet.

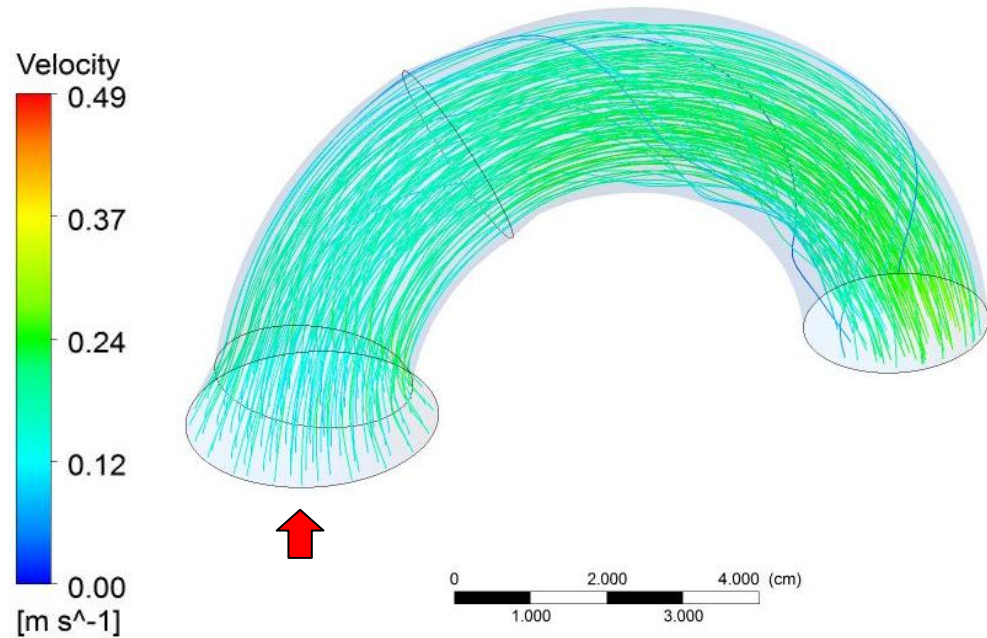


**Figure 6.12:** Velocity streamlines (m/s) in a wrapped model of the aortic arch: type A model with 80% D. This configuration shows the most regular streamlines with no areas of flow recirculation. The red arrow indicates the inlet.

Maximum velocity values are presented in **Table 6.5**, normalized to the UW model value: velocity is increased for every wrapped configuration compared to the UW one, but this augmentation is influenced by the complex combination of different wrapping lengths (corresponding to different distances from the inlet) and different diameter reductions; therefore, no simple pattern can be extracted to define the wrap influence on maximum velocity. For larger diameter reductions (60% and 70% D) the smaller wrapping length (model type B), which corresponded to a larger distance of the wrap from the inlet, produced a lower velocity increase compared to the larger wrapping length (model type A). For the smallest diameter reduction, instead, the two different wrapping lengths (model types A and B) had a similar effect on velocity increase. The largest increase was obtained for the smallest diameter reduction (60% D) and the longest wrapping length (model type A), where the maximum velocity value was 1.87 times the UW one.

**Table 6.5:** Maximum velocity values calculated for every geometrical configuration of the aortic arch model: absolute values in m/s (left) and relative values normalized to the max velocity value of the unwrapped model (right).

Max v (m/s)			Max v (norm)		
D (%)	L wrap		D (%)	L wrap	
	A	B		A	B
60	0.52	0.43	60	1.87	1.55
70	0.34	0.31	70	1.22	1.11
80	0.30	0.33	80	1.09	1.19

Pressure drops ( $\Delta P$ ), defined as the difference between the maximum and minimum values of pressure reached in the model, were calculated and presented in **Table 6.6**:  $\Delta P$  was increased for every wrapped configuration compared to the UW one. Moreover, a similar pattern to the one observed for maximum velocity was evident: the overall biggest  $\Delta P$  increase was reached for the model type A at the largest diameter reduction (60% D), and model B (characterized



by the shortest wrapping length) produced the smallest increase in  $\Delta P$  for large (60% D) and medium (70% D) diameter reductions.

**Table 6.6:** Pressure drops calculated for every geometrical configuration of the aortic arch model: absolute values in Pa (left) and relative values normalized to the pressure drop value of the unwrapped model (right).

$\Delta P$ (Pa)			$\Delta P$ (norm)		
D (%)	L wrap		D (%)	L wrap	
	A	B		A	B
60	323.31	297.11	60	6.46	5.94
70	415.77	100.11	70	8.31	2.00
80	101.64	184.27	80	2.03	3.68

Maximum wall shear stress was calculated for every model configuration and displayed in **Table 6.7:** after wrapping, maximum WSS was increased for every configuration, ranging from 2.84 to 26.54 times the UW value. No clear pattern was evident that could correlate the model type or diameter reduction to the WSS increase, thus indicating that the combination of different geometrical characteristics play a complex role in determining WSS in the wrapped models of the aortic arch.

**Table 6.7:** Maximum WSS values calculated for every geometrical configuration of the realistic arch model: absolute values in Pa (left) and relative values normalized to the maximum WSS value of the unwrapped model (right).

Max WSS (Pa)			Max WSS (norm)		
D (%)	L wrap		D (%)	L wrap	
	A	B		A	B
60	16.72	54.10	60	7.70	24.91
70	57.63	6.17	70	26.54	2.84
80	6.54	37.73	80	3.01	17.37

## 6.4 Discussion

The results of these simulations demonstrated that the AW caused increased peak velocity, increased WSS, and higher pressure drops for every combination of wrapping diameter and length, and for both model geometries – straight (similar to the descending thoracic aorta) and curved (mimicking the AA and the aortic arch). Curved models presented increased irregularities in the flow patterns: areas of low flow were produced by high diameter reduction configurations (60% D); in particular, model A, defined by a closer location of the wrap to the inlet, induced vortices and flow separation in the area of the arch immediately distal to the wrapped section.

When analysing the effects of the AW on a straight model of the aorta, a clear pattern was evident: the larger the diameter reduction and the longer the wrapping length, the larger was the impact of the AW on hemodynamic parameters. More specifically, for all three analysed parameters (max WSS, max velocity, and pressure drop), the values increased in a linear fashion with decreasing diameter from 90% D to 70% D, and then had a sharp step increase from 70% D to 60% D: this may indicate that a 70% wrapping diameter is the optimal compromise between wall unloading effectiveness, which increases with increasing diameter reduction, and minimization of negative hemodynamic effects associated with said diameter reduction.

In the analysis of the effects of wrapping on the realistic curved model of the aortic arch, the geometrical variations influenced the hemodynamic parameters in a more complex way, compared to the straight model analysis: the combination of diameter reduction, distance of the wrap from the inlet, and length of the wrap produced an irregular trend in the increase of the analysed hemodynamic parameters. Similarly to what was observed for the straight model, however, a 30% diameter reduction (70% D models) appeared to be the threshold below

which the negative effects of wrapping on flow velocity had a marked increase; in particular, areas of flow recirculation and separation were only visible for the 60%D model with longer wrapping length. This factor further indicates a 70% wrapping diameter as a potential choice for the optimization of the balance between positive and negative effects induced by aortic diameter reduction.

The models used present obvious limitations: the rigid arterial walls, the steady-state boundary condition, the idealised vessel geometry, and above all the lack of fluid-structure mechanical interaction determine a non-optimal accuracy of the model in describing the 3D fluid dynamic behaviour of a wrapped aortic segment. Further studies are suggested to develop the modelling framework described in this chapter and overcome current limitations. Firstly, imaging data could be used to obtain accurate patient-specific 3D models of unwrapped and (simulated or real) wrapped aortic geometries, similarly to what has been done in recent CFD investigations. In a recent study by Anzani et al. on the fluid dynamics of restenosed aortic coarctation, patient-specific AA geometry and aortic blood flow boundary conditions were obtained from magnetic resonance angiography (MRA) data and 2D phase-contrast magnetic resonance imaging (PC MRI) respectively, allowing for CFD simulation of blood flow in the AA tract affected by stenosis and ultimately predicting the effect of aortic coarctation on flow turbulence in the AA (Arzani et al. 2012). Similarly, LaDisa et al. used patient-specific image-derived geometrical models to perform CFD simulations of blood flow in patients affected by thoracic aortic coarctation which was surgically resected with end-to-end anastomosis, in order to predict and localise flow disturbances and abnormal values of WSS due to irregular aortic geometry (LaDisa et al. 2011). Another very informative study was performed by Auricchio et al. on the effects of endovascular stent repair of aortic disease on local flow and WSS pattern changes using advanced computed tomography and MRI for the creation of patient-specific geometries (Auricchio et al. 2014). Moreover, future

computational investigations of the AW should include fluid-structure interaction analyses to account for coupling between hemodynamics and wall mechanics and quantify the effect of AW on wall tension (Crosetto et al. 2011).

In conclusion, the hemodynamic changes determined by the AW – increased peak velocity, increased WSS, flow recirculation and separation – may have a negative impact on the physiology of the aortic wall, but cannot be avoided, as they are inherent in the diameter reduction necessary for aortic wall unloading. It is therefore crucial to consider the impact of the AW on hemodynamics of the aorta and to aim at minimizing the potential detrimental effects for clinical applications of the AW. The simulations performed in these studies suggest that diameter reductions above 30% (70% D) should be avoided to prevent increasingly detrimental effects on the hemodynamics of the aorta.

# Chapter 7

## *Conclusions*

The Aortic Wrap's conceptual working mechanism, aimed at increasing aortic distensibility and reducing pulse pressure, was investigated throughout this thesis by means of different computational and experimental methodologies. Every study clearly indicated that the AW works through aortic wall unloading and increases distensibility of the wrapped aortic segment, thus decreasing aortic input impedance and reducing pulse pressure. The following conclusions were achieved in relation to each specific study:

- (i) The study on the computational multibranched model of the arterial tree demonstrated that aortic PP can be reduced by 8% when decreasing functional stiffness by 80% in the AA, which is able to compensate for the rise of PP determined by increased resistance associated with a 20% AA diameter reduction. This study highlighted the necessity of achieving high values of distensibility in the AA in order to obtain clinically significant PP reduction effects.

- (ii) The *in vitro* study on synthetic models of the aorta proved the efficacy of the AW concept in increasing vessel compliance: it demonstrated that external wall unloading of a stiff vessel by a means of diameter reduction by a highly distensible wrap is an effective mechanism of stiffness reduction. The results of the study showed that distensibility of a stiff model of the aorta could be increased 4.5 times with a 20% diameter reduction for working pressures in the 50 – 200 mmHg range, therefore virtually restoring distensibility values typical of young subjects (40-49 year old) in a model with an intrinsic distensibility matching elderly subjects (> 70 year old). The magnitude of these results is in line with what is described by the computational multibranched study: the 80% reduction in stiffness proposed by the computational simulation translates into a 5 fold increase in distensibility (distensibility being the inverse of E), which is nearly achieved by the 4.5 fold distensibility increase observed in the experimental study.
- (iii) The experimental study performed on a bench-top distributed silicon model of the arterial circulation investigated the effects of elastic wrapping on central PP and demonstrated that PP (and consequently systolic pressure) could be reduced when the AA diameter was decreased with the same elastic distensible wrap used for the *in vitro* distensibility study; in particular, when a 20% D reduction was applied, PP in the AA was decreased by 8 % for an intermediate heart rate of 60 bpm and an intermediate stroke volume of 60 ml. Once again, these findings fit with the results obtained by the computational multibranched model: the 8% PP reduction proposed by the computational model was achieved or even exceeded by most of the experimental model configurations (i.e. different combinations of stroke volume

and heart rate). It is important to note that an 8% reduction in pulse pressure of a subject with isolated systolic hypertension (eg. systolic pressure of 160 mmHg and diastolic pressure of 90 mmHg) would equate to approximately 6 mmHg in systolic pressure. If this decrease in systolic pressure were to be maintained over prolonged periods it would translate to a 22% reduction in risk of stroke (Staessen et al. 1999).

- (iv) The Aortic Wrap, proven to be effective on increasing distensibility and decreasing PP in the thoracic aorta, bases its functional effectiveness in aortic diameter reduction: this feature, although necessary for wall unloading, induces hemodynamic changes in the wrapped section and the neighbouring areas of the aorta. To address this point, the effects of AW-associated diameter reduction on aortic hemodynamics were investigated via CFD simulations on 3D computational models of the aorta and the aortic arch. The results of this study indicated that peak flow velocity, WSS, and pressure drop were increased after wrapping and suggested that a 30% diameter reduction should not be exceeded in order to avoid areas of flow recirculation and minimize negative hemodynamic effects. However, as demonstrated by the computational multibranched simulation and the experimental studies, a 20% diameter reduction, well below the 30% threshold, is sufficient to produce substantial results in terms of increased distensibility and decreased pulse pressure.

This thesis demonstrated that the AW is a valid and highly effective method to reduce pulse pressure in old stiffened aortas, typical of patients affected by isolated systolic hypertension. The Aortic Wrap, thus, is presented as a potential non-pharmacological therapeutic treatment for resistant ISH and congestive heart failure. Future studies on large animal models are required to assess acute and long term effects of wrapping on central blood pressure and

aortic wall physiology; moreover, 3D computational simulations which account for fluid-structure interaction phenomena are needed to model the effects of AW on wall stresses and better characterize the hemodynamic effects of diameter reduction.



# *Appendix*

## **A. Limitations of the multibranched computational model described in Chapter 3:**

The model is based on assumptions which reduce complexity and computing power required, but which inevitably determine its limitations: the 3D nature of blood flow was not considered; the geometrical and biomechanical characteristics and of the arterial system were simplified, by limiting the number of branches, not representing arterioles with diameter  $< 2\text{mm}$ , and considering arteries as cylindrical vessel with uniform section; moreover, the purely resistive terminations of the arterial tree branches constitutes a simplified and linearised boundary condition which can introduce inaccuracies. These assumptions limited the accuracy of the model in describing the fluid dynamics of the system; moreover, the structural effects of the AW on the arterial walls could not be explored with this purely hemodynamic approach. However, the model used has proved effective in indicating the effects on aortic PP determined by an increase in stiffness and a decrease in diameter in the AA, thus being informative on AW-induced effects on PP in the aorta.

**B. Comparison between the original multibranched model developed by Avolio (1980) and the current modified version of the model (described in Chapter 3):**

**Table B:** The table highlights the structural differences between the original model (Avolio 1980) and the current model.

	<i>Avolio (1980)</i>	<i>Current model</i>
<b>N. of nodes</b>	68	76
<b>N. of segments</b>	128	136
<b>N. of aortic segments</b>	10	18
<b>Aortic radius</b>	fixed	variable
<b>Aortic stiffness (Young's modulus)</b>	fixed	variable

**C. Overview of the *in vitro* investigation of the Aortic Wrap effects on distensibility using rigid cylindrical aortic models (described in Chapter 4):**

**Table C:** The table presents an overview of the experimental design and critical pressure results obtained in Chapter 4.

<i>Experiment number:</i>	<i>A</i>	<i>B</i>	<i>C</i>
<b>Type of aortic model</b>	silicon tube	silicon tube	fabric model
<b>Type of Aortic Wrap</b>	7 rubber rings	1, 2 or 3 rectangular rubber wraps	3 rectangular rubber wraps
<b>Initial diameter (D) reduction</b>	33%	20% and 30%	20%
<b>Critical Pressure [mmHg]</b>	~50	~70 (20% D reduction) and ~115 (30% D reduction)	~200

# References

- Alastruey, J, A W Khir, K S Matthys, P Segers, S J Sherwin, P R Verdonck, K H Parker, and J Peiró. 2011. "Pulse Wave Propagation in a Model Human Arterial Network: Assessment of 1-D Visco-Elastic Simulations against in Vitro Measurements." *Journal of Biomechanics* 44 (12) (August 11): 2250–8.
- Armentano, R L, J Levenson, J G Barra, E I Fischer, G J Breitbart, R H Pichel, and A Simon. 1991. "Assessment of Elastin and Collagen Contribution to Aortic Elasticity in Conscious Dogs." *Am J Physiol Heart Circ Physiol* 260 (6) (June 1): H1870–1877.
- Arzani, A, P Dyverfeldt, T Ebberts, and S C Shadden. 2012. "In Vivo Validation of Numerical Prediction for Turbulence Intensity in an Aortic Coarctation." *Annals of Biomedical Engineering* 40 (4) (April): 860–70.
- Auricchio, F, M Conti, A Lefieux, S Morganti, A Reali, F Sardanelli, F Secchi, S Trimarchi, and A Veneziani. 2014. "Patient-Specific Analysis of Post-Operative Aortic Hemodynamics: A Focus on Thoracic Endovascular Repair (TEVAR)." *Computational Mechanics* (January 24).
- Avolio, A 1980. "Multi-Branched Model of the Human Arterial System." *Medical and Biological Engineering and Computing* 18 (6): 709–718.
- Avolio, A P, S G Chen, R P Wang, C L Zhang, M F Li, and M F O'Rourke. 1983. "Effects of Aging on Changing Arterial Compliance and Left Ventricular Load in a Northern Chinese Urban Community." *Circulation* 68 (1): 50–58.
- Avolio, A, M Butlin, Y Liu, K Viegas, B Avadhanam, and G Lindesay. 2011. "Regulation of Arterial Stiffness: Cellular, Molecular and Neurogenic Mechanisms." *Artery Research* 5 (4) (December): 122–127.
- Bateman, G 2002. "Pulse-Wave Encephalopathy: A Comparative Study of the Hydrodynamics of Leukoaraisosis and Normal-Pressure Hydrocephalus." *Neuroradiology* 44 (9): 740–748.
- Beckett, N S, R Peters, A E Fletcher, J A Staessen, L Liu, D Dumitrascu, V Stoyanovsky, et al. 2008. "Treatment of Hypertension in Patients 80 Years of Age or Older." *New England Journal of Medicine* 358 (18) (May 1): 1887–1898.

- Boutouyrie, P, S Laurent, A Benetos, X Girerd, A Hoeks, and M Safar. 1992. "Opposing Effects of Ageing on Distal and Proximal Large Arteries in Hypertensives." *Journal of Hypertension* 10: S87–S92.
- Bramwell, J C, and A V Hill. 1922a. "The Velocity of the Pulse Wave in Man." *Proceedings of the Royal Society of London. Series B, Containing Papers of a Biological Character* 93 (652): 298–306.
- . 1922b. "Velocity of Transmission of the Pulse-Wave." *The Lancet* 199 (5149): 891–892.
- Braunwald, E 1969. "Thirteenth Bowditch Lecture. The Determinants of Myocardial Oxygen Consumption." *The Physiologist* 12 (2): 65–93.
- Cavalcante, J L, J A C Lima, A Redheuil, and M H Al-Mallah. 2011. "Aortic Stiffness: Current Understanding and Future Directions." *Journal of the American College of Cardiology* 57 (14): 1511–1522.
- Cecelja, M, and P Chowienczyk. 2012. "Role of Arterial Stiffness in Cardiovascular Disease." *JRSM Cardiovascular Disease* 1 (4).
- Chobanian, A V, G L Bakris, H R Black, W C Cushman, L A Green, J L Izzo, D W Jones, et al. 2003. "Seventh Report of the Joint National Committee on Prevention, Detection, Evaluation, and Treatment of High Blood Pressure." *Hypertension* 42 (6 ) (December 1): 1206–1252.
- Crosetto, P, P Reymond, S Deparis, D Kontaxakis, N Stergiopoulos, and A Quarteroni. 2011. "Fluid-Structure Interaction Simulation of Aortic Blood Flow." *Computers & Fluids* 43 (1): 46–57.
- Dart, A M, F Lacombe, J K Yeoh, J D Cameron, G L Jennings, E Laufer, and D S Esmore. 1991. "Aortic Distensibility in Patients with Isolated Hypercholesterolaemia, Coronary Artery Disease, or Cardiac Transplant." *The Lancet* 338 (8762): 270–273.
- Dufouil, C, J Chalmers, O Coskun, V Besancon, M Bousser, P Guillon, S MacMahon, et al. 2005. "Effects of Blood Pressure Lowering on Cerebral White Matter Hyperintensities in Patients With Stroke: The PROGRESS (Perindopril Protection Against Recurrent Stroke Study) Magnetic Resonance Imaging Substudy." *Circulation* 112 (11): 1644–1650.
- Dzau, V J, E M Antman, H R Black, D L Hayes, J E Manson, J Plutzky, J J Popma, and W Stevenson. 2006a. "The Cardiovascular Disease Continuum Validated: Clinical Evidence of Improved Patient Outcomes: Part II: Clinical Trial Evidence (Acute Coronary Syndromes Through Renal Disease) and Future Directions." *Circulation* 114 (25): 2871–2891.
- . 2006b. "The Cardiovascular Disease Continuum Validated: Clinical Evidence of Improved Patient Outcomes: Part I: Pathophysiology and Clinical Trial Evidence (Risk Factors Through Stable Coronary Artery Disease)." *Circulation* 114 (25): 2850–2870.
- Franklin, S S. 2012. "Elderly Hypertensives: How Are They Different?" *The Journal of Clinical Hypertension* 14 (11): 779–786.

- Franklin, S S, W Gustin, N D Wong, M G Larson, M A Weber, W B Kannel, and D Levy. 1997. "Hemodynamic Patterns of Age-Related Changes in Blood Pressure: The Framingham Heart Study." *Circulation* 96 (1): 308–315.
- Franklin, S S, M J Jacobs, N D Wong, G J L'Italien, and P Lapuerta. 2001. "Predominance of Isolated Systolic Hypertension Among Middle-Aged and Elderly US Hypertensives: Analysis Based on National Health and Nutrition Examination Survey (NHANES) III." *Hypertension* 37 (3): 869–874.
- Giudici, F, Y Qian, M O'Rourke, and A Avolio. 2012. "Simulation of Reduction of Proximal Aortic Stiffness by an Elastic Wrap and Effects on Pulse Pressure." In *Engineering in Medicine and Biology Society (EMBC), 2012 Annual International Conference of the IEEE*, 2012:657–660.
- Hall, J E, and A C Guyton. 2011. *Textbook of Medical Physiology*. Saunders.
- Hayward, C S, W S Peters, A F Merry, P N Ruygrok, P Jansz, G O'Driscoll, R I Larbalestier, et al. 2010. "Chronic Extra-Aortic Balloon Counterpulsation: First-in-Human Pilot Study in End-Stage Heart Failure." *The Journal of Heart and Lung Transplantation* 29 (12) (December): 1427–1432.
- Henry Feugeas, M C, G De Marco, I I Peretti, S Godon-Hardy, D Fredy, and E Schouman Claeys. 2005. "Age-Related Cerebral White Matter Changes and Pulse-Wave Encephalopathy: Observations with Three-Dimensional MRI." *Magnetic Resonance Imaging* 23 (9): 929–937.
- Hickson, S S, M Butlin, M Graves, V Taviani, A P Avolio, C M McEniery, and I B Wilkinson. 2010. "The Relationship of Age With Regional Aortic Stiffness and Diameter." *JACC: Cardiovascular Imaging* 3 (12): 1247–1255.
- Hirata, K, T Yaginuma, M F O'Rourke, and M Kawakami. 2006. "Age-Related Changes in Carotid Artery Flow and Pressure Pulses: Possible Implications for Cerebral Microvascular Disease." *Stroke* 37 (10): 2552–2556.
- Iliopoulos, J. 2006. "The Aortic Wrap Procedure: A Surgical Method of Treating Age Related Aortic Dilatation and Stiffness, Ph.D. Thesis". Sydney, NSW: University of New South Wales.
- Ioannou, C V, D R Morel, A N Katsamouris, S Katranitsa, I Startchik, A Kalangos, N Westerhof, and N Stergiopulos. 2009. "Left Ventricular Hypertrophy Induced by Reduced Aortic Compliance." *Journal of Vascular Research* 46 (5): 417–425.
- Ioannou, C V, N Stergiopulos, A N Katsamouris, I Startchik, A Kalangos, M J Licker, N Westerhof, and D R Morel. 2003. "Hemodynamics Induced after Acute Reduction of Proximal Thoracic Aorta Compliance." *European Journal of Vascular and Endovascular Surgery* 26 (2): 195–204.
- Jung, S M, S Jandu, J Stepan, A Belkin, S S An, A Pak, E Y Choi, et al. 2013. "Increased Tissue Transglutaminase Activity Contributes to Central Vascular Stiffness in eNOS Knockout Mice." *American Journal of Physiology. Heart and Circulatory Physiology* 305 (6) (September 15): H803–10.

- Kahle, W, H Leonhardt, and W Platzer. 1992. *Color Atlas and Textbook of Human Anatomy: Locomotor System*. Vol. 1. G. Thieme Verlag.
- Karamanoglu, M, D E Gallagher, A P Avolio, and M F O'Rourke. 1994. "Functional Origin of Reflected Pressure Waves in a Multibranched Model of the Human Arterial System." *American Journal of Physiology - Heart and Circulatory Physiology* 267 (5): H1681–H1688.
- Kass, D A, E P Shapiro, M Kawaguchi, A R Capriotti, A Scuteri, R C deGroof, and E G Lakatta. 2001. "Improved Arterial Compliance by a Novel Advanced Glycation End-Product Crosslink Breaker." *Circulation* 104 (13): 1464–1470.
- Katz, A M. 1994. "The Cardiomyopathy of Overload: An Unnatural Growth Response in the Hypertrophied Heart." *Annals of Internal Medicine* 121 (5) (September 1): 363.
- Kelly, R P, R Tunin, and D A Kass. 1992. "Effect of Reduced Aortic Compliance on Cardiac Efficiency and Contractile Function of in Situ Canine Left Ventricle." *Circulation Research* 71 (3): 490–502.
- Kostis, J B, B R Davis, J Cutler, and et al. 1997. "Prevention of Heart Failure by Antihypertensive Drug Treatment in Older Persons with Isolated Systolic Hypertension." *JAMA* 278 (3): 212–216.
- Kostis, J B, J Lawrence-Nelson, R Ranjan, A C Wilson, W J Kostis, and C R Lacy. 2001. "Association of Increased Pulse Pressure with the Development of Heart Failure in Shep." *American Journal of Hypertension* 14 (8): 798–803.
- LaDisa, J F, R J Dholakia, C A Figueroa, I E Vignon-Clementel, F P Chan, M M Samyn, J R Cava, C A Taylor, and J A Feinstein. 2011. "Computational Simulations Demonstrate Altered Wall Shear Stress in Aortic Coarctation Patients Treated by Resection with End-to-End Anastomosis." *Congenital Heart Disease* 6 (5): 432–43.
- Lakatta, E G, and D Levy. 2003a. "Arterial and Cardiac Aging: Major Shareholders in Cardiovascular Disease Enterprises: Part I: Aging Arteries: A 'Set Up' for Vascular Disease." *Circulation* 107 (1): 139–146.
- . 2003b. "Arterial and Cardiac Aging: Major Shareholders in Cardiovascular Disease Enterprises: Part II: The Aging Heart in Health: Links to Heart Disease." *Circulation* 107 (2): 346–354.
- Länne, T, H Stale, H Bengtsson, D Gustafsson, D Bergqvist, B Sonesson, H Lecerof, and P Dahl. 1992. "Noninvasive Measurement of Diameter Changes in the Distal Abdominal Aorta in Man." *Ultrasound in Medicine & Biology* 18 (5): 451–457.
- Lanne, T, Fl Hansen, P Mangell, and B Sonesson. 1994. "Differences in Mechanical Properties of the Common Carotid Artery and Abdominal Aorta in Healthy Males." *Journal of Vascular Surgery* 20 (2): 218–225.
- Latson, T W, W C Hunter, N Katoh, and K Sagawa. 1988. "Effect of Nitroglycerin on Aortic Impedance, Diameter, and Pulse-Wave Velocity." *Circulation Research* 62 (5): 884–890.

- Laurent, S, J Cockcroft, L Van Bortel, P Boutouyrie, C Giannattasio, D Hayoz, B Pannier, C Vlachopoulos, I Wilkinson, and H Struijker-Boudier. 2006. "Expert Consensus Document on Arterial Stiffness: Methodological Issues and Clinical Applications." *European Heart Journal* 27 (21): 2588–2605.
- Learoyd, B M, and M G Taylor. 1966. "Alterations with Age in the Viscoelastic Properties of Human Arterial Walls." *Circulation Research* 18 (3): 278–292.
- Legget, M E, W S Peters, F P Milsom, J S Clark, T M West, R L French, and A F Merry. 2005. "Extra-Aortic Balloon Counterpulsation: An Intraoperative Feasibility Study ." *Circulation* 112 (9 suppl ) (August 30): I–26–I–31.
- London, G M, R G Asmar, M F O'Rourke, and M E Safar. 2004. "Mechanism(s) of Selective Systolic Blood Pressure Reduction after a Low-Dose Combination of perindopril/Indapamide in Hypertensive Subjects: Comparison with Atenolol." *Journal of the American College of Cardiology* 43 (1) (January): 92–99.
- Matthys, K S, J Alastruey, J Peiro, A W Khir, P Segers, P R Verdonck, K H Parker, and S J Sherwin. 2007. "Pulse Wave Propagation in a Model Human Arterial Network: Assessment of 1-D Numerical Simulations against in Vitro Measurements." *Journal of Biomechanics* 40 (15): 3476–3486.
- McEniery, C M. 2006. "Novel Therapeutic Strategies for Reducing Arterial Stiffness." *British Journal of Pharmacology* 148 (7): 881–883.
- McEniery, C M, I B Wilkinson, and A P Avolio. 2007. "Age, Hypertension and Arterial Function." *Clinical and Experimental Pharmacology and Physiology* 34 (7): 665–671.
- McEniery, C M, Yasmin, I R Hall, A Qasem, I B Wilkinson, and J R Cockcroft. 2005. "Normal Vascular Aging: Differential Effects on Wave Reflection and Aortic Pulse Wave Velocity: The Anglo-Cardiff Collaborative Trial (ACCT)." *Journal of the American College of Cardiology* 46 (9): 1753–1760.
- Milnor, W R. 1989. "Hemodynamics." *Williams and Wilkins, Baltimore*.
- Mitchell, G F, S Hwang, R S Vasan, M G Larson, M J Pencina, N M Hamburg, J A Vita, D Levy, and E J Benjamin. 2010. "Arterial Stiffness and Cardiovascular Events: The Framingham Heart Study." *Circulation* 121 (4): 505–511.
- Mitnovetski, S, A A Almeida, A Barr, W S Peters, F P Milsom, B Ho, and J A Smith. 2008. "Extra-Aortic Implantable Counterpulsation Pump in Chronic Heart Failure." *The Annals of Thoracic Surgery* 85 (6) (June): 2122–2125.
- Moulopoulos, S D, S Topaz, and W J Kolff. 1962. "Diastolic Balloon Pumping (with Carbon Dioxide) in the aorta—A Mechanical Assistance to the Failing Circulation." *American Heart Journal* 63 (5) (May): 669–675.
- Najjar, S S, A Scuteri, and E G Lakatta. 2005. "Arterial Aging: Is It an Immutable Cardiovascular Risk Factor?" *Hypertension* 46 (3): 454–462.
- Nichols, W W, C R Conti, W E Walker, and W R Milnor. 1977. "Input Impedance of the Systemic Circulation in Man." *Circulation Research* 40 (5) (May 1): 451–458.

- Nichols, W W, M F O'Rourke, C Vlachopoulos, and P D Arnold P. Hoeks. 2011. *McDonald's Blood Flow in Arteries: Theoretical, Experimental and Clinical Principles*. 6th ed. Hodder Arnold Publishers.
- Nichols, W W, and D G Edwards. 2001. "Arterial Elastance and Wave Reflection Augmentation of Systolic Blood Pressure: Deleterious Effects and Implications for Therapy." *Journal of Cardiovascular Pharmacology and Therapeutics* 6 (1): 5–21.
- Nichols, W W, M F O'Rourke, A P Avolio, T Yaginuma, J P Murgo, C J Pepine, and C R Conti. 1985. "Effects of Age on Ventricular-Vascular Coupling." *The American Journal of Cardiology* 55 (9): 1179–1184.
- Nichols, W W, M F O'Rourke, A P Avolio, T Yaginuma, J P Murgo, C J Pepine, and C R Conti. 1987. "Age-Related Changes in Left Ventricular/Arterial Coupling." In *Ventricular/Vascular Coupling SE - 4*, edited by Frank C.P. Yin, 79–114. Springer New York.
- Noordergraaf, A. 1978. *Circulatory System Dynamics 1978*. New York: Academic Press. Elsevier.
- O'Rourke, M F. 1967. "Steady and Pulsatile Energy Losses in the Systemic Circulation under Normal Conditions and in Simulated Arterial Disease." *Cardiovascular Research* 1 (4): 313–326.
- O'Rourke, M F, A P Avolio, P D Lauren, and J Yong. 1987. "Age-Related Changes of Elastin Lamellae in the Human Thoracic Aorta." *Journal of the American College of Cardiology* 9: 53A.
- O'Rourke, M F, and M G Taylor. 1967. "Input Impedance of the Systemic Circulation." *Circulation Research* 20 (4): 365–380.
- O'Rourke, M F. 1965. "Pressure and Flow in Arteries, MD Thesis". University of Sydney.
- . 1976. "Pulsatile Arterial Haemodynamics in Hypertension." *Australian and New Zealand Journal of Medicine* 6 (4): 40–48.
- O'Rourke, M F, and J Hashimoto. 2007. "Mechanical Factors in Arterial Aging: A Clinical Perspective." *Journal of the American College of Cardiology* 50 (1): 1–13.
- O'Rourke, M F, and W W Nichols. 2005. "Aortic Diameter, Aortic Stiffness, and Wave Reflection Increase With Age and Isolated Systolic Hypertension." *Hypertension* 45 (4): 652–658.
- O'Rourke, M F, and M E Safar. 2005. "Relationship Between Aortic Stiffening and Microvascular Disease in Brain and Kidney: Cause and Logic of Therapy." *Hypertension* 46 (1): 200–204. doi:10.1161/01.hyp.0000168052.00426.65.
- O'Rourke, M F, M E Safar, and V Dzau. 2010. "The Cardiovascular Continuum Extended: Aging Effects on the Aorta and Microvasculature." *Vascular Medicine* 15 (6): 461–468.



- Okamoto, R, J Wagenseil, W DeLong, S Peterson, N Kouchoukos, and T Sundt. 2002. "Mechanical Properties of Dilated Human Ascending Aorta." *Annals of Biomedical Engineering* 30 (5): 624–635.
- Pannier, B M, A P Avolio, A Hoeks, G Mancina, and K Takazawa. 2002. "Methods and Devices for Measuring Arterial Compliance in Humans." *American Journal of Hypertension* 15 (8): 743–753.
- Perry, H Jr, B R Davis, T R Price, and et al. 2000. "Effect of Treating Isolated Systolic Hypertension on the Risk of Developing Various Types and Subtypes of Stroke: The Systolic Hypertension in the Elderly Program (shep)." *JAMA* 284 (4): 465–471.
- Redheuil, A, W Yu, E Mousseaux, A A Harouni, N Kachenoura, C O Wu, D Bluemke, and J A C Lima. 2011. "Age-Related Changes in Aortic Arch Geometry: Relationship With Proximal Aortic Function and Left Ventricular Mass and Remodeling." *Journal of the American College of Cardiology* 58 (12): 1262–1270.
- Redheuil, A, W Yu, C O Wu, E Mousseaux, A de Cesare, R Yan, N Kachenoura, D Bluemke, and J A C Lima. 2010. "Reduced Ascending Aortic Strain and Distensibility." *Hypertension* 55 (2): 319–326.
- Rutan, G H, L H Kuller, J D Neaton, D N Wentworth, R H McDonald, and W M Smith. 1988. "Mortality Associated with Diastolic Hypertension and Isolated Systolic Hypertension among Men Screened for the Multiple Risk Factor Intervention Trial." *Circulation* 77 (3 ) (March 1): 504–514.
- Safar, M E. 2007. "Mechanism(s) of Systolic Blood Pressure Reduction and Drug Therapy in Hypertension." *Hypertension* 50 (1): 167–171.
- Safar, M E, T Nawar, and G E Plante. 2007. "Large Arteries and the Kidney." *Journal of the American Society of Hypertension* 1 (3): 169–177.
- Schmid-Schönbein, H, and R E Wells Jr. 1971. "Rheological Properties of Human Erythrocytes and Their Influence upon the 'Anomalous' Viscosity of Blood." In *Ergebnisse Der Physiologie Reviews of Physiology, Volume 63 SE - 4*, 63:146–219. Springer Berlin Heidelberg.
- Schmitt, M, A Avolio, A Qasem, C M McEniery, M Butlin, I B Wilkinson, and J R Cockcroft. 2005. "Basal NO Locally Modulates Human Iliac Artery Function In Vivo." *Hypertension* 46 (1): 227–231.
- Segers, P, F Dubois, D De Wachter, and P Verdonck. 1998. "Role and Relevancy of a Cardiovascular Simulator." *Cardiovascular Engineering* 3 (1): 48–56.
- Segers, P, and P Verdonck. 2000. "Role of Tapering in Aortic Wave Reflection: Hydraulic and Mathematical Model Study." *Journal of Biomechanics* 33 (3): 299–306.
- SHEP. 1991. "Prevention of Stroke by Antihypertensive Drug Treatment in Older Persons with Isolated Systolic Hypertension: Final Results of the Systolic Hypertension in the Elderly Program (shep)." *JAMA* 265 (24): 3255–3264.

- Smulyan, H, R G Asmar, A Rudnicki, G M London, and M E Safar. 2001. "Comparative Effects of Aging in Men and Women on the Properties of the Arterial Tree." *Journal of the American College of Cardiology* 37 (5): 1374–1380.
- Sonesson, B, F Hansen, H Stale, and T Lanne. 1993. "Compliance and Diameter in the Human Abdominal aorta—The Influence of Age and Sex." *European Journal of Vascular Surgery* 7 (6): 690–697.
- Staessen, J, JG Wang, L Thijs, and R Fagard. 1999. "Overview of the Outcome Trials in Older Patients with Isolated Systolic Hypertension." *Journal of Human Hypertension* 13 (12): 859.
- Sugawara, J, K Hayashi, T Yokoi, and H Tanaka. 2008. "Age-Associated Elongation of the Ascending Aorta in Adults." *JACC: Cardiovascular Imaging* 1 (6): 739–748.
- Taylor, M G. 1964. "Wave Travel in Arteries and the Design of the Cardiovascular System." *Pulsatile Blood Flow*: 343–372.
- . 1965. "Wave-Travel in a Non-Uniform Transmission Line, in Relation to Pulses in Arteries." *Phys Med Biol* 10 ((4)): 539–550.
- . 1966a. "Wave Transmission through an Assembly of Randomly Branching Elastic Tubes." *Biophysical Journal* 6 (6): 697–716.
- . 1966b. "The Input Impedance of an Assembly of Randomly Branching Elastic Tubes." *Biophysical Journal* 6 (1): 29–51.
- . 1967. "The Influence of the Viscous Properties of Blood and the Arterial Wall upon the Input Impedance of the Arterial System." *Biorheology* 4 (3): 143–147.
- . 1969. "The Optimum Elastic Properties of Arteries." In *Ciba Foundation Symposium - Circulatory and Respiratory Mass Transport*, 136–152. John Wiley & Sons, Ltd.
- . 1973. *Hemodynamics*. Comroe, Julius H. Jr.
- Vaitkevicius, P V, M Lane, H Spurgeon, D K Ingram, G S Roth, J J Egan, S Vasan, et al. 2001. "A Cross-Link Breaker Has Sustained Effects on Arterial and Ventricular Properties in Older Rhesus Monkeys." *Proceedings of the National Academy of Sciences* 98 (3): 1171–1175.
- Virmani, R, A P Avolio, W J Mergner, M Robinowitz, E E Herderick, J F Cornhill, S Y Guo, T H Liu, D Y Ou, and M O'Rourke. 1991. "Effect of Aging on Aortic Morphology in Populations with High and Low Prevalence of Hypertension and Atherosclerosis. Comparison between Occidental and Chinese Communities." *The American Journal of Pathology* 139 (5): 1119–1129.
- Vlachopoulos, C, K Aznaouridis, and C Stefanadis. 2006. "Clinical Appraisal of Arterial Stiffness: The Argonauts in Front of the Golden Fleece." *Heart* 92 (11): 1544–1550.
- Vlachopoulos, C, K Aznaouridis, and C Stefanadis. 2010. "Prediction of Cardiovascular Events and All-Cause Mortality With Arterial Stiffness: A Systematic Review and Meta-Analysis." *Journal of the American College of Cardiology* 55 (13): 1318–1327.

- Wagenseil, J E, and R P Mecham. 2012. "Elastin in Large Artery Stiffness and Hypertension." *Journal of Cardiovascular Translational Research* 5 (3): 264–273.
- Westerhof, N, F Bosman, C J De Vries, and A Noordergraaf. 1969. "Analog Studies of the Human Systemic Arterial Tree." *Journal of Biomechanics* 2 (2): 121–143.
- Wolffenbittel, B H R, C M Boulanger, F R L Crijns, M S P Huijberts, P Poitevin, G N M Swennen, S Vasan, et al. 1998. "Breakers of Advanced Glycation End Products Restore Large Artery Properties in Experimental Diabetes." *Proceedings of the National Academy of Sciences* 95 (8): 4630–4634.
- Womersley, J R. 1955. "Method for the Calculation of Velocity, Rate of Flow and Viscous Drag in Arteries When the Pressure Gradient Is Known." *The Journal of Physiology* 127 (3 ) (March 28): 553–563.
- . 1957. "Oscillatory Flow in Arteries: The Constrained Elastic Tube as a Model of Arterial Flow and Pulse." *Physics in Medicine and Biology* 2 (2).
- Yu, S Y, and H T Blumenthal. 1965. "The Calcification of Elastic Fiber: Part 4. Epinephrine and Beta-Aminopropionitrile-Induced Calcification in Animal Aortas." *Journal of Atherosclerosis Research* 5 (2): 159–173.